UC Berkeley
UC Berkeley Electronic Theses and Dissertations

Title
Selected Topics in Dispersed Multiphase Flow Transport

Permalink
https://escholarship.org/uc/item/9tg192mh

Author
Thacher, Eric

Publication Date
2022

Peer reviewed|Thesis/dissertation

Selected Topics in Dispersed Multiphase Flow Transport

by

Eric William Thacher

A dissertation submitted in partial satisfaction of the

requirements for the degree of

Doctor of Philosophy

in

Engineering- Mechanical Engineering

in the

Graduate Division

of the

University of California, Berkeley

Committee in charge:

Assistant Professor Simo A. Mäkiharju , Chair
Professor Reza Alam
Professor Evan Variano

Fall 2022

Selected Topics in Dispersed Multiphase Flow Transport

Abstract

Selected Topics in Dispersed Multiphase Flow Transport

by

Eric William Thacher

Doctor of Philosophy in Engineering- Mechanical Engineering

University of California, Berkeley

Assistant Professor Simo A. Mäkiharju , Chair

The COVID-19 pandemic heightened the interest in particle-laden turbulent jets generated by breathing, talking, coughing, and sneezing, and how these can contribute to disease transmission. Predicting the transport distance of the expelled droplets remains a critical, and still open, question. In the first segment of my work, I study the effect of ejection geometry and environmental boundary conditions on the transport of water density-matched particles. The study of particle transport from a canonical jet geometry illustrates the influence of secondary flows from the environmental boundary conditions (e.g. thermal gradients and wall effects) on particle dispersal. Subsequent experiments on the particle transport from a repeatable cough generator reveal that vortex structures created by the mouth and tongue structure have a large role in dispersal, due to the ejection of particles from regions of high vorticity.

In the second segment of my work, I study bubbly flows, in which the dispersed and carrier fluid phases are reversed. This flipped density ratio causes bubbles to accumulate in regions of high vorticity. Bubble transport is studied in the context of flow over a cylinder, for which the induced vibration is an important design consideration in devices from flow meters to nuclear reactors. While past researchers have shown that introducing bubbles to the flow can decrease vibration amplitude while increasing shedding frequency, the nonlinear shift in shedding frequency with bubble size has not been explained. Through experimental and numerical study of size-dependent bubble transport, I provide insight into the mechanism causing this change in shedding frequency.

The study of both projects in tandem allows for the exploration of the effect of preferential accumulation/ejection on dispersed multiphase transport. In addition to complementary flow behaviour, the study of interchanged dispersed/carrier phases necessitates the development of highly specialized measurement techniques. I hope that the methods developed in this work see increased use in literature when developing validation datasets, as I look to challenge some of the common assumptions made in existing multiphase transport studies. A common

theme through both projects is that typically second-order effects (e.g. spanwise velocity differences) have a significant influence on dispersed multiphase transport. As dispersed multiphase transport draws increased research interest, I hope that this work illustrates that (until proven otherwise) *the collective understanding of the dominant mechanisms that exist for the single phase flow do not necessarily apply to multiphase transport.*

To my parents, thank you for your encouragement and unwavering support. This would not have been possible without you.

Contents

List of Figures

List of Tables

Acknowledgments

I feel so lucky that I had this opportunity, but I could not have done it alone. So many people have supported me throughout my degree, with everything from exchanging ideas, to sharing experiences, or simply encouraging me along the way.

I owe a debt of gratitude to my advisor, Simo Makiharju. Not only was your expertise incredibly valuable throughout the PhD, your passion for research is infectious. Thank you for your willingness to meet at any hour of the day, and discuss my latest challenges. Most importantly, thank you for all the opportunities you gave me throughout my PhD - to live abroad, work on different and interesting projects, and in doing so figure out the type of research that I want to pursue moving forward.

I feel incredibly fortunate to have had the opportunity to work with many great research collaborators. Thank you to Evan Variano for your support both on my committee and in the lab. Your support was especially invaluable during the pandemic, from encouraging me to take a day off to lending me your bike when the gyms were closed. To Reza Alam, thank you for encouraging me to come to Berkeley, as well as providing feedback as a member of my committee. Thank you to Per-Olof Persson for your patience as I learned to work with Linux, and your flexibility as I had to put our work aside during busy times in the lab. Clark Zha, I really appreciate all the late hours (and frequent re-soldering) on the UAUV project. Thank you to Tvetene Carlson for doing whatever it takes (from painting to drilling holes in the freezer) during the COVID project, as well as our collaborators at LBNL. To all the members of the FLOW Lab, I appreciate the research (and random) conversations that we frequently had in the office. Sharing the research experience with all of you made the PhD way more enjoyable. A special thank you to Andrew Kokubun for all of the discussions and help in the lab on the bubble project. During my time in Brest, I owe so much to Céline Gabillet and Bruno Van Ruymbeke. Thank you for your patience and kindness as I struggled to learn French. Each and every one of you helped me learn so much, and made the research more enjoyable along the way.

Outside of the lab, I cannot thank my friends in Berkeley enough. Whether we were skiing, hiking, or simply chatting I feel so lucky to have such a supportive group of people around me. When I first moved here, I didn't know anyone in the country never mind in Berkeley - I am so fortunate to have met such great people. The PhD would not have been the same without our ski trips and travels around California. For my friends back home, thank you for always making it feel like no time had passed. You have known me from basically the time I first learned what a bubble was, and while there would be months (or years) apart, I always knew that you would welcome me back with open arms (and a free couch).

To my partner Kate, thank you for welcoming me into your family. During the ups and downs of the PhD, you were always by my side. Whenever I am busy, you always work around my schedule to make time to listen, chat, and support me in any way you can. During my last semester, I cannot thank you enough for your support as I struggled to balance work,

writing, and exploring while we were both in France. I appreciate you taking the leap to move abroad and explore together.

Lastly, thank you to my family for all of your support. To my parents, I truly could not have done this without your support. Moving abroad is a challenge, but being kept apart during the pandemic was a challenge that we never expected to face. Your endless support throughout was exactly what I needed to feel like I made the right choice in moving to Berkeley. Your encouragement has ensured that I am excited to continue pursuing research in my career. To Dana, seeing you achieve so much two years ahead of me has always been a continuous source of inspiration. You have set a high standard of success in everything you do - thank you for being a big sister, friend, and role model.

Chapter 1

Introduction

Multiphase flows present a highly challenging, yet interesting, engineering problem. Examples of multiphase flows include droplets in air, bubbly flows, or solid particle suspensions. These flows often exist in turbulent environments, for which the combined study of multiphase flows and turbulence presents a formidable challenge [4]. These challenges arise from deficits in existing measurement techniques (e.g. requirement of optical access), but also interesting phenomena arising from the nature of the flow. These phenomena include preferential accumulation and turbulence modification [4], both of which inhibit a universal understanding of the flow behaviour across a wide range of applications. There is an additional challenge of differing length scales, for which it is highly challenging to resolve boundary layers existing in the carrier fluid as well as on the dispersed phase surface. Consequently, our understanding of the flow must often be made with imperfect knowledge, and (particularly in the case of numerical simulations) with significant assumptions. This is highly prevalent in the study of dispersed phase transport, for which the size of the measurement domain is often determined by the scale of the changes in the carrier phase; having a large domain of interest makes it nearly impossible to resolve the flow on the order of the size of the boundary layer of the dispersed phase.

In short, studying dispersed multiphase transport necessitates significant assumptions, but these must be made highly judiciously - it is difficult to predict *a priori* the effect of simplifications to the effect of transport of the dispersed phase. In such a complex environment, with coupling between the dispersed and carrier phases, we need more studies addressing which simplifications are justified. To this aim, I present work on the study of two distinct applications, completed during the course of my PhD:

1. Studying the transport and deposition of water density matched particles expelled into air.

2. Studying the capture and transport of dispersed air bubbles within cross flow over a cylinder.

Both projects study the transport of a dispersed medium within a multiphase flow. The

primary distinction between these two flows is the density ratio between the dispersed phase and carrier phase, which is reversed from one project to the other. Consequently, different measurement techniques are needed and different phenomena are observed. For this reason, I will spend significant time discussing the measurement techniques used to obtain each result. Prior to delving into the projects in detail, it is necessary to provide a background to the governing equations for transport of a dispersed multiphase flow.

1.1 Governing Equations

The transport of a dispersed, one way coupled spherical particle has been studied extensively. For the definitions of dispersed and one-way coupled flow used in this work, refer to section 1.3. I will largely study the motion of the dispersed phase under the assumption that the particle is spherical, with an unchanging interface.

A major contribution to the field was the analytical derivation of the motion of a spherical particle in a nonuniform creeping flow, for which the governing equation is known as the Maxey-Riley equation [5]:

$$m_p \frac{dV_i}{dt} = (m_p - m_F)g_i + m_F \frac{Du_i}{Dt}\bigg|_{Y(t)} - \frac{1}{2}m_F \frac{d}{dt}(V_i(t) - u_i(Y(t), t) -$$

$$\frac{1}{10}a^2 \nabla^2 u_i|_{Y(t)}) - 6\pi a\mu(V_i(t) - u_i(Y(t), t) - \frac{1}{6}a^2 \nabla^2 u_i|_{Y(t)})$$

$$- 6\pi a^2 \mu \int_0^t \frac{\frac{d}{d\tau}\left[V_i(t) - u_i(Y(t), t) + \frac{1}{6}a^2 \nabla^2 u_i|_{Y(t)}\right]}{\sqrt{\pi\nu(t-\tau)}}d\tau \qquad (1.1)$$

This equation was derived under a series of stringent assumptions:

1. Flow is incompressible, or

$$\nabla \cdot u = 0 \qquad (1.2)$$

2. Sphere is small relative to length scales present in the flow.

3. Stokes flow applies (low Reynolds number limit).

4. Small velocity gradients.

5. Assumed quadratic form for the velocity on the sphere surface.

However, in many applications the assumption of Stokes flow is violated. Therefore, extensions to the Maxey-Riley equations exist. To extend the Maxey-Riley equations to finite Reynolds number flows, the typical approach is to take the critical terms within the Maxey-Riley equation (drag, pressure contribution, added mass, history term) and then apply Reynolds number based corrections to these terms. Furthermore, additional terms are added in an ad hoc manner via superposition, including lift (which by definition is not

included in equations derived under the creeping flow assumption). These adjustments are justified by comparison to experiments, but it is worth noting that with enough correction factors it is not surprising that the equations match with experiments, even if the physical foundation upon which the equation is derived is no longer present [6].

While for brevity I will not go into all of these corrections it is instructive to briefly address the accuracy of empirical relationships for the drag coefficient. Many such empirical relationships exist, including the following from Clift and Gauvin [7] which is valid in the subcritical Reynolds number range ($Re_\tau < 2$ x 10^5) [8]:

$$C_D = \frac{24}{Re_\tau} \left[1 + 0.15 Re_\tau^{0.687} + 0.0175(1 + (4.25x10^4) Re_\tau^{-1.16})^{-1} \right] \tag{1.3}$$

Where $Re_\tau = \frac{D|u-v|}{\nu}$, which is the Reynolds number defined using the relative speed of the sphere, v and the undisturbed fluid, u. The diameter of the sphere is given by D while the kinematic viscosity is given by ν. While the above equation for C_D is widely implemented, this empirical relationship smooths over the effect of secondary parameters on the drag coefficient. In particular, turbulence intensity has a significant effect on drag, which is discussed in more detail in work by Crowe et al [8] and Moradian et al [9]. With increasing turbulence intensity, the drag coefficient decreases [9]. While sufficiently accurate for most engineering problems, the tendency to smooth over secondary effects is cause to treat existing relations for the motion of a sphere in time-varying fluid with scepticism.

With this in mind, if we assume that only body force acting is gravity, then the governing equation for one-way coupled motion of a sphere in a time-varying fluid at finite Reynolds number is given by the following [8]:

$$m_p \frac{dV_i}{dt} = -(m_p - m_f)g + V_p \left[-\frac{\partial p}{\partial x_i} + \frac{\partial \tau_{ik}}{\partial x_k} \right] + \frac{1}{2} \rho_f C_D \pi a^2 |u_i - V_i|(u_i - V_i)$$

$$+ C_M \frac{\rho V_p}{2} \left[\frac{D u_i}{Dt} - \frac{dV_i}{dt} \right]$$

$$+ C_B \frac{3}{2} D^2 \sqrt{\pi \rho_f \mu_f} \left[\int_0^t \frac{\frac{d}{dt'}(u_i - V_i)}{\sqrt{t - t'}} dt' + \frac{(u_i - V_i)_0}{\sqrt{t}} \right]$$

$$+ C_S 1.61 D^2 (\mu_f \rho_f)^{0.5} |\omega_{f,i}|^{-0.5} \left[\epsilon_{ijk}(u_j - V_j)\omega_{f,k} \right]$$

$$+ C_{LR} \frac{\pi}{8} D^3 \rho_f \left[\epsilon_{ijk}\omega_{p,j}(V_k - u_k) \right] \tag{1.4}$$

This is the form of the force balance which will be implemented throughout the remainder of the work. The terms of this equation are as follows:

1. Force due to gravity:

$$F_g = -(m_p - m_f)g \tag{1.5}$$

2. Force due to undisturbed fluid:

$$F_u = V_p \left[-\frac{\partial p}{\partial x_i} + \frac{\partial \tau_{ik}}{\partial x_k} \right] \tag{1.6}$$

3. Force due to steady state drag:

$$F_{drag} = \frac{1}{2}\rho_f C_D \pi a^2 |u_i - v_i|(u_i - v_i) \tag{1.7}$$

4. Force due to added mass:

$$F_a = C_M \frac{\rho \mathcal{V}_p}{2}\left[\frac{Du_i}{Dt} - \frac{dv_i}{dt}\right] \tag{1.8}$$

5. Basset history force:

$$F_B = C_B \frac{3}{2} D^2 \sqrt{\pi \rho_f \mu_f}\left[\int_0^t \frac{\frac{d}{dt'}(u_i - v_i)}{\sqrt{t - t'}}dt' + \frac{(u_i - v_i)_0}{\sqrt{t}}\right] \tag{1.9}$$

6. Saffman lift:

$$F_S = C_S 1.61 D^2 (\mu_f \rho_f)^{0.5}|\omega_{f,i}|^{-0.5}\left[\epsilon_{ijk}(u_j - v_j)\omega_{f,k}\right] \tag{1.10}$$

7. Magnus lift:

$$F_M = C_{LR}\frac{\pi}{8}D^3 \rho_f \left[\epsilon_{ijk}\omega_{p,j}(v_k - u_k)\right] \tag{1.11}$$

As highlighted above, it is important to note the number of Reynolds number based correction factors included in the equation. As illustrated by the above discussion of the drag coefficient, even when widely accepted the equations for these coefficients can still ignore the effect of secondary (yet still significant) parameters. Secondly, to solve this equation accurately we need to integrate since the beginning of time. Lastly, to solve Eq. 1.4 we need to know the flow field of the continuous phase *exactly*. This is nearly impossible in practice.

For these reasons, it is very challenging to use this equation to predict the motion of a spherical particle in a carrier fluid (even if the dispersed fluid is one-way coupled). When deciding which terms to include and/or neglect and which correction factors to use, comparison to high quality validation data is required. Additional terms may also be included, for which a brief description is given in section 1.1.

Additional Effects on Particle Transport

In addition to the terms described in Eq. 1.4, other terms can become important. These include terms related to orientable particles or particle pair interactions, for which a brief description is given in [10]. These terms are neglected in the present work as the flow is assumed to be one-way coupled and with spherical particles.

Bubble motion is particularly challenging to predict due to the nature of a deformable interface. The forces present on a rising bubble are discussed in detail by Kulkarni and Joshi [11]. In particular, it is noted that the rise velocity is dependent on the surface tension of the carrier fluid. This effect is due to the preferential accumulation of surfactant on the

rear surface of the bubble, as surfactants present in the fluid are advected along the bubble surface; this concentration gradient produces a Marangoni effect which introduces finite shear at the interface. This effect does not directly appear in Eq. 1.4, but must be accounted for in carrier fluids with surfactant present. In the present work, bubble motion is assumed to be in clean fluid such that this term can be neglected. In addition to finite shear at the interface, bubbles may deform to shapes which can significantly alter their dynamics. In the present work, we aim to operate in the low-Weber number limit to ensure that bubbles remain spherical [12]. Weber number is defined as $\mathrm{We} = \frac{2DU^2}{\sigma}$, where σ is the surface tension of the carrier fluid. Bubble break-up and accumulation are also neglected, the latter of which is driven under the one-way coupled assumption described in section 1.3.

Even if the particle remains spherical, the particle may change size during its motion; this will introduce coupled dynamics to Eq. 1.4 for the changing particle diameter. In the case of bubbly flow this effect can be significant; for example, the significant alteration of the bubble size as it approaches a low-pressure vortex core is seen in work by Oweis et al [13]. In the present work, this effect is neglected as we are far from a cavitating regime, and do not aim to predict the motion of bubbles *within* the vortex core.

In the case of liquid droplets, the effect of evaporation and relative humidity on the droplet size is indirectly addressed in 2.3. Since the motion of the droplets is not computed in the present work, I will not go into further detail other than to state that these effects are important to consider.

In addition to the above forces, one can also include additional body forces such as electrophoresis, for which the force is given by:

$$F_{elec} = q\mathbf{E}(\mathbf{Y}) \tag{1.12}$$

where q is the charge of the particle, $\mathbf{Y}$ is the particle location, and $\mathbf{E}$ the electric field experienced by the particle. This force is of significant importance in section 2.4

Environmental factors may also play a role, through the indirect alteration of the flow field in the vicinity of the dispersed medium. For example, we know that droplet– or particle– laden jet motion is affected by ambient temperature gradients (e.g. [14]), radiative forcing (e.g. [15]), contaminants, pressure waves, and of course forced and natural convection. The 'near–field' motion is dominated by the jet orifice, mass flowrate, and momentum flowrate. The 'far–field' motion is more strongly influenced by instabilities and turbulence in the jet, as well as the ambient features listed above. These effects can be said to be included in Eq. 1.4 provided that the true flow field is used, but care must be taken to neglect these effects otherwise (e.g. if a canonical jet or similar velocity profile is assumed). Challenges regarding the elimination of background convective and thermally driven flows are described in section 2.2.

Despite the breadth of additional forces which can alter the dynamics, there are some key results which can be derived from simplifying the governing equation given in Eq. 1.4. The most important of these results for this work is the effect of density ratio on preferential accumulation within vortical flows.

1.2 Preferential Accumulation of Particles in Vortical Flows

This derivation closely follows the work of Maxey [16] and Davila & Hunt [17]. To simplify this analysis, we will assume that the Reynolds number of the particle defined using the terminal velocity, $Re_T = \frac{V_T D}{\nu} < 1$, where the terminal velocity is given by V_T. In the low Reynolds number limit, we can assume linearized drag, where the drag coefficient, k_T accounts for finite Reynolds number effects through the following relationship: $k_T = 1 + 0.15 Re_T^{2/3}$ [17]. In this flow regime, we can also eliminate both lift terms from Eq. 1.4. Furthermore, if we assume that there are small particle accelerations (allowing us to neglect the Basset history force), we have:

$$m_p \frac{dV_i}{dt} = -(m_p - m_f)g + V_p \left[-\frac{\partial p}{\partial x_i} + \frac{\partial \tau_{ik}}{\partial x_k} \right]$$

$$+ 6\pi k_T a \rho_f \nu_f (u_i(Y(t), t) - V_i) + C_M \frac{\rho_f V_p}{2} \left[\left. \frac{Du_i}{Dt} \right|_{Y(t)} - \frac{dV_i}{dt} \right]$$

Where $\left. \right|_{Y(t)}$ denotes that the quantity is being evaluated at the particle centre. In conjunction with the assumption of an incompressible fluid, this allows the equation to be simplified to the following:

$$(m_p + C_M m_f)) \frac{dV_i}{dt} = -(m_p - m_f)g + (m_f + C_M m_f) \left. \frac{Du_i}{Dt} \right|_{Y(t)}$$

$$+ 6\pi k_T a \rho_f \nu_f (u_i(Y(t), t) - V_i)$$

Where the $\frac{1}{2}$ factor has been incorporated into the added mass coefficient for simplicity. If we divide both sides of the equation by the factor $\frac{4\pi a^3}{3}(\rho_p + C_M \rho_f)$ then we have

$$\frac{dV_i}{dt} = -\frac{\rho_p - \rho_f}{\rho_p + C_M \rho_f} g + \frac{\rho_f + C_M \rho_f}{\rho_p + C_M \rho_f} \left. \frac{Du_i}{Dt} \right|_{Y(t)}$$

$$+ \frac{\rho_f}{\rho_p + C_M \rho_f} \frac{9}{2a^2} k_T \nu_f (u_i(Y(t), t) - V_i)$$

If we define $\beta = \frac{\rho_p}{\rho_f}$ then we can simplify this expression further:

$$\frac{dV_i}{dt} = -\frac{\beta - 1}{\beta + C_M} g + \frac{1 + C_M}{\beta + C_M} \left. \frac{Du_i}{Dt} \right|_{Y(t)}$$

$$+ \frac{1}{\beta + C_M} \frac{9}{2a^2} k_T \nu_f (u_i(Y(t), t) - V_i) \tag{1.13}$$

To simplify this expression further we will define the terminal velocity, V_T, using the following:

$$6\pi k_T a \rho_f \nu V_T = \frac{4}{3}\pi a^3 (\rho_p - \rho_f)g \tag{1.14}$$

For which we can determine the terminal velocity to be:

$$V_T = \frac{2}{9}\frac{a^2}{k_T \nu}\frac{(\rho_p - \rho_f)}{\rho_f}g = \frac{2}{9}\frac{a^2}{k_T \nu}(\beta - 1)g \tag{1.15}$$

The particle response time, t_P directly follows:

$$t_P = \frac{V_T}{g} = \frac{2}{9}\frac{a^2}{k_T \nu}(\beta - 1) \tag{1.16}$$

The terminal velocity can be substituted into Eq. 1.13 to produce the following expression:

$$\frac{dV_i}{dt} = -\frac{\beta - 1}{\beta + C_M}g + \frac{1 + C_M}{\beta + C_M}\frac{Du_i}{Dt}\bigg|_{Y(t)} + \frac{\beta - 1}{\beta + C_M}\frac{1}{t_P}(u_i(Y(t),t) - V_i) \tag{1.17}$$

As a final reduction we have the following:

$$\frac{dV_i}{dt} = \frac{\beta - 1}{\beta + C_M}\left(\frac{(u_i(Y(t),t) - V_i)}{t_P} - g\right) + \frac{1 + C_M}{\beta + C_M}\frac{Du_i}{Dt}\bigg|_{Y(t)} \tag{1.18}$$

To non-dimensionalize this expression we follow the work of Davila and Hunt [17]. Initially, we define the characteristic velocity $\tilde{U}$ and characteristic circulation strength, Γ. These quantities are related by $t_r = \frac{\Gamma}{\tilde{U}^2}$, where t_r is a characteristic residence time of the particle. We then use this characteristic velocity to produce the following non-dimensional quantities:

$$V_i^* = \frac{V_i}{\tilde{U}} \tag{1.19}$$

$$u_i^* = \frac{u_i}{\tilde{U}} \tag{1.20}$$

$$t^* = \frac{t\tilde{U}^2}{\Gamma} \tag{1.21}$$

$$St = \frac{\tilde{U}^2 t_P}{\Gamma} \tag{1.22}$$

$$V_T^* = \frac{t_P g}{\tilde{U}} \tag{1.23}$$

Substituting these expressions into Eq. 1.18 we have:

$$\frac{\tilde{U}^3}{\Gamma}\frac{dV_i^*}{dt^*} = \frac{\beta - 1}{\beta + C_M}\left((u_i^* - V_i^*)\frac{\tilde{U}}{t_P} - g\right) + \frac{1 + C_M}{\beta + C_M}\frac{Du_i^*}{Dt^*}\frac{\tilde{U}^3}{\Gamma} \tag{1.24}$$

$$\frac{dV_i^*}{dt^*} = \frac{\beta - 1}{\beta + C_M}\frac{\Gamma}{\tilde{U}^3}\left((u_i^* - V_i^*)\frac{\tilde{U}}{t_P} - g\right) + \frac{1 + C_M}{\beta + C_M}\frac{Du_i^*}{Dt^*} \tag{1.25}$$

$$\frac{dV_i^*}{dt^*} = \frac{\beta - 1}{\beta + C_M}\frac{1}{St}(u_i^* - V_i^* + V_T^*) + \frac{1 + C_M}{\beta + C_M}\frac{Du_i^*}{Dt^*} \tag{1.26}$$

If we take the limit of a dense particle (e.g. water density matched sphere in air), then we have $\beta >> 1$, which leads to the following simplified expression:

$$\frac{dV_i^*}{dt^*} = \frac{\beta - 1}{\beta + C_M} \frac{1}{St} (u_i^* - V_i^* + V_T^*) \tag{1.27}$$

For simplicity I will now drop the $*$ notation and will proceed solely with the non-dimensionalized expression. If we state that $A = \frac{\beta - 1}{St(\beta + C_M)}$ then we have the following form:

$$\frac{1}{A} \frac{dV_i}{dt} = (u_i - V_i + V_T) \tag{1.28}$$

In this form, a solution directly follows from Maxey [16], who propose a solution that is accurate to $O(\frac{1}{A^2})$ via a nonlinear integral equation for $Y(t)$, where $V_i = \frac{dY}{dt}$. Under the condition that $V_i(t = 0) = V_T + u_i(Y(t = 0), t = 0)$ we can restate equation Eq. 1.28 as the following:

$$V_i = V_T + u_i|_{Y(t)} - \frac{St(\beta + C_M)}{\beta - 1} \frac{du_i}{dt}\bigg|_{Y(t)} \tag{1.29}$$

Since u_i is evaluated at the centre of the particle, $Y(t)$, the expression $\frac{du_i}{dt}$ is implicit in $Y(t)$. Consequently, the derivative $\frac{du_i}{dt}$ is given by the following [16]:

$$\frac{du_i}{dt} = \left[\frac{\partial u_i}{\partial t} + V_i \cdot \nabla u_i\right]\bigg|_{Y(t)} = \left[\frac{\partial u_i}{\partial t} + (V_T + u_i(Y(t), t)) \cdot \nabla u_i\right]\bigg|_{Y(t)} + O(\frac{St(\beta + C_M)}{\beta - 1}) \tag{1.30}$$

Combining Eq. 1.29 and Eq. 1.30 we have the following:

$$V_i = V_T + u_i - \frac{St(\beta + C_M)}{\beta - 1} \left[\frac{\partial u_i}{\partial t} + (V_T + u_i(Y(t), t)) \cdot \nabla u_i\right]\bigg|_{Y(t)} \tag{1.31}$$

If we take the divergence of both sides of the equation then we obtain the following expression [17][16]:

$$\nabla \cdot V_i = -\frac{1}{4} \frac{St(\beta + C_M)}{\beta - 1} \left[\left(\frac{\partial u_i}{\partial x_j} + \frac{\partial u_j}{\partial x_i}\right)^2 - \left(\frac{\partial u_i}{\partial x_j} - \frac{\partial u_j}{\partial x_i}\right)^2\right] \tag{1.32}$$

For which it is apparent that the divergence is negative when the strain rate exceeds the vorticity, and positive otherwise. Consequently, dense particles ($\beta >> 1$) gather in regions of high strain rate and low vorticity. It has been shown that the opposite is true for light particles ($\beta << 1$), which will gather in regions of high vorticity and low strain rate [18].

This distinction based on the density ratio separates particles in vortical flows into two fundamental regimes:

1. Particles that are heavier than the carrier fluid, which get flung from regions of high vorticity.

2. Particles which are lighter than the carrier fluid, which collect in regions of high vorticity.

These two distinct regimes establish the foundation for the remainder of my dissertation. The two selected research topics explore both sides of this phenomena, and allow me to explore the fundamentally different transport phenomena that results. Before going through these projects in detail, I will provide some critical definitions which are useful throughout the remainder of the document.

1.3   Critical Definitions

Dispersed Flow   For the purpose of this work, I will use the definition of Balanchar and Eaton [4] to distinguish *dispersed* multiphase flows from free-surface and other multiphase flows. In the case of dispersed multiphase flows, the effect of the interface (including agglomeration and contact forces) is secondary.

One-way Coupled Flow.   The presence of particles or droplets in a flow can radically change the flow dynamics, notably the turbulence. One classification scheme names this effect "two–way coupling," in contrast to the "one–way coupling" regime in which the fluid flow is not significantly modified by the presence of suspended material. The particle–laden jet can be in either regime depending on the concentration and properties of particles or droplets. Elghobashi [19] (with recently proposed updates [20]) offers an approximate criteria for when the flow could be considered one-way coupled due to turbulence considerations. The criteria proposed by Elghobashi is that the flow is one-way coupled if the volume fraction is below 10^{-6}, and the flow is considered four-way coupled (particle-particle interactions are also important) if the volume fraction is above 10^{-3}. In the present work, the average particle volume fraction in particle ejection experiments is well below 1×10^{-6}.

In the case of bubbles, the two-way coupling limit is more challenging to define. As stated by Mathai et al [21], it is sufficient for one bubble to significantly modify the fluid (e.g. single bubble interacting with a vortex ring [22]), so the particle limits are not appropriate. Instead, we qualitatively define one-way coupled bubbly flow as cases in which the primary flow features are not modified by the presence of the bubbles. Generally, this should be the case if the bubbles are smaller than the dominant vortex length scales present in the flow, there is little to no bubble coalesence, and there are no observed changes in bulk fluid properties (such as the shedding frequency).

Particles vs. Droplets   Droplets and particles can be considered as different categories based on their composition or their surface slip behavior. While some works refer to both generically as 'particles,' in this work a clear distinction is made. We use the term 'particle' to describe those objects that begin their journey from the jet as a solid. We use the term 'droplet' to describe objects that are initially fluid, although it is important to note that

the liquid can evaporate and effectively transform the droplet into solid particles composed of non–evaporative material. For this work, the density of droplet/particles is always larger than the carrier fluid.

Aerosol and Ballistic Particles   Droplets and particles can also be categorized based on their dynamics, e.g. by their Stokes number or the continuum from 'aerosol' to 'ballistic' behavior. An aerosol quickly loses its initial momentum, settles slowly through the local flow over minutes (or hours), and is generally a faithful flow tracer. A ballistic particle or droplet maintains its initial momentum long enough to significantly cross streamlines, and thus mostly follows its own trajectory. We can use projectile motion equations to estimate time for a ballistic particle to reach ground $t_{fall} \approx \sqrt{(2h/g)}$, where h is the initial height and g the acceleration due to gravity. Thus a ballistic particle starting at a human nose 165 cm high will settle to the floor in ≈ 0.6 sec. Herein we consider particles that are in between the extremes of ballistic and aerosol dynamics. These 'mid–range' droplets and particles have diameters 1–100 μm. Their trajectory is a strong function of both their initial momentum and the local flow field. In the 'mid–range,' there is not a completely closed equation for momentum conservation on a particle or droplet approximated as a single point mass. Note that using a trajectory based distinction (the changing role of initial momentum vs. the local flow field in the dynamics) differs from previous definitions which are based on evaporation time (e.g. Wells [23]).

1.4   Organization of Dissertation

The thesis is organized as follows. In section 2 I present methods for studying droplet and particle transport in air. In section 3 I present the application of these methods to the transport of particles from two different release geometries in a quiescent environment. It is seen that particle transport is highly dependent on the initial vortex structures produced from the release geometry. In section 4 I present methods for studying bubble transport in the context of flow over a cylinder. In section 5 I apply these methods to identify bubble positions and tracks in the dilute bubbly flow regime. The vortex distortion in the vicinity of the cylinder appears to be highly coupled to the size-dependent mean bubble trajectory, for which tracks are non-trivial to estimate *a priori*. In section 6 I present the conclusions of my work as well as directions for future research.

Chapter 2

Droplet and Particle Transport in Air

Particle–laden jets have been studied in many contexts, from internal combustion to environmental processes (e.g. [24]). The primary application for my work is that of disease transport, for which the COVID-19 pandemic was the impetus for starting the project. A major vector of SARS-CoV-2 virus transport is thought to be respiratory droplets that are expelled when coughing, speaking, and breathing (e.g. [25]). To reduce person-to-person exposures, businesses, schools, and other building owners implemented numerous safety measures to minimize the risk of exposure to the virus. One such measure was the implementation of social distancing, for which there are still significant uncertainties in choosing an appropriate distance. Tests on the efficacy of these measures were often empirical and ranged widely in their thoroughness, which further excacerbated the challenge of developing appropriate safety measures.

These shortcomings served to highlight the importance of understanding respiratory aerosol transport from first principles. Two factors which have a significant impact on droplet travel distance are environmental factors and the aerosol release conditions. To better understand the influence of these factors, section 2.1 provides a review of literature on aerosol transport in different environments. Section 2.1 reviews the effect of the release geometry on aerosol transport.

Following these reviews, I will detail the experimental methods I developed to study aerosol transport, followed by some key results in chapter 3. The methods presented in this chapter closely follow the paper by Thacher et al [1].

2.1 Literature Review on Aerosol Transport in Different Environments

The review presented here closely follow the review given in Thacher et al [1]. Numerous measurements have addressed the question of droplet and aerosol transport in practical environments. Many reviews exist, which cover a range of qualitative and quantitative data (e.g. [26, 27, 25, 28]). Of particular interest is the transport of respiratory aerosols in

medical facilities, for which many types of aerosols have been studied. These include benign bacteriophages (Sze To et al [29]), liquid droplets [30, 31, 32], or the SARS–COV2 virus itself (e.g. Nissen et al [33]). Additional papers on practical environments include the movement of aerosols in an airline cabin (Zhang et al [34]), laboratory (Liu et al [35]), furnished office–type space (Richmond-Bryant et al [36]) or multi–zone indoor spaces (Miller and Nazaroff [37]).

Measurements in practical environments cannot provide all of the boundary conditions needed to validate numerical models. Thus some measurements have used controlled environmental chambers to study aerosol motion. These can include the influence of common sources of convection such as thermal plumes, ventilation, or air conditioning [38, 39, 40, 41, 42, 43, 44, 45, 46]. These can also focus on the fundamental case of respiratory jets with nominally no background flow [47, 48, 49, 50, 51]. In an effort to provide validation data in a well-known environment, the work presented in chapter 3 is of the latter type, focusing on jets with no background flow.

Though there is still much more to learn, many researchers have pursued measurements in nominally quiescent environments in recent years. Droplet production and transport from a sneeze was investigated by Bourouiba et al [50, 49]. Comparing sneeze flows to measured fallout and deposition from a particle–laden multi–phase puff in a water tank, they created a theoretical model to predict droplet transport distance. Also using a water tank, Wei and Li [47] show the importance of how the temporal variation in flowrate impacts the transport patterns in a simulated cough. The approach of using water tanks and applying similitude to translate the results to air is a practical way to simplify some of the challenges of working with real aerosols (discussed below). Still, there are limits to what can be achieved with similitude, given that particles are typically $O(1)$–$O(10)$ times denser than water while particles and droplets are typically $O(1000)$ times denser than air. Therefore there is a need to directly measure aerosol transport in air.

A major challenge in directly measuring respiratory aerosols is managing their broad size distribution. Optical measurements must correct for the nonlinear effects of scattering, which becomes challenging when the optical path between emitter and receiver is complex. For example, laser–sheet imaging (shown from our laboratory in Fig. 2.1) produces results that are biased towards large particles in a manner that is very difficult to correct. This bias is important for the work of Zhu et al [48], who used particle image velocimetry (PIV) to measure cough–ejected particles using three healthy male subjects.

Bourouiba et al [49] note the size–selectivity of optical methods in their quote, *"more droplets and mist were observed with naked eye than the camera"*. In our experiments (discussed below) there were also biases in the optical methods found within some optical particle counters (OPCs). These biases may affect the work of Zhu et al [52] which measures the dispersal of nanoparticle aggregates using multiple optical particle counters within a room. Some measurement methods that manage the difficulties of particle or droplet size distribution are discussed later in this manuscript.

Quantified background flows contribute greatly to the value of idealized experiments. Discussion of these flows varies from qualitative to quantitative. On the qualitative side, Jones
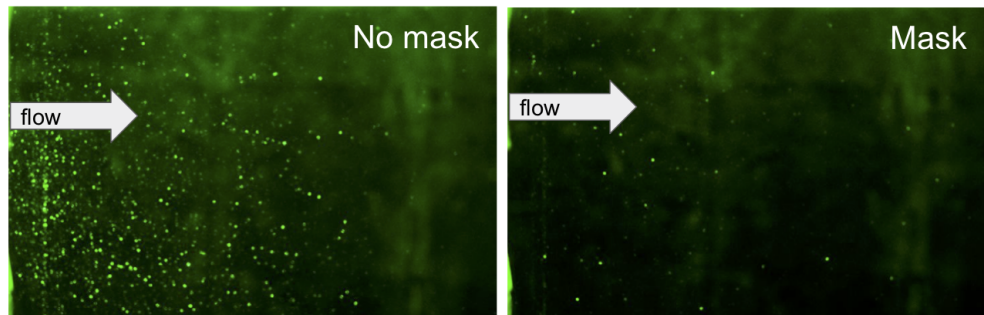
Figure 2.1: Light–sheet imaging of respiratory jets from a speaking person with and without a surgical mask (field of view 50 cm wide). The axis and direction of the jet are indicated by the arrow and are opposite to those of the laser light sheet. The imaging misses many of the smaller droplets in a way that is greatly affected by laser quality, image–capture settings, optical components and their alignment [1]

.

and Nicas [14] described the background thermal convection visible when using fluorescein–dyed liquid droplets to measure deposition patterns in a nominally quiescent room. Sajo et al [53] extended this conclusion by discussing how deviations between the measured and modeled deposition of 0.01–15 μm solid particles on adhesive collector foils may have been caused by thermal gradients or electrostatic effects. Lee et al [51] quantify the background flow inside their study space using the metric of air changes per hour (ACH) and report ACH = 0.0037 for their measurement of respiratory aerosols in a cleanroom.

The particle size range considered by previous researchers leaves some gaps to be filled. Respiratory aerosols are known to span the range of $< 1\mu m$ to $> 100\mu m$ [54]. However, Jones and Nicas [55] notes the lack of room–scale validation–quality experiments with particles larger than 1 micron. This is of particular concern because the 1–100 micron range includes a changeover from tracer behavior to motion dominated by particle momentum and gravitational settling [56]. This size range is also especially important when considering liquid droplets: as reported in Wang et al [57] mid–range ($\approx 50\mu m$) droplets are especially sensitive to the rate of evaporation. Furthermore, mid range sized droplets are poorly covered by the popular discrete random walk (DRW) models (Wei and Li [58]).

Having reviewed these previous works, we conclude that more attention is needed in several areas:

1. Decreasing the effect of boundary conditions on particle and droplet deposition measurements.

2. Measuring the transport of particles and droplets from 1–100 μm

3. Sampling particles and droplets in a manner that captures the size distribution accurately.

In addition to these issues, it is also important to assess the effects of release geometry on aerosol transport.

Literature Review on Effects of Release Geometry on Aerosol Transport

This section closely follows the review provided in Thacher and Makiharju [3]. Previous studies of the human cough have noted significant subject-to-subject variation [59, 60], as well as the dependence of the flow rate on body position (Tang et al [59]) and number of sequential coughs [61, 62]. Consequently, most studies consider cough transport in aggregate, for which initial droplet size distributions [63, 64] and velocity of the gas phase in the centerline plane have been investigated. The velocity of the fluid has been studied using Schlieren imaging [65, 59], particle image velocimetry (PIV) [66, 67, 68, 48, 63, 69], shadowgraph (e.g. Tang et al [70]) and hot-wire measurements (e.g. Dudalski et al [66]).

Experiments which attempt to quantify droplet transport using human subjects are limited [48]; instead, droplet or particle transport is typically studied numerically or using "analogue" experiments with simplified geometries. The stated resemblance of the vertical centerline velocity profile to a round jet (e.g. Tang et al [59]) has led a round jet type profile to be frequently assumed in droplet transport studies (e.g. [58, 40, 71, 72]). Even when facial features are included, mannequins with a circular airway are commonly used (e.g. [73, 74, 75]). Similarly, while some numerical studies resolve outer features of human subjects such as the jaw [48, 76], the inlet airflow is still commonly computed using an injection area and flow rate rather than resolving the complexities of the inlet jet. The assumption of a round jet continues to persist despite indications of vortex ring dynamics present in human coughs [65]. In an effort to capture additional complexity of the cough flow structure, Bourouiba et al [49] and Wei and Li [47] suggest that the cough may be best represented by a multiphase puff or an interrupted jet, respectively. While an improvement, Wei and Li [47] noted that the difference in spread angle of the analogue and human subject may be due to the missing complex oral cavity, including the effect of teeth.

While experimental studies occasionally use mannequins with oral features, the accuracy of these models varies significantly. The oral cavity ranges from simplified semi-elliptical mouths (e.g. [77, 78]) to 3D printed computed tomography (CT) scans including the lungs, bronchi, and internal passages (e.g. [79, 80]). Focusing on the centerline plane, Berlanga et al [79] demonstrate the dependence of the flow field on the airway geometry through PIV measurements of a simplified airway (straight circular tube ending in a semi-elliptical orifice) and a CT scanned realistic airway. Among other effects, it was noted that the simplified model has a longer and clearer core structure in the initial vortex when compared to the realistic geometry, which results in a longer distance before the origin of a secondary vortex downstream. While these differences are apparent in the centerline plane, further research work is still needed as out-of-plane studies on the cough flow field either do not quantify velocities [62] or focus on a single horizontal plane [81]. To my knowledge, the 3D velocity

distribution from a cough has not been experimentally studied. Consequently, it is not possible to glean insight on the effect of vorticity present in the cough on particle transport. This is a major limitation, given that it is well known that vorticity can significantly affect particle transport [82].

Far from the exit of a single-phase jet the inlet geometry has a diminished effect. However, there is known dependence of self-similarity scaling on the initial conditions [83, 84]. In other words, the initial conditions are known to influence the development of coherent structures. These structures have a significant impact on particle transport. The effect of vortical flows on particle transport has been studied in a variety of canonical flows including: a vortex-ring [85], Lamb-Oseen vortex [86], Rankine vortex [17], spherical vortex [87], and free-shear flows [88, 86, 89, 90, 91]. For each of these flows, particle transport was highly dependent on the details of the vortical nature of the flow, and dense particles preferentially accumulated or were ejected in specific regions of the flow.

In large part due to the well-established phenomenon of particle clustering described in section 1.1, efforts to produce self-similar particle velocity profiles [92] and particle fluxes [93] for particle-laden turbulent jets have not yielded universal scaling. These approaches depend on scaling with the local Stokes number and local particle spreading rate, respectively. The lack of a universal scaling is driven by the interaction between the particle response time and local structures in the carrier fluid, which is explained in section 1.1. Hence, studies of the flow field produced during a cough should capture both the mean flow field, as well as the initial size and breakdown of the 3D flow structures downstream in order to accurately predict particle transport. Yet, much remains unclear about the characteristic structures in the flow and their influence on droplet transport.

Literature Review Summary

Through review of available literature, we have established the following key issues in literature:

1. Assessing and eliminating (as required) the effect of environmental boundary conditions on particle and droplet deposition measurements.

2. Developing reliable measurement techniques the transport of particles and droplets from 1–100 μm

3. Sampling particles and droplets in a manner that captures the size distribution accurately.

4. Understanding the influence of mouth geometry on particle transport.

We address these four issues herein and present data on particle transport in an environment with carefully controlled boundary conditions. We achieve this using a variety of techniques (high–speed imaging and charge–neutral deposition sampling) and discuss others that we ruled out along the way. The methods laid out in this work address key challenges

in producing steady, uniform, and accurately measured boundary conditions in particle and droplet transport experiments.

To ensure that the experiments were conducted in a simplified, repeatable, environment, the released air in all experiments was at ambient temperature. This was an intentional decision to choose *repeatability* over realism. It is understood that buoyancy effects are significant in particle transport (e.g. Bourouiba et al [49]); however, I believe that repeatable studies which intentionally eliminate certain effects are critical for isolating complex phenomena (such as the effect of boundary conditions on particle transport). Secondly, the majority of our work was on the study of solid particles instead of liquid droplets. The study of droplets is limited to an illustrative test case given in section 2.3. These choices allow us to ignore the effects of buoyancy and evaporation on droplet transport in the results presented in chapter 3.

Section 2.2 discusses the laboratory facility we constructed for controlling boundary conditions. Section 2.3 discusses methods for droplet measurement and Section 2.4 discusses methods for particle measurement.

2.2   Droplet and Particle Transport Facility

The Cal Covid Cube, C^3, was set up to evaluate experimental methods and provide data suitable for validating numerical models. The C^3 is a parallelepiped room that is 232 cm tall, 376 cm long and 284 cm wide on the inside. A diagram of the C^3 is included in Fig. 2.2. The three main features of the C^3 are as follows:

- **Isothermal.** The C^3 has 10.5 – 13 cm of thermal insulation surrounding it on all sides, built using the methods from walk–in freezers. The C^3 is located in the middle of a building at least 5 m away from all building walls, with no direct sunlight exposure. The ceiling is also insulated, with both foam and a 21–cm air gap between the interior and exterior surfaces. The insulated floor rests on a concrete floor. An empty sub–basement is beneath the floor, helping shield the floor from daily variation in temperature. Temperature uniformity was checked with an Extech 42542 infrared (IR) thermometer (nominal uncertainty $\pm 2°C$) and two Hobo MX2302A data loggers (nominal uncertainty $\pm 0.2°C$). Before each measurement, we confirmed that temperatures were isothermal within the uncertainty of these thermometers.

- **Quiescent.** The isothermal conditions discussed above keep the thermal convection in the C^3 to a minimum. Flows driven by external pressure gradients are also non-detectable (and presumed negligible) because there are only two access holes connecting the exterior and interior of the C^3. The first access hole supplies the jet via a pipe of inner diameter 9.78 ± 0.02 mm) tightly fitted through the hole. The second hole (diameter 75 mm) is to release pressure from the C^3 as the jet delivers air. It is located directly across from the jet orifice, but higher up the wall (see Fig. 2.2). That is, the pressure release hole is at a height of 213.5 cm while the jet is at a height of
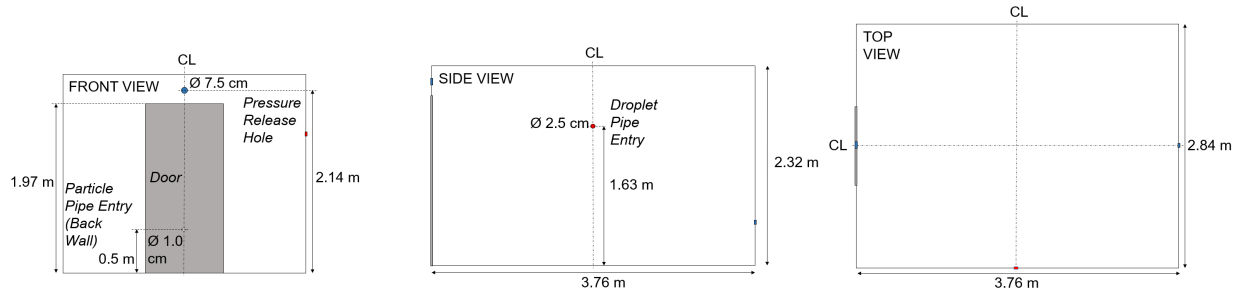
Figure 2.2: Inside dimensions of C^3 including pipe entry and pressure release holes. During particle release the droplet pipe entry hole was closed and vice versa. During all experiments the door was closed. [1]

50.2 $\pm$0.2 cm. Quiescence was verified with both hot wire measurements and with the particle–deposition measurements described at length below. In these, free–falling particles $O(30\mu m)$ showed the same deposition pattern with no observable drift in many repeated observations.

• **Isopotential.** Accumulated charge on the C^3 can significantly change the deposition pattern of particles and drops, as discussed further below. To prevent this, the outer and inner surfaces of the C^3, including all parts of the door, are finished with conductive material (conductive aluminum and stainless steel) and connected to each other with copper tape. The door, interior shell, and exterior shell were tied to building ground. Inspection for electrical path resistance revealed no measurable resistance within the accuracy of the Fluke 87V multi-meter. Electric fields were surveyed with Simco–Ion FMX–003 electrostatic field meter and found to be negligible within precision of instrument ($\pm$0.1 kV).

Other design elements include an all–matte–black interior to support imaging and also a location on the ground floor to limit vibrations. To ensure that the environment remains isothermal, all building air supplies within 3 m of the C^3 are disabled. When these supplies were not blocked, a temperature gradient ($\approx 0.4°C$) developed across the interior of the C^3 and led to a detectable convective flow inside the C^3. This flow led to a detectable drift in particle motion, which can be seen qualitatively in Fig. 2.3. This shift is particularly notable as the thermal gradient was caused by an air vent several metres away from an insulated and enclosed chamber. Many environments are not controlled to this degree, and yet the impact on particle dispersion is visible to the naked eye.

With the environment controlled, repeatability was our second main goal. Even though cough and sneeze flows are unique to the individual (see section 2.1), with variable velocities and droplet densities, repeatable experiments are required for numerical validation.

In addition to ejecting droplets/particles within ambient temperature air (see discussion in section 2.1), we simplify the release by considering different layers of complexity. This allows an explicit evaluation of the effect of the mouth geometry on particle transport. To
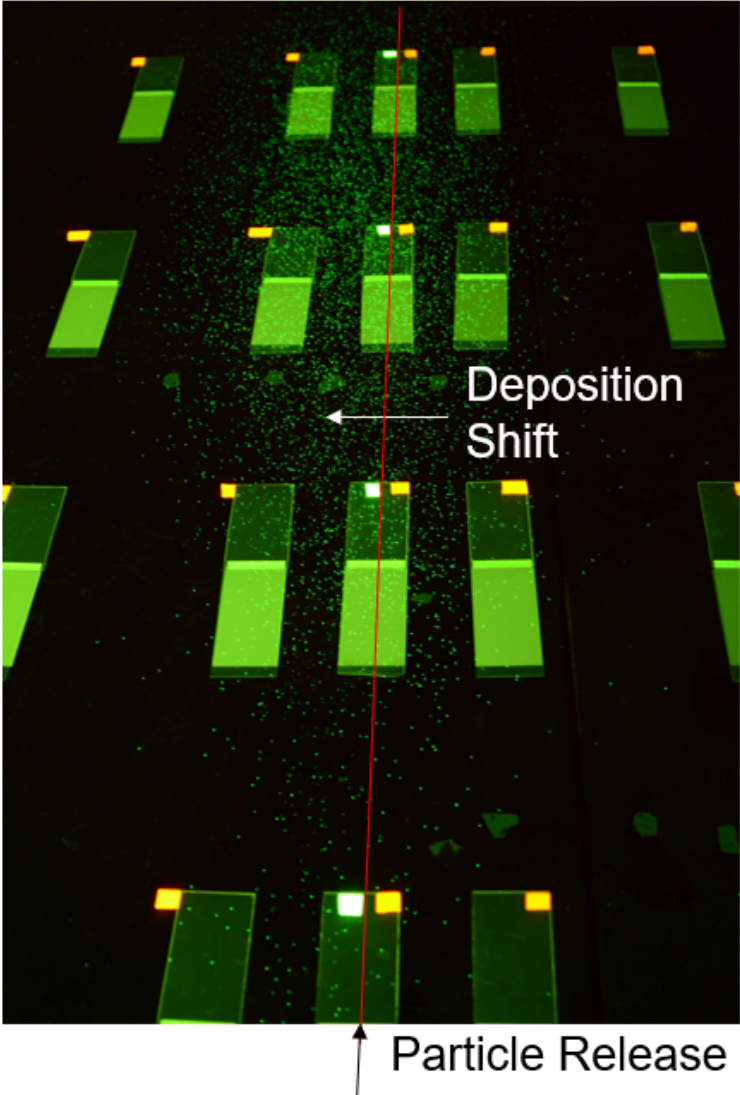
Figure 2.3: Particle drift due to $\approx 0.4°C$ thermal gradient, perpendicular to direction of particle release. The centerline is indicated in red.
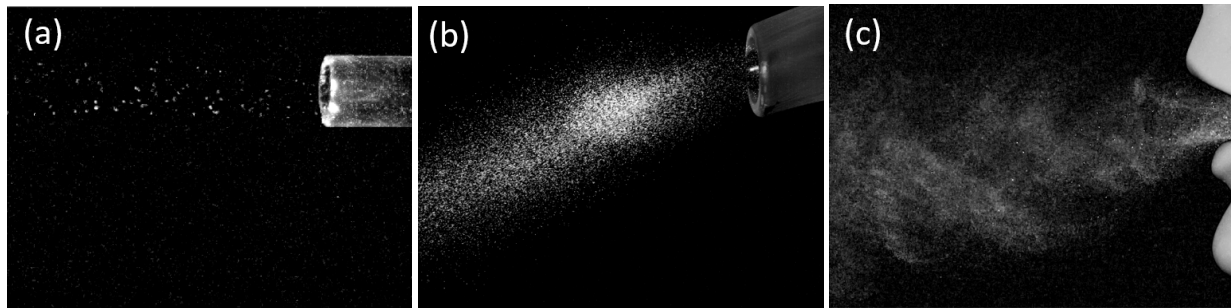
Figure 2.4: Snapshot of particle ejection from (a) straight pipe, (b) smooth 90° curved pipe, (c) intubation trainer doll, with realistic airways and mouth/tongue structure [1].

this aim, we produced three jet orifices which take us from a canonical turbulent jet towards a true cough or sneeze (see Fig. 2.4). The three jet orifices, in order of increasing complexity, are given below:

1. Straight round pipe with sufficient length to reach fully developed flow.

2. Smooth 90° curved pipe, with a changing radius along the length of the pipe.

3. Intubation trainer doll, with realistic airways and mouth/tongue structure.

Using this facility and release geometries, it is now necessary to develop methods for studying the deposition location of released droplets and particles. Section 2.3 provides methods for studying droplets, while section 2.4 details methods for studying particles.

2.3   Droplet Measurements

This section closely follows work produced in Thacher et al [1]. The free exchange of mass across the air-liquid interface introduces significant complexity in the study of droplets. Droplets can grow or shrink as a result, and this occurs at timescales short enough that initial conditions alone are likely insufficient to predict droplet transport. In other words, the boundary conditions are of key importance. This is true for both the air– and liquid– phases. In both phases, the rate of cross–interface exchange is set by temperature, solutes, and flow patterns. A notable example is the presence of salt in water droplets. Saltwater droplets can reach an equilibrium size under the same conditions for which pure water droplets evaporate entirely.

The humidity and temperature of the co-flowing air affect the size of droplets via evaporation or condensation. The temperature of the co-flowing air also can add to the buoyancy difference between the droplet–laden jet and the ambient air into which it flows. Even if the co-flowing air begins at the same temperature and humidity as the ambient air, it can become cooled if droplets are evaporating. To eliminate these complexities, most data presented here

uses solid particles instead of liquid droplets. However, it is important to remember that evaporation and humidity effects are important in many environments. For this reason, some time was taken to develop methods for liquid droplets, with the hope that this work will be continued in the future.

Liquid droplets were generated using an ultrasonic transducer in a constant–depth water bath generating polydisperse droplets. The droplets are made by mechanical means from water with a controlled amount of fluorescent dye (Sigma-Aldrich Fluorescein sodium salt F6377).

The humid droplet–laden flow was fed to a pipe, and at the exit of the pipe a phase Doppler interferometer measures droplet size and velocity. In this study, a straight pipe with 2.38 ± 0.005 cm diameter and 117 ± 1 cm length (L/D = 49) was utilized to simplify the initial condition (i.e. to have a nominally fully developed pipe flow at the exit).

Deposition of droplets on the floor was quantified by collecting drops in plastic weigh boats on a horizontal grid. The C^3 door was not opened until 30 minutes after the experiment to ensure that droplets $> 3.6 \mu m$ had settled. A standard amount of water, in this case 3 mL, is added to each weigh boat to collect the deposited dye. The concentration of dye in this water is measured using a fluorometer (Turner instruments 10AU) with a minimum detection limit of 0.01 ppb. It uses a 510-700 nm emission filter and a narrowband 491 nm excitation filter designed specifically for detecting fluorescein. A calibration was conducted with an average error of 3% for a given measurement over a range of 0.05 ppb to 240 ppb Fluorescein.

To illustrate the application of these methods, we report here the difference between identical droplet–laden jets entering ambient air with 90% vs. 25% relative humidity. As seen in Fig. 2.5, in the low–humidity environment droplets spread much more evenly throughout the room. This is likely due to faster evaporation in a drier environment, leading to smaller droplets. The higher residence time of these droplets allows for more even dispersal by convection from the flow set up in the C^3 by the droplet-laden jet. The effects of humidity on droplet size are explored further by Yang and Marr [94].

The effect of environmental humidity on droplet dispersal is illustrative in emphasizing the importance of carefully defining environmental boundary conditions. However, controlling humidity and temperature on a room scale is challenging. Consequently, the study of particle transport greatly simplifies the problem; this simplification allow for the characterization of alternate effects (such as the mouth geometry) in the absence of conflating factors. The following section provides methods for studying particles.

2.4 Particle Measurements

To study particle transport, our methods focused on quantifying surface deposition. This section closely follows Thacher et al [1]. In–air sampling by optical particle sensors (OPS's) was also tested, but there were significant challenges that led us to focus on deposition instead. Namely, the OPS designed to measure particle of the size that was used $(22-212 \mu m)$
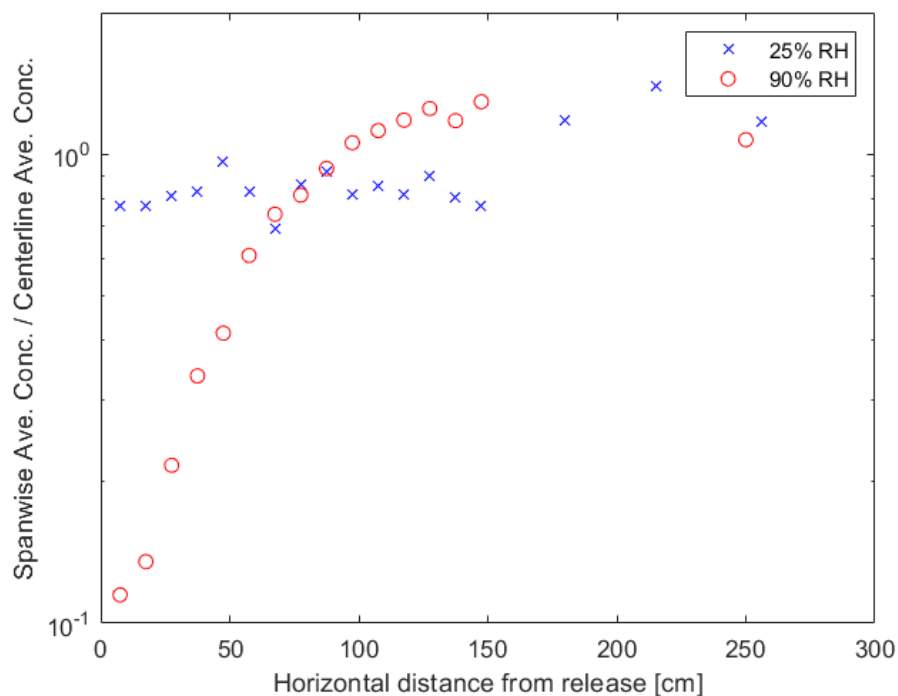
Figure 2.5: Initial experiments of droplet deposition measured by the fluorescein method. Ambient air is at T= 22°C and 90% relative humidity. The source of the jet was located at a height of 163 ± 1 cm, and measurements were made on the floor of the C^3. Plotted concentrations are normalized by the average concentration along the centerline of droplet ejection [1].

could not robustly separate and size the well–characterized particles used in our tests. This is likely due to the high concentrations of background particles (many devices are designed for use in clean–rooms). Upgrading these devices to utilize more of the color spectra would help, as is done in devices which identify particulate matter that comes from combustion. However, it was decided to focus on counting individual particles to reduce the uncertainty in OPS sampling accuracy.

Passive collection (deposition) has been done on glass, foil, silicon "witness wafers," and adhesive "coupons" or "strips." Active collection pulls air through a filter that is later washed to collect the particles; this method can amplify the signal by increasing the "footprint" of the sample. We chose to use passive collection and developed two methods that unite the benefits of foil and adhesive sampling. Adhesive sampling allows users to move and store the samples without risk of disturbing the particles, but care must be taken to ensure the strip does not retain a static charge. Foil sampling allows the surface to be charge–neutralized. The two methods that were developed are: (1) grounded aluminum–backed carbon sampling strips, (2) non–conductive adhesive sampling strips (TriTech vinyl backed print lifters) treated with

an ionizer. For the results that are reported in chapter 3, the Tritech vinyl backed print lifters were used. To characterize spatial deposition patterns, the strips are set out on the ground in a grid below the jet outlet. A surface concentration is calculated for each strip by optical imaging.

Static charge effects can manifest through particle–particle or particle–surface interaction, both of which affect particle deposition patterns. The effect of neutralizing sampling strips with an ionizer is seen in Fig. 2.7. The process of peeling off the cover to expose adhesive charges the sampling strips, and this repels particles as seen in subplot (a). Neutralized strips do not repel particles, as seen in subplot (b). The non–conductive sampling strips were ionized by placing them underneath a Simco–Ion 5225 AeroBar until the static charge (measured with Simco–Ion FMX–003 electrostatic fieldmeter) on the strip was between $[-0.2kV, +0.2kV]$. This was an empirical limit for charge below which there was no noticeable difference in deposition between the sampling strip and the charge–neutralized floor. The conductive adhesive strips (carbon tape with aluminum backing) were grounded to the isopotential C^3 floor and walls.

To image the particles on a sample strip we tried research–grade slide–scanning microscopes, scientific digital cameras with macro–lenses, teaching–grade USB microscopes, and finally found the best balance of speed and quality with a commercial flat–bed scanner. We pushed the detection limit of this method by working at 6400 dot–per–inch scans and post–processing using the Hough transform to identify particles in the target size range. Accuracy of particle counts was improved with layered checks using color intensity and particle shape for the rejection of crushed/broken particles, dust/debris, and other foreign bodies. With these efforts, we were able to measure particles of 20 μm and larger.

To verify accuracy of the particle–counting code, a comparison of $22 - 27$ μm particle counts from the scanned image was made to images taken with Zeiss AxioZoom microscope with 7.0x objective and mCherry bandpass filter, for which results are seen in Fig. 2.6. Over the imaged area of the sample strip (48.0% of total, when accounting for overlap in microscope images), there are 1080 matched red particles, 18 unmatched red particles, and 18 false positives. This amounts to a matching rate of 98.4% and a false positive rate of 1.6%. Violet particles were matched based on position but since the microscope images were monochrome a separate count of missed violet particles was not possible. Notably this error is significantly below the variation in particle count seen from test to test in both sets of experiments (described in detail in section 3). A full listing of the test–to–test variation across locations and particle sizes for release from a straight pipe is provided in Table 3.4. The test–to–test variation during the intubation trainer release is given in Table 3.6. A research team with extensive microscopy resources could likely extend our method to smaller particles. However, this would also require interventions in particle aggregation such as delivering particles from a fluidized bed.

(b) Microscope image of strip with red band-pass filter applied.

(a) Locations of microscope images superimposed on particle scan with identified particles.
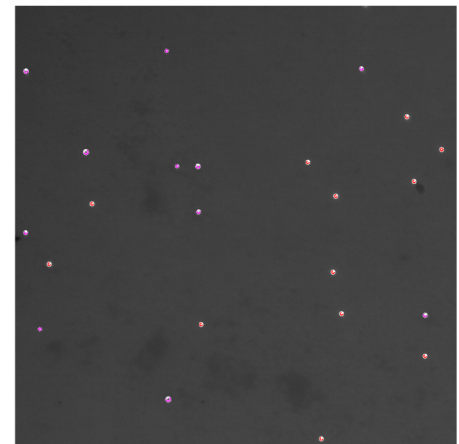
(c) Matched particles.

Figure 2.6: (a) Red highlighted section from scan is compared to (b) red bandpass filtered microscope image. (c) Particle counting comparison where red circle indicates match of 22–27 μm particle and violet circle indicates match of 45–53 μm particle [1].
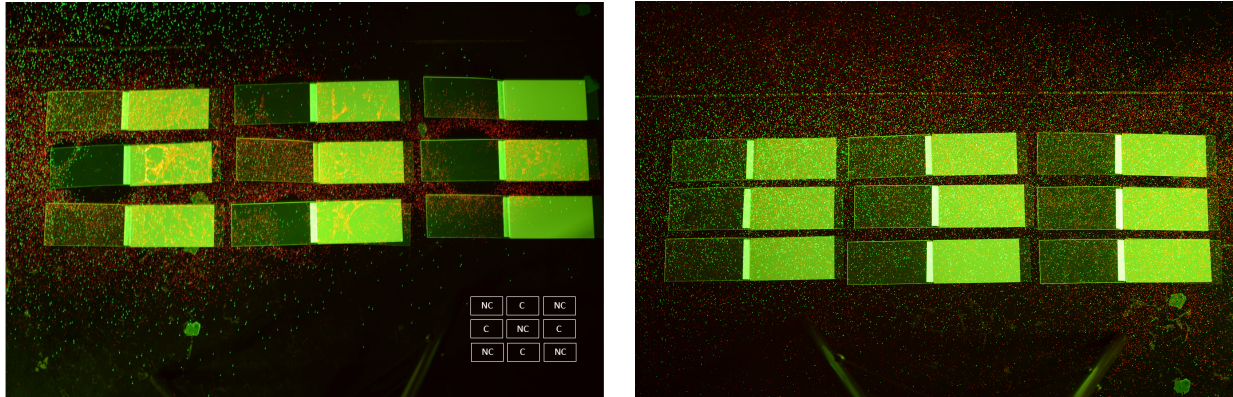
(a) No effort to eliminate particle charging.   (b) Particle tribocharging eliminated.

Figure 2.7: Comparison of particle deposition on alternating charged (C) and neutralized (NC) strips. The same pattern of charged and neutralized strips is used in (b) with particle tribocharging eliminated upstream of the jet [1].

Analyzing Charge Effects

It should be noted that had the particles not been fluorescent and large enough to be imaged with a wide field of view (encompassing the sampling strips), charge effects would not have been readily observable. To determine if electrophoresis can be neglected in the more general case, the force resulting from an external electric field on a charged particle could be compared to the force of gravity or drag force. The forces due to gravity and drag are described in section 1.1. The equation for the electrostratic force is given in Eq. 1.12.

When $F_{electrophoresis} << F_{gravity,drag}$ we assume the former is negligible. However, no common criteria appears to be evoked in most cases when assuming this negligible. To estimate the charge on particles due to tribocharging, the work of Taghavivand et al [95] can offer a starting point. Discussion by Matsuyama [96] on the theoretical maximum charge a given particle can acquire, as a function of material properties and particle size, may be another practical way to evaluate the potential importance of charge effects.

Even without evaluating particle charge one can make scaling arguments on the effect of charge interventions. For example, a reduction in sampling strip charge from ≈ 7 kV to 0.2 kV is expected to reduce the magnitude of the electric field, $E = \frac{dV}{dx}$, by a factor of ≈ 35. This reduction is expected to reduce the size of 'halos' (see Fig. 2.7) on the sampling strips into which no particles were deposited from 1.1x the strip width to 0.03x the strip width, or to be practically negligible.

Summary of Measurement Techniques

Few experiments to date have studied the deposition of mid–range particles, i.e. those at the cross–over between aerosol and ballistic transport properties. To study particles in this range, it is essential to work in a quiescent, well–characterized environment, which takes

significant work and thus is not always provided in otherwise excellent research. To address this gap in knowledge, methods for studying the deposition of droplets and particles were developed.

For studying the deposition of droplets, we explore and find promise in fluorescence–based sampling. Initial findings indicate that the deposition pattern of liquid droplets is strongly dependent on the ambient humidity; additional research is required to explore this relationship further.

Methods for studying the deposition of mid–range sized solid particles (22 - 212 μm) were presented in detail. In preliminary studies on particle deposition from a straight pipe, we noted the extreme sensitivity in particle deposition patterns to the environment. In particular, we noticed that small thermal gradients or electrostatic charge issues can significantly affect the data. We provide practical methods to resolve these issues, including a new method of particle sampling using charge–neutralized adhesive sampling strips; this is coupled with cost–effective analysis utilizing a commercial flatbed scanner. To address thermal drift, we constructed a thermally controlled quiescent chamber. We now can apply these methods for the study of particle transport in a quiescent environment.

Chapter 3

Transport of Particles in a Quiescent Environment

In this section the transport of particles in a quiescent environment is studied. In section 3.1, results are presented for steady state release from a straight pipe. In section 3.2, particle transport from a repeatable cough-type release from a mouth with realistic features is presented.

3.1   Particle Release from a Straight Pipe

Particle release from a straight pipe provides a simpler case for numerical model validation than the releases that are more relevant to respiratory aerosols. For an example of unsteady emissions from models that approach the complexity of human anatomy see section 3.2. For data presented here, particles are released at steady state in fully–developed pipe flow, from an $L/D = 88$ straight pipe with circular cross–section.

Experimental Setup

The particle–laden pipe–flow sets the initial conditions for the jet [97]. We work in the regime for which (a) gravitational settling within the pipe is negligible and (b) the number density of particles is small enough that flow can be assumed one–way coupled. In this set of experiments, a flow rate of 149.6 ± 2.4 slpm passes through a pipe with diameter 9.78 ± 0.02 mm (L/D = 88) for 30 seconds, producing a steady-state jet with an average velocity of 33.2 ± 0.6 m/s. Thus, the pipe–flow Reynolds number was $\approx 21,500$. Uniform particle distribution across the pipe at exit was confirmed with high–speed video of particles. These videos also confirmed that there was no saltation or rolling of particles along the bottom of the pipe.

Given the significant development length for the turbulent jet, the fluid was expected to be ejected in a top–hat velocity profile with nominal velocity of $V = V_{ave} = \frac{Q}{A}$. To confirm that particles were ejected at this same velocity, PTV with volume illumination was used
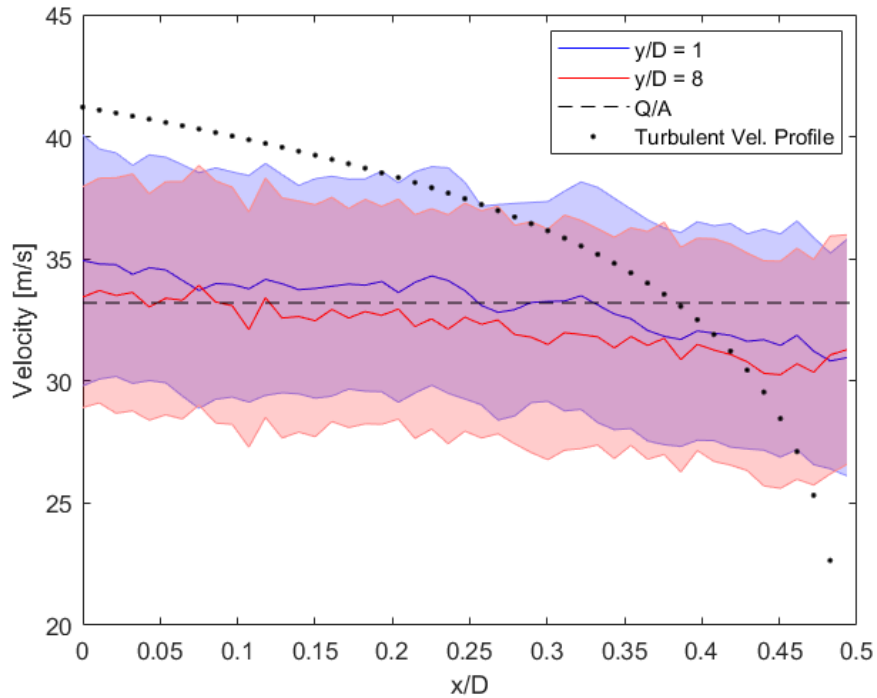
Figure 3.1: Radial profiles of time-averaged streamwise velocity of 180–212 μm particles obtained using PTV. Standard deviation of particle velocities is given by shaded region [1].

to determine the velocity of 180–212 μm particles as they exit the pipe. Results are shown in Fig. 3.1, confirming that despite the large particle size they were ejected essentially at the cross–sectional–average fluid velocity. The plotted data range in the y-direction is determined by the range of particles present in the flow. The average particle velocity across the cross section of the pipe was found in the range $0 \le x/D \le 1$ to be 33.3 $\pm$4.6 m/s, for which the mean compares well to the average fluid velocity of $Q/A = 33.2 \pm 0.6$ m/s. Particles in this range were ejected at an angle of -0.4 ± 1.5 degrees, or nearly horizontal. From the particle velocities seen in Fig. 3.1, it is clear that the largest particles maintain the bulk of their initial momentum $8D$ downstream, demonstrating the ballistic nature of these particles. Smaller particles are expected to even more faithfully follow the flow, and were assumed to be ejected very close to the average gas velocity.

The flow rate reached 90% of the maximum flow rate in 0.6s. Analyzing high speed video footage of the first 9.44s of flow from the pipe, we saw that 90.4% of 180–212 μm particles were ejected after steady–state flow is reached. Thus we conclude that over 90% of the total particle mass was released at steady–state. The steady–state particle release was achieved using the LaVision GMBH "Particle Blaster" which is a stirred canister in which the particles are kept suspended by the flow–through–induced circulation in the cavity. A magnetic stir bar is also available to agitate the contents of the cavity, but was not used

Table 3.1: Standard Particle Load per Experiment

Color	Size(μm)	Mass of Particle Load (mg)	Calculated number of Particles (#)
Green	180-212	25±1	6.3×10^3
Violet	45-53	25±1	4.1×10^5
Red	22-27	25±1	3.7×10^6

because it shattered some of the particles.

Measurements of particle transport will be disrupted if the particles aggregate or gather charge. We prevent aggregation by using particles large enough that the attraction due to surfactants or by Van der Waals Forces has minor effects. To eliminate particle tribocharging, two in-line air ionizers (Simco-Ion 4210u) are placed in series prior to air injection into the particle blaster, the ceramic inside of the particle blaster was lined with copper, tubing from blaster to pipe was minimized and grounded metallic tubing was used where possible.

The lack of aggregation was confirmed at the jet exit by high–speed imaging (without the charge–neutralizing ionizer) and on the sampling strips. The lack of particle charging was confirmed by examining particle deflection on sampling strips charged to ≈ 7 kV. An example of significant particle deflection due to tribocharging is given in Fig. 2.7(a).

To characterize the environment, we have the following inlet and boundary condition data: (1) Velocity at the jet orifice obtained via high–speed video; (2) Temperature for all four walls, ceiling, and floor; (3) Air temperature and RH at two corners of the C^3 interior. Having set these conditions, we measure particle deposition at 35 sites on the floor, using three different particle sizes simultaneously.

Results for Straight Pipe Release

The vertical height of the pipe was 50.2 cm ±0.2 cm, similar to the height of a sitting person's head above a desk or table surface. Ten tests were conducted, for which particle data for each test is summarized in Table 3.1. Wall temperature data is summarized in Table 3.2. Average temperature and relative humidity measurements during each test are summarized in Table 3.3, and show that within the uncertainty of the measurements no temperature or humidity gradients existed in the test chamber while the experiment was being conducted. The configuration of sampling strips used in each of the tests is given in Fig. 3.2.

Deposition results are seen in figures 3.3 and 3.4. The raw particle counts $r_{j,i}$ on strip j in test number i are normalized by the average centerline particle density, $\bar{C}$ (average density across all strips at location $x = 0$). This normalized data $n_{j,i} = r_{j,i}/\bar{C}$ more clearly indicates the relative particle deposition as a function of distance relative to the release point.

The mean particle counts for each location are given in Table 3.4, as well as the standard deviation and relative error. The relative error is an indication of the range in which we expect the true mean to fall, and is computed using the sample standard deviation for each
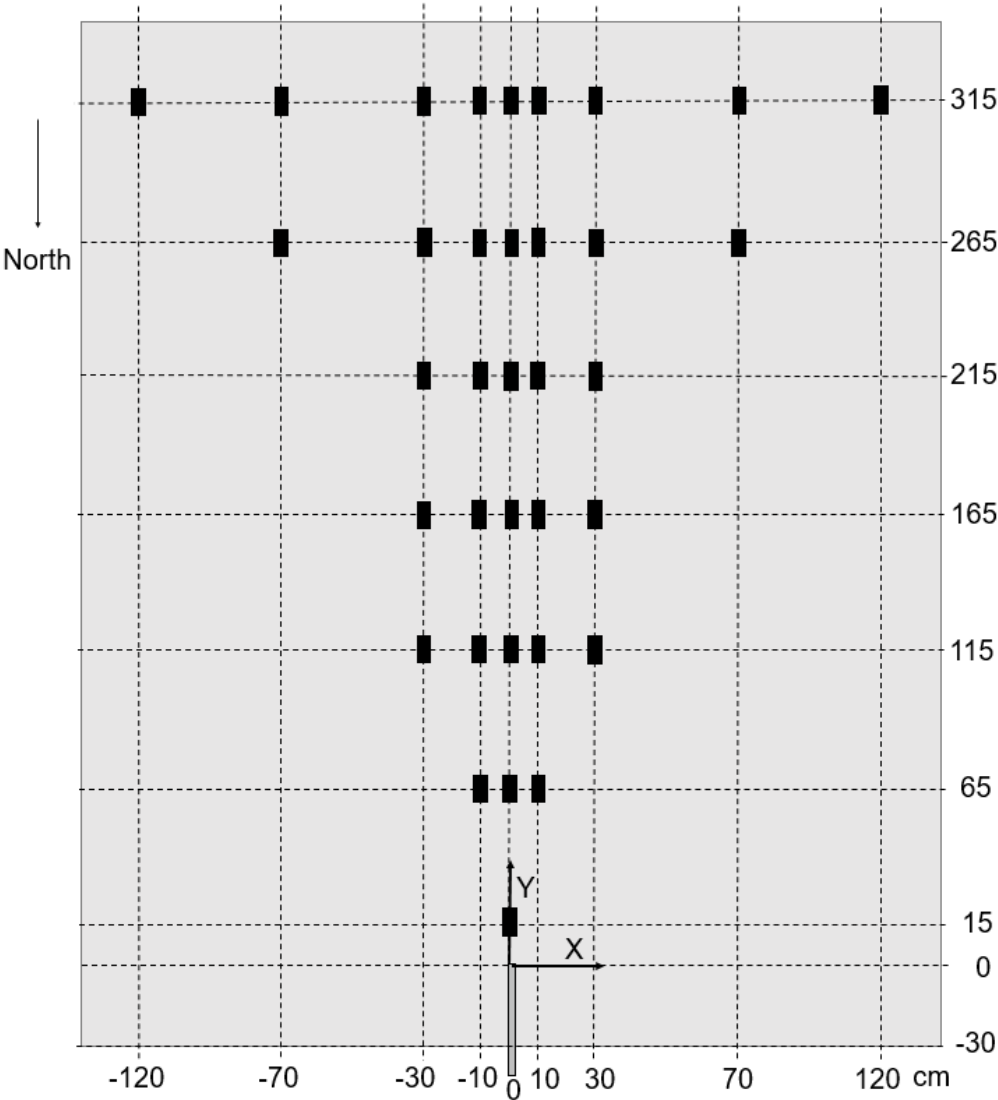
Figure 3.2: Placement of sampling strips for continuous jet experiments [1].
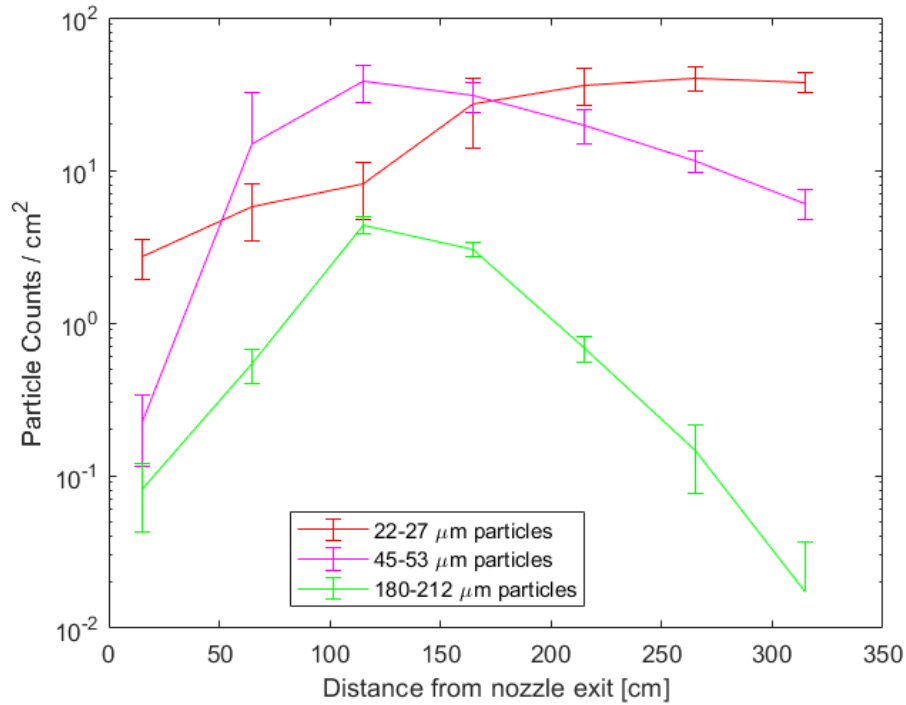
Figure 3.3: Centerline particle concentrations with standard deviation due to test–to–test variation indicated by error bars [1].

strip location, S_j, as follows:

$$\text{Relative Error (\%)} = 100[t_{0.05,\nu}\frac{S_j}{m_{j,10}\sqrt{n}}] \tag{3.1}$$

where $n = 10$ is the number of samples and $t_{0.05,\nu}$ is read directly from a t-table for $\nu = n-1 = 9$ degrees of freedom. In this case a level of significance of 0.05 is used, corresponding to a 95% confidence interval. For strips with a mean of over 5 particles/strip the average relative uncertainty for 22–27 μm particles is 16.4%, 45–53 μm particles is 27.6%, and for 180–212 μm particles is 16.9%.

Discussion of Key Results

The COVID-19 pandemic motivated a number of practical transport studies in a variety of building and environmental airflow configurations. The boundary conditions in practical studies are by definition complex, and the large span of spatial scales (from the particles of interest to the room geometry) ensures that approximations are necessary for the problem to be tractable. The results of the present study highlight the importance of checking the validity of some common assumptions such as how well boundary conditions are defined. We were motivated by the concern that even the most careful treatment of boundary conditions

(a) 22-27 μm particle density.

(b) 45-53 μm particle density.

(c) 180-212 μm particle density.
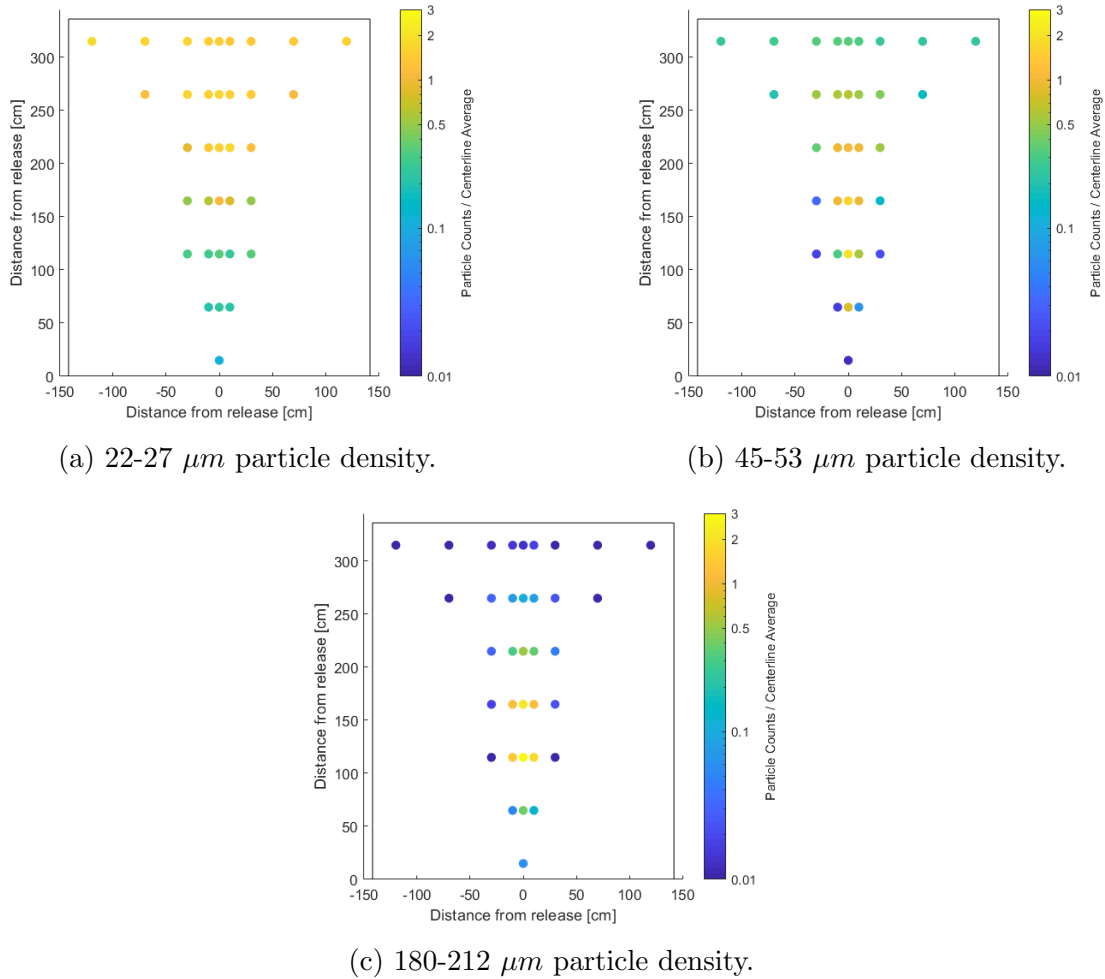
Figure 3.4: Particle deposition results for steady–state jet experiments. (a)-(c) averages across 10 repeat experiments [1].

(an already difficult task) may be insufficient for accurately predicting particle transport. We consider our results a promising message for the scientific community, because our data shows repeatability once we exert a level of environmental control that can be incorporated into many measurement setups.

The particle deposition of particles of different sizes (from nominally aerosol sized 22-27 μm diameter particles to ballistic particles 180-212 μm particles) demonstrates the clear dependence of particle transport on particle size. For a jet velocity of 33.2 m/s, the 180-212 μm particles gradually fell out of the jet and deposited in the centre of the room. For the mid range 45-53 μm particles, the peak particle deposition intensity was in the centre of the room. However, some particles were carried forward to the end of the room and were dispersed laterally due to interaction between the jet and the end wall. For the smallest particle size, the end wall effects (while secondary in terms of the jet structure) had a significant impact

on particle dispersal. The significant residence time of these particles ensured that secondary flows from jet/wall interaction were still sufficiently large to be vectors of lateral dispersal.

A comparison to computational fluid dynamics (CFD) results of the same experimental conditions is given in Thacher et al [1]. This comparison reinforces the complex issues involved with modeling the deposition of mid–range and ballistic–sized particles. Even when matching the quiescent background (despite the lack of flow obstructions, thermal gradients, particle evaporation, or electrostatic effects), there are clear areas in which more advanced CFD tools are needed to match the observed particle distribution. One is the turbulent transport of particles, in which particle clustering and/or anomalous diffusion (also called pre–Fickian or scale–dependent diffusion) can be important for certain points jet and particle conditions. Another is the interaction of the jet with walls and floors, which can be addressed through advanced CFD treatment of near–wall flows. CFD studies which attempt to model unstable and highly transient jet flows (such as a human cough) or capture effects such as evaporation must take additional care in ensuring that these effects are captured accurately.

The growing application and development of advanced CFD tools ensures that suitable experimental studies are needed for model validation, but as discussed in Section 2.1 such studies do not yet exist for practical geometries. Model validation experiments should carefully characterize or eliminate thermal gradients, ambient flows and charge effects. Methods for studying particle deposition must be accurate across a wide range of particle sizes, which is challenging with optical methods. The steps needed (e.g. room and sampling strip charge neutralization, and significant thermal insulation) suggests that in many studies that did not explicitly consider such effects and go to great lengths to mitigate them, results should be viewed cautiously with appreciation of the effects that may have influenced the data yet not been described. We hope that future studies can build on the methods presented in this paper to improve the quality of available validation studies. In the meantime, we hope that experimental studies in simplified geometries (such as the data presented in here) see increased use in numerical model validation, as predicting mid–size particle transport is shown to be highly non–trivial.

Raw Data for Steady State Particle Release

The wall temperatures are given in Table 3.2. The interior temperature relative humidity measurements for each test are given in Table 3.3. The absolute particle concentrations measured at each sampling strip are given in raw number of particle counts in Table 3.4. This is included to facilitate use of the data set for CFD code validation. It is advisable to compare to deposition value normalized by the maximum or the center line average (as in Fig. 3.4), as the true number of total particles deposited on the floor is largely unknown. While the number of particles injected to the launch apparatus is well-characterized (see Table 3.1), particles may be trapped in the ejection apparatus (either pipe or particle blaster), and may deposit in regions that are significantly under-sampled (such as far edges or walls of C^3).

Table 3.2: Wall temperatures prior to test.

Experiment	N wall (°C)	W wall (°C)	S wall (°C)	E wall (°C)	Floor (°C)	Ceiling (°C)
1	23.8	24.0	23.8	23.6	23.0	23.3
2	24.4	24.6	24.6	24.6	24.3	24.6
3	24.8	24.8	24.7	24.8	24.8	24.9
4	24.4	24.6	24.4	24.5	24.4	24.5
5	24.7	24.5	24.5	24.5	24.3	24.4
6	24.3	24.7	24.4	24.4	24.4	24.6
7	24.1	24.2	24.2	24.2	24.1	24.5
8	24.3	24.1	24.4	24.1	23.9	24.2
9	24.0	24.0	24.2	24.0	23.7	24.1
10	23.9	24.4	24.1	24.1	23.6	23.8

Table 3.3: Interior temperature and relative humidity data during test.

Experiment	NW Temp. (°C)	NW RH (%)	SE Temp. (°C)	SE RH (%)
1	21.5	39.8	21.5	40.1
2	22.2	41.5	22.3	41.3
3	22.8	36.4	22.8	37.2
4	22.4	52.5	22.4	53.5
5	22.5	51.4	22.4	52.8
6	22.3	36.8	22.3	38.0
7	22.3	41.7	22.2	43.1
8	22.1	35.0	22.1	35.8
9	22.1	41.4	22.1	42.5
10	21.9	40.4	21.9	41.4

3.2   Particle Release from an Intubation Trainer with a Realistic Mouth Geometry

In section 3.1, we see that particle size had a significant impact on dispersal. The primary differences were the location of particle fallout and the effect of wall/jet interaction on lateral dispersal. However, we would now like to study the effect of a realistic oral cavity on particle dispersal in the same size range. As described in section 1.1, it has been shows that small particles with high density ratio preferentially accumulate in regions of high strain rate and low vorticity. The tendency of particles to cluster is scaled in work by Hunt as a modified Stokes number [85]:

$$S_t^* = \frac{V_T^2 t_P}{\Gamma} \tag{3.2}$$

This follows from the particle Froude number defined in [17], $Fr_P = V_T^3/g\Gamma$. The two are seen to be equivalent when noting the terminal velocity to be $V_T = gt_P$. When $S_t^* \leq 1$, we expect that particles have sufficiently low inertia to be affected by vortices present in the flow

Table 3.4: Raw deposition data listing average number of particles per 51.6 cm^2 strip centered at the given x and y location.

x [cm]	y [cm]	22-27 μm			45-53 μm			180-212 μm		
		average counts	std. dev	Relative Error %	average counts	std. dev	Relative Error %	average counts	std. dev	Relative Error %
-120	315	2230	446	11.6	237	48	11.7	0.1	0.3	183.3
-70	265	1484	433	16.9	193	132	39.7	0	0.0	
-70	315	2036	449	12.8	257	61	13.7	0	0.0	
-30	115	392	125	18.4	16	8	31.2	0.3	0.7	130.4
-30	165	573	139	14.1	30	10	20.5	1.2	1.1	54.8
-30	215	1087	405	21.6	338	226	38.8	2.1	2.0	55.9
-30	265	2037	389	11.1	487	187	22.3	2	1.7	49.3
-30	315	2043	463	13.1	326	107	19.0	0.8	1.0	74.8
-10	65	243	71	16.9	15	6	22.0	3.4	2.1	35.2
-10	115	344	111	18.7	295	396	77.8	96.8	26.0	15.6
-10	165	807	233	16.7	918	314	19.8	83.2	14.9	10.4
-10	215	1745	602	20.0	909	393	25.0	21.7	5.1	13.6
-10	265	1998	360	10.5	556	136	14.2	5	3.3	38.3
-10	315	1949	451	13.4	308	87	16.4	1	1.2	72.3
0	15	141	42	17.1	12	6	28.2	4.2	2.0	27.5
0	65	299	122	23.8	767	904	68.4	27.9	7.0	14.6
0	115	417	169	23.5	1961	541	16.0	227.3	29.8	7.6
0	165	1393	674	28.0	1583	344	12.6	157.3	16.4	6.0
0	215	1875	511	15.8	1023	255	14.4	35.5	6.8	11.1
0	265	2083	364	10.1	596	95	9.3	7.5	3.6	27.6
0	315	1955	286	8.5	313	69	12.8	0.9	1.0	64.1
10	65	276	96	20.1	55	104	110.1	8.9	3.7	24.3
10	115	332	106	18.6	553	445	46.6	129.6	16.8	7.5
10	165	1060	657	35.9	988	200	11.7	87	22.4	14.9
10	215	2046	655	18.6	929	330	20.6	24.8	9.6	22.3
10	265	1973	370	10.9	513	91	10.3	5.4	2.1	22.7
10	315	1851	255	8.0	296	63	12.3	1.2	1.0	49.9
30	115	415	133	18.6	19	9	28.0	0.2	0.6	183.3
30	165	603	187	17.9	129	128	57.6	1.5	1.6	63.8
30	215	1523	846	32.2	522	364	40.4	2.9	2.1	41.6
30	265	1840	409	12.9	405	108	15.4	1.5	1.2	45.5
30	315	1732	144	4.8	254	64	14.7	0.5	0.7	82.0
70	265	1364	291	12.4	137	73	30.7	0	0.0	
70	315	1711	341	11.6	223	64	16.5	0	0.0	
120	315	1909	352	10.7	215	65	17.6	0	0.0	

[85]. It remains to show that vortical flows with circulation on the order of $V_T^2 t_P$ are present in a cough-type event. If so, particles are expected to be affected by circulation present in the flow, and it is important to ensure that the flow field near the mouth is prescribed accurately in modelling or experiments.

To produce a 3D flow field, we use a repeatable cough generator with a realistic oral cavity. The inclusion of teeth, tongue, and lips in the oral cavity provides a marked addition to the data available in literature. To focus the experiments on mouth geometry effects, the coughed air was at ambient temperature and solid particles were released instead of liquid droplets. These choices allow us to ignore the effects of buoyancy and evaporation on droplet transport. We will see from measurements of the simultaneous transport and deposition of particles from 22 to 212 μm that the 3D nature of the flow field has a significant effect on particle deposition.

This work addresses the gap in previous literature on the influence of mouth geometry on particle transport that was identified in section 2.1. This section closely follows the work done by Thacher et al [3].

Experimental Setup and Characterization of Inlet Boundary Conditions

Experiments were conducted in the Cal Covid Cube, which is described in 2.2. Repeatable cough-type events were produced from an intubation trainer doll with a realistic mouth geometry (3B Scientific, item 1005596). The height of the center of the doll mouth is at $z = 160 \pm 0.2$ cm above the floor. An image of the mouth and coordinate system is given in Fig. 3.6a, for which the x-axis is coming out of the page. Fluorescent polyethylene microspheres from Cospheric (Table 3.5) were placed in a particle 'trap' and a controlled air release carried the trap contents in a multi-phase turbulent puff. The particle trap is a set of two flanges with a fine wire mesh, upon which particles could be placed. As air passed through the trap the particles were suspended in the flow, and carried into the artificial airways of the doll as a turbulent puff. The doll and particle trap are shown in Fig. 3.5

After passing through the particle trap, the puff travelled through an artificial trachea and oral cavity, which included teeth, tongue, and lips. The nasal cavity was blocked off at the back of the throat between the oral and nasal pharynx. The controlled air release lasted 1.0 s, with a nominal peak flow rate of 150 slpm. The airflow was generated via a release from a 22.7 liter tank. The air released from each cough was < 2 % of the stored air volume, and a regulator provided the gas at a constant pressure (≈ 380 kPa) to an Alicat mass flow controller (MCR-2000SLPM). The Alicat has a reported uncertainty of $\pm$ (0.8% of reading + 0.2% of full scale). The flow rate was recorded directly from the Alicat using a National Instruments myDAQ. The volume of air released during the cough was determined to be highly repeatable, with a volume of $Q = 1.23 \pm 0.09$ litres, which is within the range of 0.4–1.6 litres for male subjects given by [62]. The repeatability of the air release volume was determined as an integral of the flow rate across 64 coughs. However, it is important to

<div align="center">(a) Intubation trainer doll.   (b) Bottom of particle trap.</div>
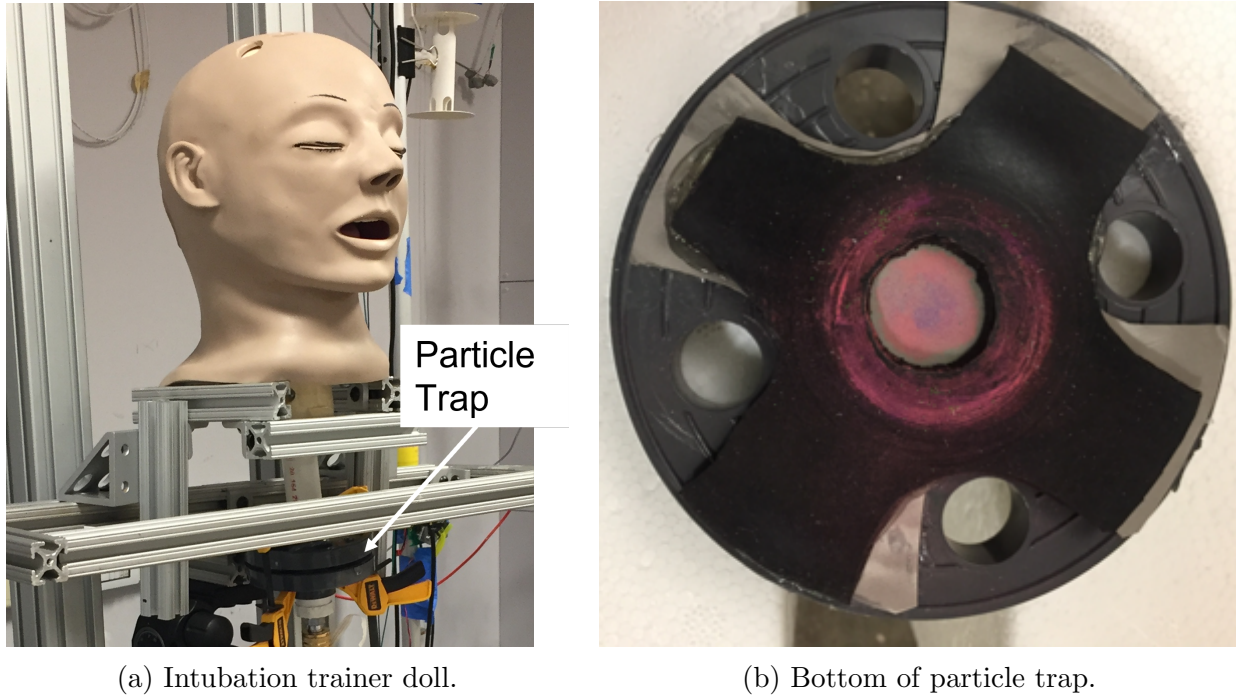
Figure 3.5: Intubation trainer doll and particle trap used to produce repeatable cough-type events.

note that the absolute value of the released volume is subject to the finite accuracy of the flow meter as stated above. The flow rate during the cough was controlled with the Alicat using a PID controller.

The mouth opening area is approximately an ellipse with a major axis of a = 2.25 cm $\pm$ 0.07 cm and a minor axis of b = 0.725 $\pm$ 0.07 cm. This corresponds to an equivalent diameter of $D_e = 2\sqrt{ab} = 2.55$ cm, and an opening area of $A_{exit} = 5.1$ cm^2, which is slightly larger than the average of 4.00 $\pm$ 0.95 cm^2 reported in [62]. The nominal Reynolds number of the turbulent puff computed using the average flow rate is $Re = \frac{QD_e}{A_{exit}\nu} \approx 4100$, where ν is the kinematic viscosity of the air (taken to be 1.5 x 10^{-5} m^2/s). The average cough velocity along the $y = 0$ plane is given in Fig. 3.7b, for which a snapshot of the particle release at the inset location is given in Fig. 3.7a. The cough trajectory is characterized by the two angles given in Fig. 3.7b, which can be compared to the expected values of $\theta_1 = 15° \pm 5°$ and $\theta_2 = 40° \pm 4°$ reported in [62]. The angle is also shallower than the approximate mean angle of 30° reported by [59], however it is noted that the angle varies with each subject as well as their body positioning.

Characterizing Velocity Distribution Downstream

Point-wise flow measurements were made using a single omnidirectional hot-wire (Dantec Dynamics 55P16). Calibration of the hot wire bound the uncertainty to 5.6% across a

(a)   (b)
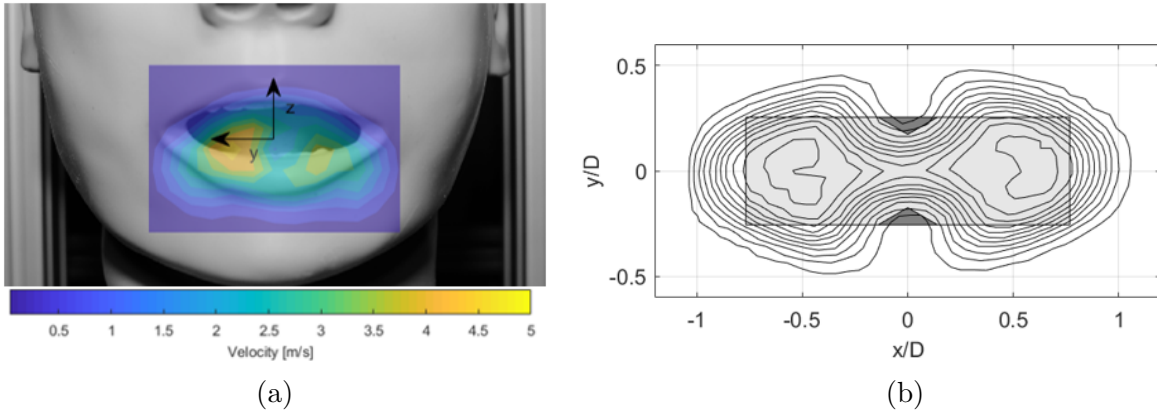
Figure 3.6: Velocity contours in $x/D_e = 1$ plane from (a) realistic geometry and (b) canonical rectangular slot with tabs (figure re-created based on Zaman [2]) [3].

velocity range of 0 - 12.2 m/s. The hot wire was traversed in x, y and z to a total of 654 unique locations, for which a minimum of three repeated measurements spanning the cough duration were made. The measurement locations are shown in Fig. 3.10. The velocity measurements were made at 5 kHz. Time-averaged velocities from $0.1\,\text{s} \leq t \leq 1\,\text{s}$ of the 1.0 s cough were computed, and the average of these velocities across the repeated measurements are what is reported here. No particles were present during the hot-wire measurements. As the cough is generated from a static geometry and a highly repeatable gas delivery system, ensemble averages of the flow field could be reported. The volume of air ejected during each cough was highly consistent with a 1.23 ± 0.09 litre released volume. While velocity at a given location fluctuates in time due to both turbulence and large coherent structures in the flow, the time-averaged velocity measurements across all locations had a mean standard deviation of 0.06 m/s. For measurements in the $z = -b$ plane, the average standard deviation of the time-averaged measurements was only 12% of the mean velocity. While additional physics may be contained within time-resolved measurements, we choose to approach the problem from a Reynolds-averaged perspective as this aligns with typical modelling practice.

Contrary to previous studies which report only the centerline ($y = 0$) profile and normalize by the maximum velocity, examining the flow beyond the centerline plane reveals that the cough forms two jets (seen in Fig. 3.6a). The jets are centered on either side of the $y = 0$ plane and below the $z = 0$ centerline due to the downward cough trajectory, and hence would have been missed in studies where only the centerline plane was characterized (even with realistic oral geometries). The likely cause of formation of the two jets is the tongue structure within the mouth, leading to a split in the flow. Similar formation of two parallel jets due to a partial blockage was reported for a canonical rectangular outlet geometry by Zaman [2]. The contours of mean velocity for flow through the rectangular opening with tabs is shown in Fig. 3.6b. The similarity between the two flows in the $x/D_e = 1$ plane is apparent. While the formation of two jets still needs to be verified with human subject experiments, the work of Zaman [2] shows that even an area blockage area of 1.8% is sufficient for two

(a)

(b)
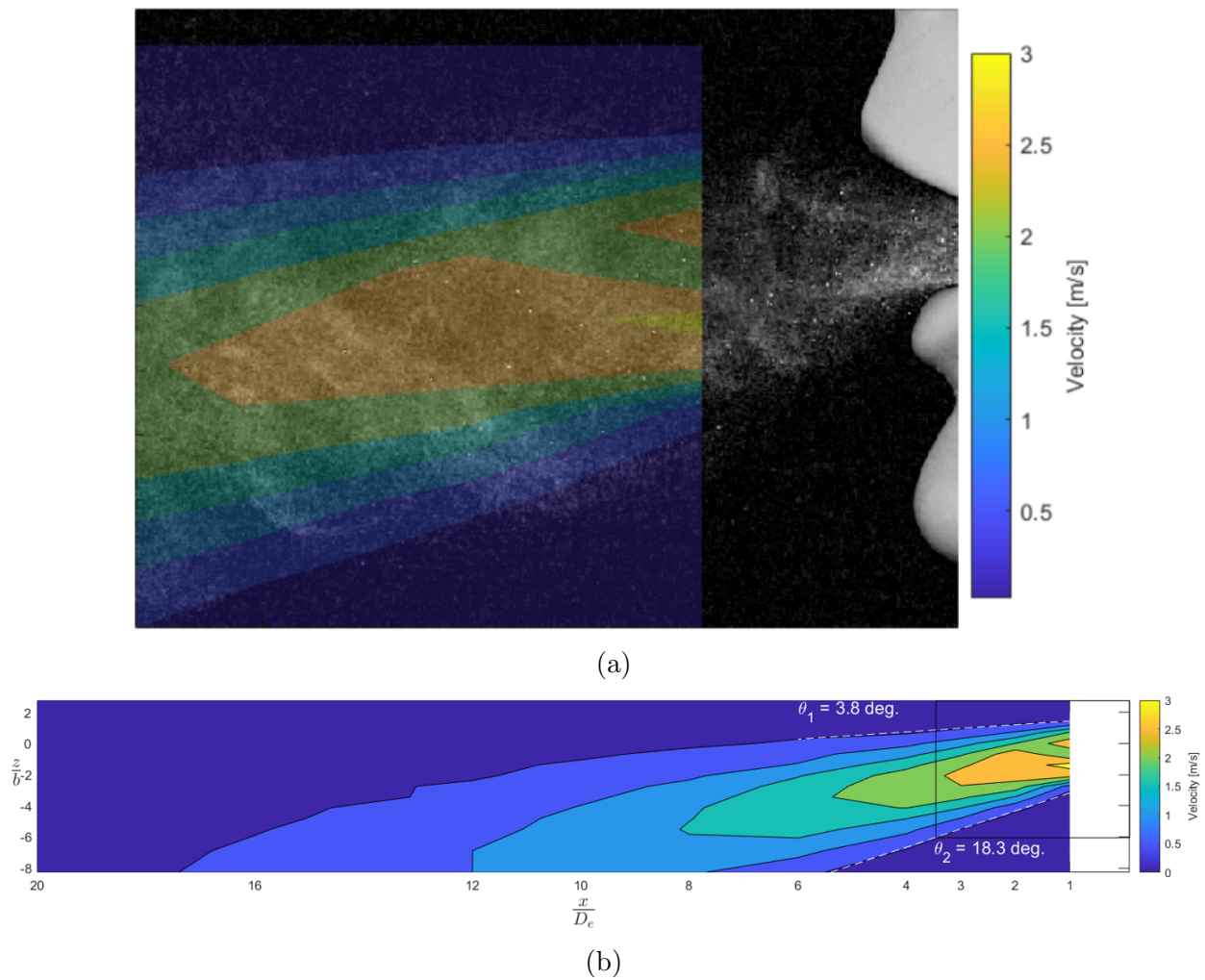
Figure 3.7: (a) Snapshot of particle release during cough with contours of average velocity in the $y = 0$ plane superimposed. (b) Average velocity contours in $y = 0$ plane with angle of cough boundaries indicated. The boundary is defined by points at which the velocity is below 0.5 m/s, or less than 10% of the maximum jet velocity of 5 m/s [3].
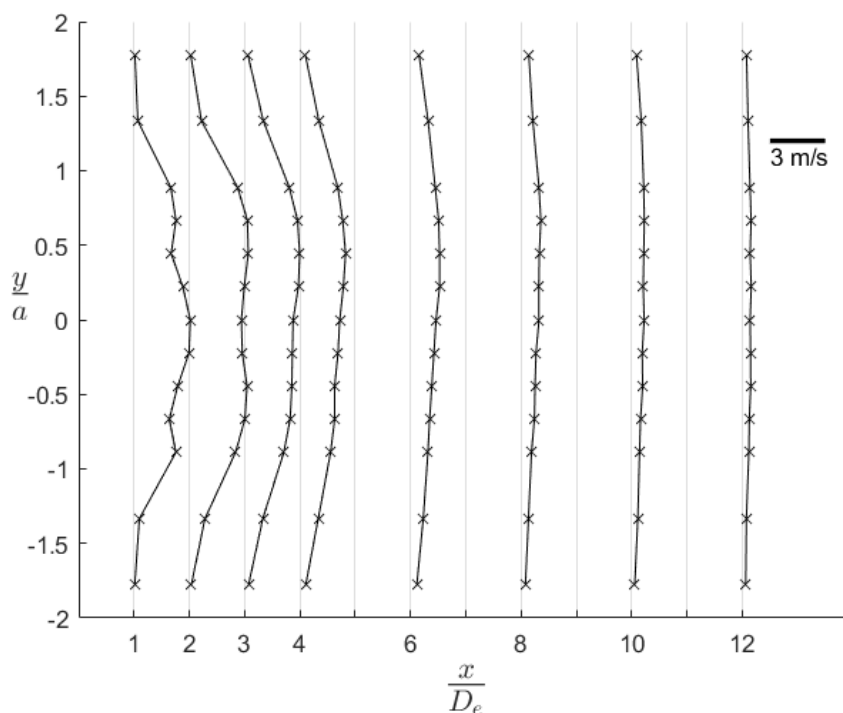
Figure 3.8: Downstream velocity profiles along z/b = -1 plane [3].

jets to form. Therefore, it seems likely that the two jets are present in at least a subset of human coughs. In these cases, a round jet would make a poor approximation of the true flow field.

Since the mouth is not perfectly symmetric, the strength of the jets are not equal and have time-averaged velocities of 5.0 m/s and 3.9 m/s at a distance of x/D_e = 1 from the mouth. The two-jet pattern leads to the formation of a shear layer downstream (see Fig. 3.8). This velocity profile downstream, including the shear layer formation, appear qualitatively similar to those found in human-subject experiments by Han et al [81]. Again, this serves to illustrate the relevance of the present work to human coughs despite the use of an intubation trainer doll in these experiments.

To illustrate the 2D velocity profile along the downward angled cough trajectory, we provide the time-averaged velocity profile in Fig. 3.9.
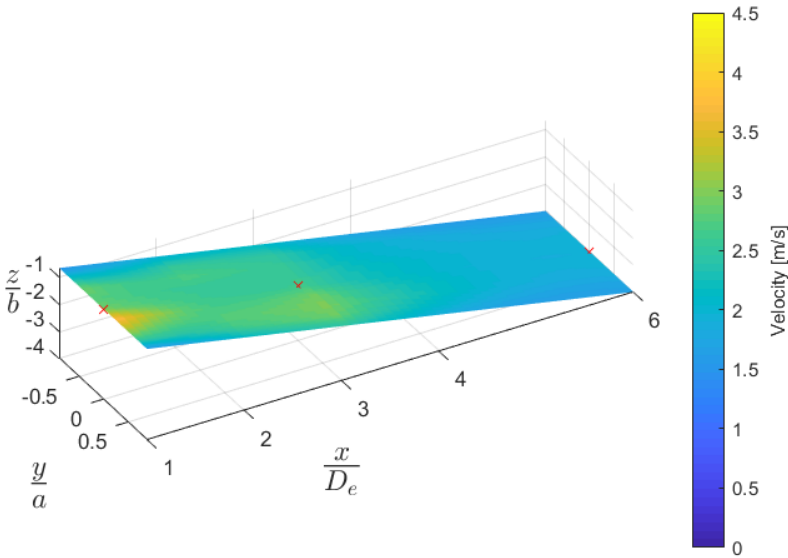
Figure 3.9: Velocity profile based on interpolation of hot wire data along angle of -10.75°. Locations of time-resolved velocity profiles provided in Fig. 3.11 are indicated by red [3].

The time-averaged profile is interpolated from the hot-wire measurements made across all measurements in Fig. 3.10.
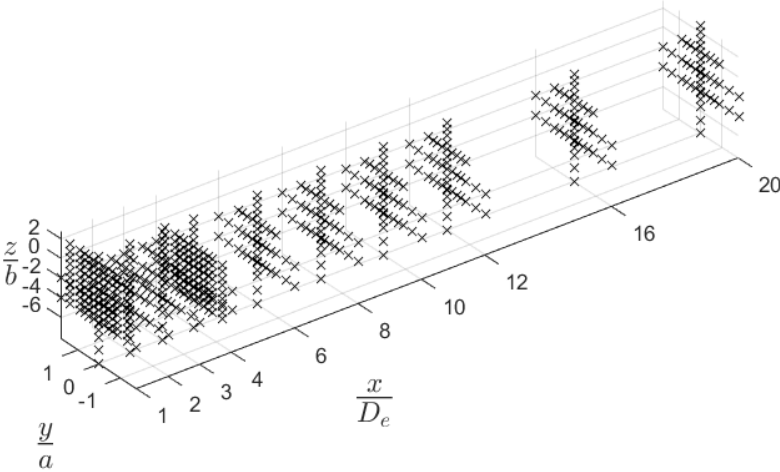
Figure 3.10: Hot wire measurement locations [3].

To aid modelers in replicating the time-resolved flow field Fig. 3.11 provides time-resolved velocity data at three locations as well as the flow rate profile to the mouth. The time-resolved velocity measurements are ensemble averaged using six measurements at the $\frac{x}{D_e} = 1$, $\frac{z}{b} = $ -0.7 location and four measurements at the other two locations. The flow rate was ensemble averaged across 64 measurement instances. The fluctuations in the flow rate result from the mass flow controller trying to track a stepwise change in the target flow rate, but these are highly repeatable as evident from the narrow standard deviation based on ensemble of the data. While these fluctuations influence the velocity magnitude, the velocity difference to either side of the mouth persists throughout the fluctuations, indicating that the shear layer also persists in the time-resolved measurements.
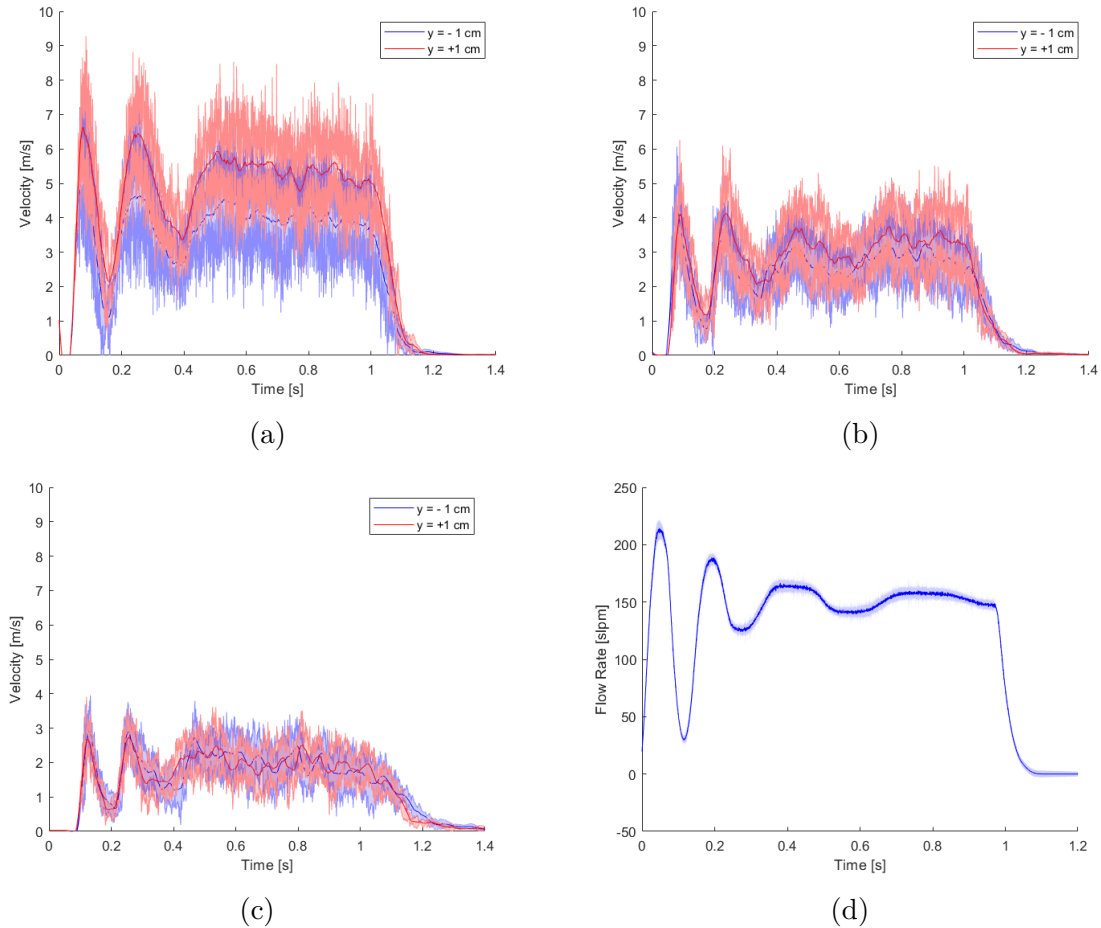
Figure 3.11: (a) Time-resolved velocity measurements at $y = \pm 1$ cm (either side of the centerline) showing the shear layer at $\frac{x}{D_e} = 1$, $\frac{z}{b} = $ -0.7, (b) $\frac{x}{D_e} = 3$, $\frac{z}{b} = $ - 2 (c) $\frac{x}{D_e} = 6$, $\frac{z}{b} = $ - 4, (d) Flow rate during ejection period. The standard deviation of the measurement (based on ensemble data at any given instant) is given by shading [3].

Table 3.5: Particle load (mass per size class) used for each experiment. The particles nominally had density of water ($\approx$ saliva), $\rho = 1 \pm 0.01$ g/cm^3

Color	Size (μm)	Mass (mg)	Calc. nb. of Particles (#)
Green	180-212	25±1	6.3×10^3
Violet	45-53	25±1	4.1×10^5
Red	22-27	25±1	3.7×10^6

Result for Particle Ejection from Realistic Geometry

While the repeatable cough generator doesn't capture changes to the cavity shape during a cough event [98], it includes many of the salient geometrical features and exposes how these may result in a more complex flow field than what is typically assumed (such as the flow field from a round or elliptical pipe release). Subsequently we describe the effect of this flow field on particle transport. Solid fluorescent color-coded particles were released to enable the simultaneous deposition of three particle sizes spanning an order of magnitude and exhibiting no coalescence or ambiguity in the original droplet size. Additionally the co-flowing air was kept nominally at room temperature, so that buoyancy would not affect the flow. While buoyancy and evaporation are important for particle transport in a real cough, neglecting these influences allows the effect of the mouth geometry to be studied independently of conflating factors.

To measure deposition, 102 mm x 51 mm adhesive TriTech vinyl backed sampling strips were placed at 46 locations on the floor. The strips were charge-neutralized (using Simco-Ion 5225 AeroBar with the neutrality inspected using the Simco-Ion FMX-003 electrostatic fieldmeter) prior to each experiment. Section 2.4 provides further detail of the experimental and data analysis technique. The particle identification rate with this method is greater than 98%, with a false positive rate below 2%. Notably, this error is significantly lower than the test–to–test variation. The mean, standard deviation, and relative error due to test–to–test variation for each location is given in section 3.2. Reported mean particle density (given in Fig. 3.12 and in further detail in section 3.2) is the average of eight repeated experiments.

To determine the effect of the shear layer on particle displacement, the modified Stokes number is computed according to eq. 3.2 with the vortex strength estimated as $\Gamma = \Delta U(x)\lambda(x)$. The equation for vortex strength is computed using the definition of circulation in a plane shear layer (as in [99]), but with a modified definition of $\Delta U(x)$. The characteristic velocity, $\Delta U(x)$, is defined as the difference in velocity evaluated at y = $0.5\lambda(x)$ and y = $-0.5\lambda(x)$ (to either side of the y = 0 centerline). This is in contrast to the definition given by Jimenez [99], who define the characteristic velocity as the velocity difference between the free jet and surrounding quiescent fluid. This change in the characteristic velocity scale is due to the steeper velocity gradient in the primary shear layer of the present experiments (within the cough and contained near the centerline). We assume that this shear will dominate the formation of coherent structures, as opposed to the shear layer caused by the interaction with the quiescent fluid external to the cough structure. $\lambda(x)$ is the large-structure wavelength
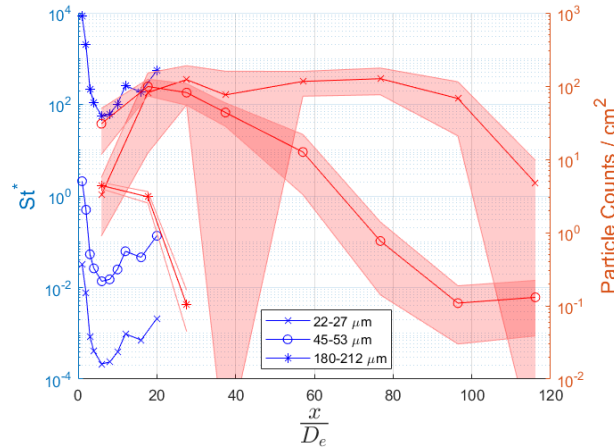
Figure 3.12: Modified Stokes number, St^*, along the horizontal $z/b = $ -1 plane and centerline particle concentration, with standard deviation due to test-to-test variation given by shaded error bars [3].

computed according to $\lambda/x = C\alpha$, where the constant $\alpha = (U_1 - U_2)/(U_1 + U_2)$. This constant is computed using the initial velocity to either side of the centerline, such that for $U_1 = 5$ m/s and $U_2 = 3.9$ m/s, $\alpha = 0.12$. The constant C defines the spreading rate of the large-scale streamwise wavelength, and was determined empirically [99] to be $C = 0.561$. This value matches closely with that from [100] for a plane shear layer produced by a finite velocity difference, ΔU. The constant spreading rate likely arises from the constant ratio between the spanwise and streamwise wavelengths in a plane shear layer [101]. The spanwise wavelength is also linearly dependent on x, and grows 1 to 1.5 times faster than the vorticity thickness [99]. This approximation of the vortex strength enables an estimate of the order of magnitude of the modified Stokes number as a function of streamwise distance and particle diameter (Fig. 3.12.)

For $St^* \leq 1$ the particles have sufficiently low inertia to be affected by the vortices produced in the shear layer. This criteria is never satisfied for the largest $\approx 200\mu m$ particles, which are deposited as ballistic projectiles. While the estimate of circulation only provides a rough approximation of S_t^*, the $22-27$ μm and $45-53$ μm particles are predicted to be affected up until at least a distance of $20D_e$ downstream (Fig. 3.12b). Still further downstream it is predicted that the $22-27$ μm particles will continue to be strongly affected by the shear layer. The locally high standard deviation of $22-27$ μm particle counts at $x = 37.4D_e$ gives some indication of where particle-vortex interaction led to high test-to-test variation.

The 'eddying pattern' seen in the deposition of $22-27$ μm particles from a single experiment shows the 'frozen signature' of the flow structure (Fig. 3.13a). This false colour image was created from a picture obtained using a 495 nm longpass filter while illuminating the fluorescent particles with UV light. The pattern seen in the image was corroborated

(a)   (b)
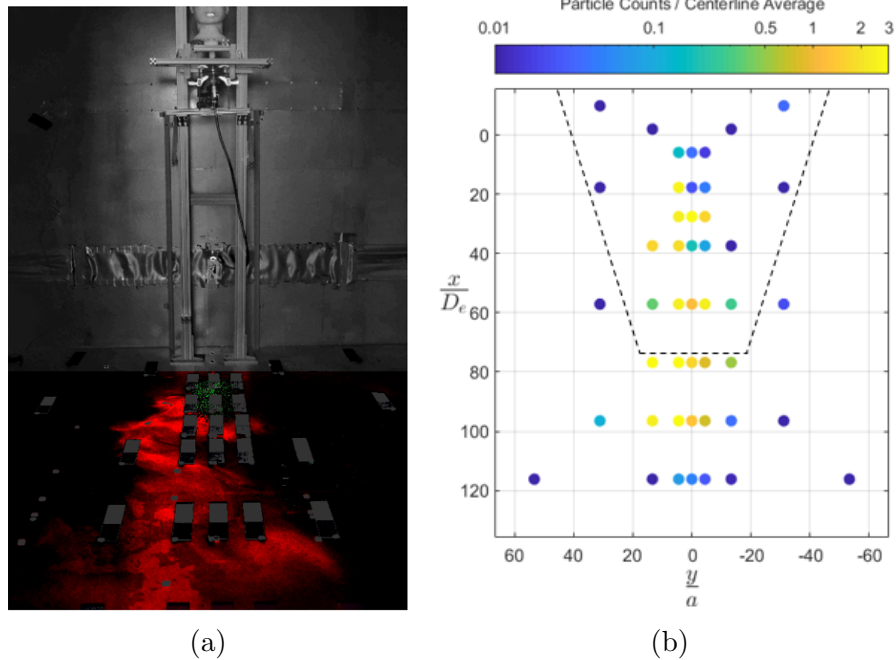
Figure 3.13: Comparison of (a) false colour image of $22 - 27$ μm (red) and $180 - 212$ μm (green) particle deposition with (b) measured $22 - 27$ μm particle deposition during a single experiment with image view indicated by dashed line [3].

with quantitative deposition data (Fig. 3.13b). This data provides a strong indication that particles are affected by the free shear layer. The eddying is most apparent in the near field, up to $x \approx 50D_e$, after which particle deposition appears to be relatively uniform across the span. The effect of eddying is also clear in the particle deposition counts, for which the row at $x = 27.6D_e$ received high particle counts while the centerline strips at the $x = 17.7D_e$ and $x = 37.4D_e$ had particle counts that were an order of magnitude lower. This result demonstrates that the spanwise shift in particle deposition due to the particle-vortex interaction in the free shear layer has a first-order effect on the particle deposition location. This large scale pattern would not have been expected from a single round jet release.

The mean particle deposition as a function of position is given in Fig. 3.14. As could be expected, the smaller particles considered travel further in the streamwise direction. Spanwise particle dispersion is also inversely related to particle diameter, indicating an increase in the effective 'diffusivity' of smaller particles. While eddying effects from particle interaction with the free shear layer are smoothed out when averaged across multiple experiments, the mean deposition results are valuable for numerical comparison studies using this dataset.
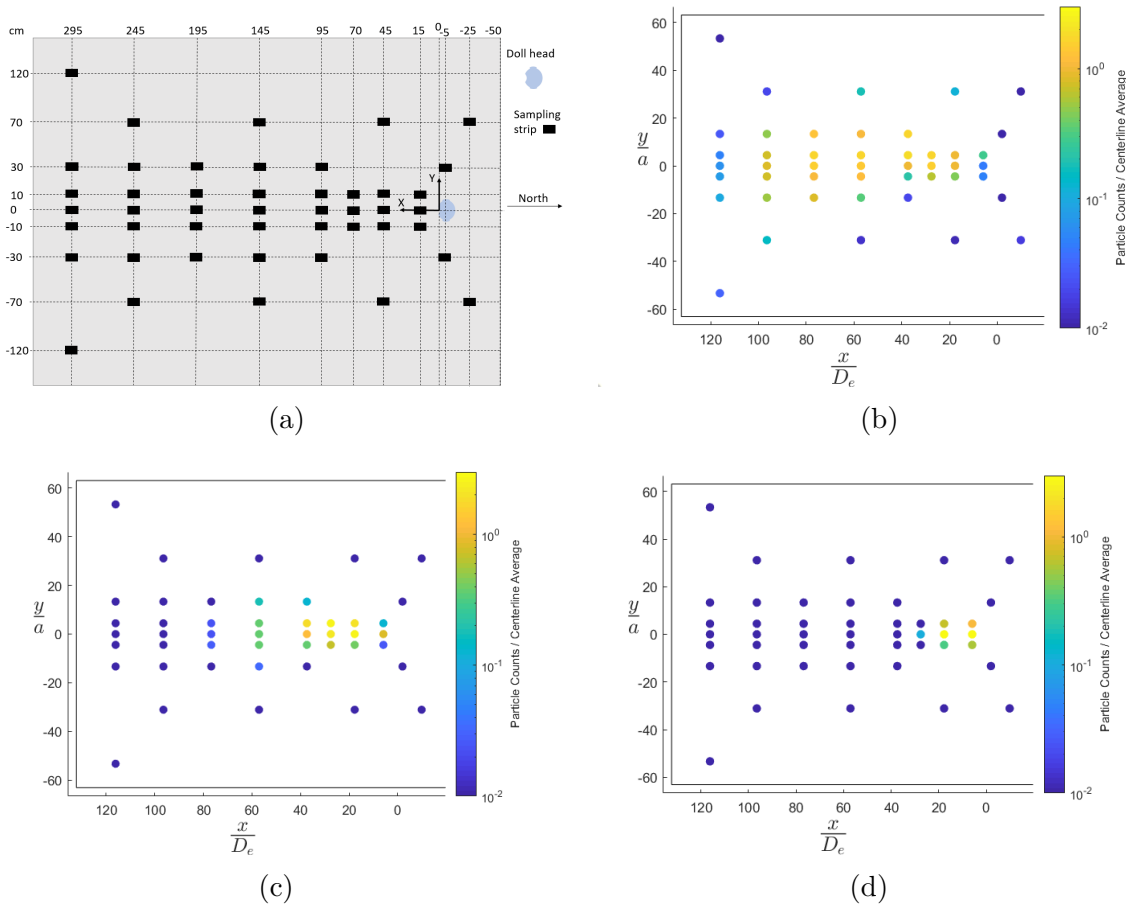
Figure 3.14: (a) Layout of sampling strips; Particle deposition of (b) $22 - 27~\mu m$ particles, (c) $45 - 53~\mu m$ particles, (d) $180 - 212~\mu m$ particles normalized by average centerline concentration [3].

Discussion of Key Results

The data suggests a clear effect on particle deposition from the cough release geometry, which is in agreement with what is expected given the modified Stokes number of the released particles. The eddying pattern seen in Fig. 3.13b was present in repeated experiments up until $\approx 50 D_e$ downstream (approximately 1.3 m away from the mouth). As circulation decreases exponentially downstream, the pattern fading further downstream lends further support for the presented interpretation of the data. There will still be a 'far field' distance at which the effects of the oral cavity geometry can be neglected. As a first approximation this distance can be described as the point at which $S_t^* \gg 1$, which indicates the dependence of the 'far field' criteria on the particle size. Beyond this distance the inlet boundary condition (ie. complex oral cavity) no longer affects particle transport. In this 'far field' region, a more general approximation of the flow field is likely sufficient, provided that the initial

preferential clustering of particles has been accounted for. Notably, the majority of droplets ejected during a real cough rapidly evaporate to an equilibrium diameter and are smaller than what was considered in the present study [64, 63]. Therefore, the majority of droplets ejected during a real cough could continue to be affected by the complex mouth geometry much further downstream than the particles in the present study.

Consequently, studies that are attempting to predict particle transport on the order of typical social distancing (recommended social distancing guideline is 1.8 m (6 ft) as given in [102]) between individuals should consider the oral cavity as something more complex than a plain round or elliptical orifice when predicting the flow field and resulting particle transport.

Raw Data for Particle Deposition from Intubation Trainer

In an effort to provide as much data as possible for reproducing these results, the raw deposition data for each location is given in Table 3.6. For each location j the mean, m_j as well as the standard deviation, s_j, is reported as well as the relative error, defined as:

$$\text{Relative Error (\%)} = 100[t_{0.05,\nu}\frac{s_j}{m_j\sqrt{n}}] \tag{3.3}$$

where $n = 8$ is the number of samples at each location and $t_{0.05,\nu}$ is read directly from a t-table for $\nu = n - 1 = 7$ degrees of freedom. In this case a level of significance of 0.05 is used, corresponding to a 95% confidence interval.

Table 3.6: Raw deposition data listing average number of particles per 51.6 cm^2 strip centered at the given x and y location.

		22-27 μm			45-53 μm			180-212 μm		
x [cm]	y [cm]	average counts	std. dev	Relative Error %	average counts	std. dev	Relative Error %	average counts	std. dev	Relative Error %
-120	295	123.6	158.0	85.6	4.4	3.8	58.4	0.0	0.0	
-70	-25	64.5	60.1	62.4	11.1	6.7	40.6	0.0	0.0	
-70	45	42.5	24.3	38.3	11.1	7.3	43.8	0.0	0.0	
-70	145	52.6	43.9	55.9	6.3	3.1	33.3	0.4	1.1	189.5
-70	245	613.0	1018.9	111.3	4.1	1.6	25.2	0.0	0.0	
-30	-5	31.6	15.8	33.6	7.9	3.7	31.6	0.0	0.0	
-30	95	74.5	119.3	107.3	11.5	8.1	47.0	0.0	0.0	
-30	145	1370.8	1992.8	97.4	58.1	107.4	123.8	0.0	0.0	
-30	195	3361.8	1937.3	38.6	16.5	11.9	48.1	0.0	0.0	
-30	245	2137.0	1729.5	54.2	3.9	3.5	60.2	0.0	0.0	
-30	295	397.1	388.2	65.5	5.6	5.5	65.5	0.0	0.0	
-10	15	183.0	422.1	154.5	45.9	55.5	81.0	29.6	10.8	24.4
-10	45	1731.3	2288.1	88.5	745.1	1334.9	120.0	15.8	7.5	31.8
-10	70	2713.3	2203.1	54.4	1257.9	1042.8	55.5	0.4	0.7	132.9
-10	95	884.3	2015.6	152.7	667.8	724.6	72.7	0.0	0.0	
-10	145	4693.3	2242.2	32.0	667.9	563.3	56.5	0.1	0.4	189.5
-10	195	4588.3	1721.1	25.1	47.0	47.1	67.2	0.0	0.0	
-10	245	3187.6	1972.3	41.4	6.1	3.2	35.3	0.0	0.0	
-10	295	293.9	305.9	69.7	5.5	3.3	39.6	0.3	0.7	189.5
0	15	169.0	122.6	48.6	1580.9	978.5	41.5	227.0	22.8	6.7
0	45	4214.8	3585.0	57.0	5097.9	1319.5	17.3	158.9	28.1	11.9
0	70	6321.0	3467.8	36.7	4204.3	1373.8	21.9	5.4	3.1	38.2
0	95	3911.6	4322.7	74.0	2250.1	793.1	23.6	0.0	0.0	
0	145	5979.3	2221.3	24.9	649.9	479.5	49.4	0.0	0.0	
0	195	6510.3	2578.6	26.5	39.6	32.3	54.6	0.0	0.0	
0	245	3497.3	2418.1	46.3	5.6	4.1	48.4	0.0	0.0	
0	295	244.9	255.9	70.0	6.8	4.7	47.1	0.0	0.0	
10	15	1166.9	1471.9	84.5	227.0	469.2	138.5	58.9	27.8	31.7
10	45	4113.0	3270.4	53.3	3816.0	1264.2	22.2	36.9	14.1	25.7
10	70	6850.9	4946.5	48.4	5080.4	1460.6	19.3	0.3	0.7	189.5
10	95	7445.8	4718.3	42.4	3602.8	1142.0	21.2	0.0	0.0	
10	145	7164.4	4205.4	39.3	648.9	384.9	39.7	0.0	0.0	
10	195	7071.8	2493.3	23.6	39.4	29.1	49.5	0.0	0.0	
10	245	3242.0	2476.7	51.2	5.9	4.4	50.4	0.0	0.0	
10	295	183.1	162.5	59.5	4.1	5.5	90.0	0.0	0.0	
30	-5	21.1	3.0	9.5	8.0	4.1	34.4	0.0	0.0	
30	95	6991.3	3190.9	30.6	227.9	188.4	55.4	0.0	0.0	
30	145	4317.4	3579.1	55.5	325.6	342.2	70.4	0.0	0.0	
30	195	5282.3	3917.3	49.7	16.3	9.9	40.8	0.0	0.0	
30	245	2068.8	2643.2	85.6	5.3	4.6	59.0	0.0	0.0	
30	295	99.1	147.4	99.6	3.8	4.9	86.9	0.0	0.0	
70	-25	41.0	23.6	38.6	12.9	10.8	56.1	0.1	0.4	189.5
70	45	454.5	1200.3	176.9	6.9	2.7	26.8	0.1	0.4	189.5
70	145	743.6	1505.5	135.6	5.9	4.8	54.3	0.0	0.0	
70	245	77.0	103.1	89.7	3.8	5.0	89.9	0.0	0.0	
120	295	40.6	33.1	54.6	6.4	5.9	61.5	0.0	0.0	

Chapter 4

Bubbly Flow around a Cylinder

Multiphase flows are encountered in many engineering applications, such as in heat exchangers [103], vortex flow meters [104], surface aerated stirring vessels [105], and froth flotation [106]. In each of these applications, both the structural integrity and performance of the device is dependent on the interactions between the component and the surrounding multiphase flow. However, the behaviour of the multiphase flow is challenging to predict *a priori* due to two-way coupled behaviour. When the dispersed phase is lighter than the carrier phase, numerous flow modifications are possible, including the addition of energy at a variety of scales present in the turbulent flow [21]. Nevertheless, the two-way coupling of the two flow phases is of significant importance for predicting heat transfer and flow mixing [21], which necessitates a thorough understanding of this complex flow. In an effort to simplify the flow condition, I study the canonical flow-structure interaction problem of cross-flow over a cylinder. By focusing on this canonical flow, I can draw upon a wealth of past research in the single phase case.

For single phase flow past a cylinder over a wide range of Reynolds numbers we see the famed von Karman vortex street, and from Re $\approx 10^2$ to 10^5 we even have a nearly constant Strouhal number. The definition of Strouhal number is as follows:

$$St = \frac{fD}{U} \tag{4.1}$$

Where f is the frequency of vortex shedding, D is the cylinder diameter, and U is the freestream velocity. To characterize the Strouhal number variation with Reynolds number, many fundamental studies exist (e.g. [107, 108, 109]. As Reynolds number increases above $O(10^5)$, the Strouhal number no longer remains constant, and cylinder roughness also takes on a more significant role (as shown by Lienhard [107] and Achenbach and Heinecke [108]). Despite this observed effect, and while single phase flow past cylinders is still of interest, it can be considered to be well understood [110, 111, 112, 113]. However, multiphase flow over a cylinder is much less understood. To understand the state of the knowledge in the multiphase case, I present a literature review on bubbly flow over a cylinder.

4.1   Literature Review on Bubbly Flow over a Cylinder

In part due to the clear design & structural implications of multiphase coupling, there has been a significant body of research on periodic shedding in two-phase cross flow. In particular, due to the relevance of two-phase shedding in heat exchanger applications, there has been a significant body of research on flow over tube bundles [114]. For brevity, I will not review this work here. Instead, I will focus solely on vortex shedding from cross-flow over a single cylinder.

Early experimental work by Hulin et al [115] and Hara [116] showed that the shedding frequency and vibration amplitude are affected when air is introduced to the flow. Hulin et al [115] found that there is an increase in both the mean frequency and bandwidth of pressure oscillations on the cylinder. Furthermore, they discovered that at high phase fractions ($\approx 10\%$) vortex shedding from the cylinder becomes less regular. Furthermore, Hulin et al [115] demonstrate that bubbles are trapped within vortices, for which the local phase fraction within the vortex increases with Reynolds number.

In addition to these results from Hulin et al [115] and Hara [116], a summary of the early work in two-phase cross flow over a cylinder is summarized in Ch. 27 of the Encyclopedia of Fluid Mechanics [117]. As a result of these initial experiments several important conclusions were reached, namely the following:

1. At phase fractions above 10%, a gas pocket builds behind the obstacle and the vortex emission in air-water flows becomes less stable.

2. At low void fractions (below 10%), the Strouhal number increases with phase fraction.

3. Bubbles are trapped in the cores of the vortices that are shed from the cylinder. The efficiency of this trapping increases with flow velocity.

These conclusions were reached empirically, and to develop an increased understanding a theoretical explanation based on modelling the wake behind an obstacle as an oscillating wing was developed. To do so, the lift force is proportional to the angle of attack, θ, as given by the following [117]:

$$F_{lift} = -K\rho_{mainflow}V_0^2\theta \tag{4.2}$$

Where K is a constant. If we assume that the effective wavelength is proportional to the width then we can rewrite the force as $F_{lift} = K'\rho_{wake}d^2\frac{d^2\theta}{dt^2}$ such that we obtain a differential equation for θ. Solving this differential equation, the frequency of vortex emission is proportional to the following [117]:

$$f \propto \frac{V_0}{D}\sqrt{\frac{\rho_{mainflow}}{\rho_{wake}}} \tag{4.3}$$

Since bubbles are trapped within the vortices, the wake density is lower than the density in the incoming flow. As a result, using this approach we can see that the frequency should be

higher when encountering multiphase flow instead of a single phase ($\rho_{mainflow} = \rho_{wake}$) case. However, this explanation does not explain the spatially and temporally varying phenomena of bubble trapping within downstream vortices. More work is needed to understand the fundamental physics driving this phenomena.

To address this knowledge gap, numerous experimental studies studied the effect of different parameters on flow patterns around the cylinder. A summary of the studied parameter range across this range of experimental studies is given in Table 4.1. In most of these works, the flow is forced and as such the Reynolds number is given by the freestream velocity. However, Uchiyama et al. [118] and Lee and Park [119] study the motion of bubble driven flows, and as such the Reynolds number is defined using the superficial gas velocity, $u_g = \frac{Q_g}{A}$.

Hara [120] demonstrated that air bubbles can reduce the Karman vortex-induced vibration in both the in-line and cross-flow directions. It is stated that "the reasons for this effect are not quantitatively clear, and we do not yet know all of the parameters influencing this vibration reduction effect." [120] With regards to cross-flow, Hara [120] found that small bubbles are more effective than large bubbles in reducing vibration. It was proposed that the stochastic motion of air bubbles in the flow was a factor in producing an unsteady lift force- effectively reducing cross-flow vibration.

A robust study on the effect of different cylinder diameters and Reynolds numbers was given by Yokosawa et al [121] and Inoue et al [122]. Joo et al [123] studied the effect of phase fraction on the drag coefficient. The effect of blockage ratio across a range of Reynolds numbers and phase fractions was studied by Shakouchi et al [124]. The effect of cylinder shape was qualitatively studied by Murai et al [125] and Habeeb et al [126]. In addition to presenting qualitative experimental data on the local phase fraction modification due to the obstacle, Habeeb et al [126] numerically computed both the local volume phase fractions and pressure on the cylinder. Voutsinas et al [127] studied the effect of bubble size on pressure fluctuations on the cylinder surface, as well as the local velocity distribution.

Voutsinas et al [127] demonstrate that changing the bubble size affects both the shedding frequency and amplitude. For the three studied bubble sizes (albeit not well characterized and also far from truly monodisperse [128]) in their work, there are bi-modal frequency peaks at both d = 2.6 mm and d = 0.27 mm. This is an indication that the shedding frequency depends strongly on the bubble size, and that the governing phenomena describing this relationship is much more complicated than given by Eq. 4.1. This is not a surprising result, since it makes sense that smaller bubbles will be entrained in the vortices shed from the cylinder at different rates.

The distribution of bubbles rising solely from buoyancy around a circular cylinder was studied by Uchiyama et al [118], for which it was found that in addition to bubbles entrained in the large scale eddies behind the cylinder, bubbles were also trapped in the stagnation point at the front of the cylinder. Lee and Park [119] study the gravity induced liquid motion of an oblate ellipsoid bubble swarm past a circular cylinder. A vortex street is not formed, but Lee and Park [119] note that an elongated region of low void fraction in the wake of the cylinder is reduced in size at increasing void fraction. At higher void fractions, shear induced lift is sufficiently large to cause earlier bubble migration to the cylinder wake. These topics

are further discussed in the thesis of Lee [129]. Kim and Rau [130] study the liquid only region in the wake of the cylinder, and note that this region decreases in size with increasing Reynolds number. Suzuki et al [131] show that microbubbles tend to accumulate in the front stagnation point, then are repulsed from the boundary layer near 90° from the front stagnation point. The presence of microbubbles alters the boundary layer dynamics and reduces the turbulence intensity ('laminarizing' the flow). Suzuki et al [131] reported that the shedding frequency increased with the introduction of microbubbles. Their hypothesis for the increase in the shedding frequency is the expansion of the laminar boundary layer coupled with an earlier separation point. Meng [132] note that coupling between bubbles and vortices can suppress the shedding frequency due to momentum coupling, but significant attention is not given to this result. The location of high void fraction regions in the wake of the cylinder is shown to be a function of bubble size. When bubbles are larger than the cylinder it is shown that a stable gas cavity can form in the wake of the cylinder.

While the focus of this work is on void fractions in which the shedding frequency remains coherent, it is important to note that as void fraction is increased $\gg 20\%$ the forces are still of significant interest. Pascal-Ribot and Blanchet [133, 134] study the lift force on a single rigid cylinder under cross flow in the range of void fraction from 20% - 80%. They note that as void fraction increases, the presence of low frequency components in the signal increases.

Within the reviewed experimental papers, several key effects are determined:

1. Bubbles tend to accumulate in vortices downstream.

2. There is a wake region with locally low void fraction in the wake of the cylinder which varies in size with obstacle shape and upstream void fraction.

3. The changes in shedding frequency and cylinder vibration experienced with multiphase flows are bubble size dependent.

4. Bubbles can alter the separation point.

While these effects are all of interest, none shed further light on the dominant mechanisms that lead to an alteration in the vortex shedding frequency. To shed additional light on some of the dominant mechanisms leading to these changes, selected numerical studies on bubbly flow over a cylinder are presented. A comprehensive review of numerical papers is not given as the accuracy and techniques used to account for two-way coupling are outside the scope of this work. Instead, these numerical works are used to fill in some of the knowledge gaps not provided by experimental works to date, specifically the proposed mechanisms by which the shedding frequency changes.

Table 4.1: Parameter range of previous experimental studies.

Paper	Phase Fraction [%]	Bubble Size [mm]	$Re_D = \frac{u_g D}{\nu}$	Cylinder Diameter [mm]	Cross-Section	Channel Size
Uchiyama et al. [118]	Not Reported	0.02 - 0.06	702, 981	30	Circular	440 mm x440 mm
Lee and Park [119]	0.3 - 2.1	3.7	Not Reported	20, 30	Circular	670 mm x240 mm
Paper	Phase Fraction [%]	Bubble Size [mm]	$Re_D = \frac{UD}{\nu}$	Cylinder Diameter [mm]	Cross-Section	Channel Size
Kim and Rau [130]	Not Reported	1-2,4-10	96 - 2868	9.5	Circular	136.5 mm x44.5 mm
Habeeb et al. [126]	22.2 - 66.7	Not Reported	14928 - 33439	30	Circular, Square, Triangular	30 mm x100 mm
Pascal-Ribot and Blanchet [134]	10 - 80	3 - 14.9	Not Reported	12.15,15.85,20.7 25.6,31.9	Circular	70 mm x100 mm
Suzuki et al [131]	0.03	0.09-0.43	46000	20	Circular	80 mm x2 mm
Voutsinas et al. [127]	0 - 5	0.25 - 2.6	5000, 10000	30	Square	90 mm x60 mm
Pascal-Ribot and Blanchet [133]	10 - 80	3 - 14.9	Not Reported	12.15	Circular	70 mm x100 mm
Murai et al. [125]	4 - 20	1.5 - 2.5	500 - 1800	10, 50	Circular, Square, Triangular, Ellipsoid (2), Star	10 mm x500 mm
Shakouchi et al. [124]	0 - 30	2.48	5000 - 15000	18, 22.5, 30, 45	Square	90 mm x45 mm
Iijima et al. [135]	0 - 33	3 - 4	12200 - 40000	30	Circular	200 mm x60 mm
Meng [132]	4 - 20	0.5 - 4	3000 - 45700	2,6,11	Circular	Circular D = 40 mm
Hara et al. [136]	0 - 20	5 - 6	2000 - 32500	25	Circular	200 mm x60 mm
Joo et al. [123]	0 - 50	Not Reported	430 - 21900	22	Circular	125 mm x200 mm
Yokosawa et al. [121]	0 - 10	3 - 5	4000-300000	1, 3, 5, 6, 8, 10, 20, 30, 40	Circular	80 mm x120 mm
Inoue et al. [122]	0 - 24	3 - 5	5000 - 80000	10, 20, 30, 40	Circular	120 mm x60 mm
Hara [116]	0 - 28.5	Not Reported	9000 - 18000	30	Circular	200 mm x60 mm
Hulin et al. [115]	0 - 25	2 - 4	0 - 110000	35 upstream, 23 downstream	Trapezoidal	150 mm diam. tube.

Review of Selected Numerical Studies on Bubbly Flow over a Cylinder

Many papers discussing available numerical techniques for the study of gas/liquid flows exist (e.g. [137]). Since the focus of this work is primarily experimental, a comprehensive review is not given. Instead, the goal is to fill in some of the knowledge gaps surrounding the mechanisms for why bubbles tend to shift the shedding frequency of flow over a cylinder through the review of select numerical works.

A review of numerical techniques for predicting bubble motion in vertical flows, as well as descriptions of the terms described in section 1.1 as applied to bubbly flows is given by Jakobsen et al [138]. These techniques include the application of commercial codes such as Fluent (e.g. Habeeb et al [126]) or finite volume CFD codes dedicated to multiphase flows [139]. Habeeb et al [126] found that their model did not match the bubble size which they measured experimentally, as a result of the errors in the bubble boundary definition. Hanafizadeh et al [140] studied the drag and pressure coefficient for two-phase flow around a circular cylinder using an Euler-Euler approach. The simulations use two cylinders in the streamwise direction, in which a smaller cylinder trips the flow prior to the passing around the main central cylinder. Xu et al [141] simulated flow around a square cylinder using a multi-scale model in order to study the lift and drag coefficients, void fraction distribution, and vortex shedding frequency. This model was shown to accurately capture the local phase fraction in the wake of the cylinder, while also correctly predicting the shedding frequency from the cylinder. Additionally the model was compared to and shown to outperform the Standard k-ϵ and RNG k-ϵ models. Meng [132] numerically computed bubble trajectories in the vicinity of the cylinder using a one-way coupled Lagrangian approach; however, due to the strong heterogeneity of two phase flow around a cylinder the results are mainly qualitative. They noted that experimental trajectories are necessary for further validation.

With the above array of methods in mind, several papers have proposed mechanisms for why the shedding frequency changes. Uchiyama and Degawa [142] study the flow using a combined Eulerean (vortex-in-cell) Lagrangian (bubble motion) approach. They found that bubbles captured in the shed vortices have a local void fraction that is approximately three times higher than the upstream value (which is varied from 0 - 0.03). They propose that the increased shedding frequency is due to increased water velocity from the presence of bubbles in the flow. Nguyen et al [143] apply the same Eulerean (vortex-in-cell) Lagrangian methodology. They found that the flow was quasi stable upstream but unstable downstream; bubbles tended to coalesce in regions of high shear to either side of the cylinder, but then these plane shear layers interacted and combined in the wake. Cook and Harlow [144] perform numerical studies on the two way coupled motion of bubbles passing around a rectangular obstacle. They note that bubble concentration centers within the shed vortices move more rapidly then the vortices themselves due to buoyancy, thereby pulling the vortices away from the cylinder more rapidly then they would otherwise be shed. In addition to this important finding, they note that the presence of bubbles alters the effective width of the vortex sheet, thereby providing a mechanism for the shedding frequency to change. In addition to bubble

capture within the shed vortices, Cook and Harlow [144] note that a 'tongue' of locally high void fraction forms on the opposite side of the shed vortex. This secondary region of high bubble density forms from the leading edge shear, while the primary vortex accumulation is driven by the flow separation vorticity layer [144]. This paper presents a notable departure from previous works, through the inclusion of additional regions of high void fraction with differing bubble accumulation time-scales.

However, the increase in shedding frequency has not been found universally in numerical studies. Sugiyama et al [145] simulated laminar bubbly flow around a circular cylinder for Reynolds number varying from 100 to 2000. Sugiyama et al [145] note that there is a local peak in the local void fraction at a distance of one diameter downstream, and posit that this is due to the preferential accumulation of bubbles in the shed vortex at this location. For a bubble size of 1.5 mm, at a Reynolds number of 200, it is noted that that there is little bubble clustering, and as such the Strouhal number appears unchanged with void fraction. At a Reynolds number of 500, a local peak in the Strouhal number is achieved at a void fraction of 15%. Sugiyama et al [145] note that for bubble accumulation in the wake vortices, a sufficiently large bubble relaxation time (ie. sufficient bubble inertia) is required. Importantly, they noted that bubble accumulation in the vortices increased when accounting for buoyancy effects, as the bubble relaxation time increased. A numerical study on flow over rectangular cylinders of varying thickness–to–width ratios was conducted by Uchiyama [146] at Re = 20000 (based on the cross width of the cylinder). Interestingly, Uchiyama [146] found that the Strouhal number *decreases* monotically with increasing gas phase fraction from 0.025 to 0.075, regardless of the thickness–to–width ratio.

In summary, several numerical studies on bubbly flow over a cylinder have been identified. These studies present several potential mechanisms for the increase in shedding frequency: (1) increased water velocity due to momentum transport from rising bubbles, (2) alteration of the density of the shed vortices from bubble accumulation (increasing the rise velocity of the vortices), (3) changing the effective width of the obstacle through alterations to the streamlines around the cylinder. While no definitive mechanism has been identified, these explanations provide a marked improvement upon the explanation provided by Eq. 4.1 as the bubble size effect is accounted for. It has been noted by Sugiyama et al [145] and Uchiyama [146] that there are cases in which the shedding frequency does not increase with increasing phase fraction. Given this lack of consensus, more work is needed to identify what effect bubbles have on the shedding frequency. Prior to diving into this in detail, a final (brief) review is presented on select papers studying the motion of bubbles near vortices; in these papers the vorticity is not produced by flow over a cylinder.

Bubble Capture in Alternate Vortex Flows

While it is not possible to give an exhaustive review of bubble capture in vortices here, there are several effects which are important to note moving forward. Several papers are presented which study the capture of bubbles within isolated vortex rings, free shear flows, and jets.

Sridhar and Katz [147] study the capture of bubbles within isolated vortex rings. They found that only a few bubbles are required to distort the vortex; furthermore, the distortion is at a maximum for bubbles with an equilibrium position of 20% - 40% of the core radius. Jha et al [22] studied the capture of bubbles in an isolated vortex ring. They described the stages of bubble capture, for which it is shown that bubbles initially approach the vortex core in a spiralling manner, gradually stretch along the azimuthal direction, and then break up into smaller bubbles. At low Weber number, the bubble reaches an equilibrium at a finite distance from the vortex centre while at larger Weber number the bubble is pulled into the vortex centre. The bubble capture time decreases significantly with increasing Weber number.

Ruetsch and Meiburg [148] study bubble capture in free shear flows. They found that the capture of bubbles reduces vorticity and the pressure gradients near the vortex core. These changes alter the equilibrium positions of bubbles of a particular size within the vortex. Druzhinin and Elghobashi [149] perform direct numerical simulations of bubbles within a free shear layer. It is found that bubbles preferentially accumulate in sheets within the shear layer; the preference of bubbles also leads to neighbouring regions of high and low vorticity.

Milenkovic et al [150, 151] experimentally study two-way coupled bubbly jet flows, in which periodic excitation of the shear layer is used to create regular coherent structures. It is observed that stable bubble rings, at a finite distance from the vortex core, can be convected downstream with the vortex. Due to vortex growth and secondary instabilites, these rings of trapped bubbles disintegrate at some distance downstream.

From these papers there are several key bubble trapping phenomena of note. The first is that there is an equilibrium distance from the vortex core at which bubbles tend to accumulate which is dependent on bubble size; this equilibrium distance has an influence on the degree of vortex distortion imparted by the presence of bubbles. Secondly, very few bubbles are required to cause vortex distortion. In addition to vortex distortion, bubbles have been seen to modify both the vorticity and pressure fields of the carrier fluid; again, these changes are strong functions of bubble size. The size-dependent equilibrium position of bubbles within the flow field is an important concept to apply to bubbly flows around a cylinder.

4.2 Summary of Literature Review

Experimental and numerical works studying bubbly flow around a cylinder have been reviewed. It has been found that:

1. Bubbles tend to accumulate in vortices downstream.

2. There is a wake region with locally low void fraction in the wake of the cylinder which varies in size with obstacle shape and upstream void fraction.

3. The changes in shedding frequency and cylinder vibration experienced with multi-phase flows are bubble size dependent. The shedding frequency tends to increase with increasing void fraction.

4. Bubbles can alter the separation point.

   The reviewed experimental works have not yet provided an explanation of the dominant mechanisms that leads to an alteration in the vortex shedding frequency. Numerical studies have led to several theories for this change, including:

1. The presence of bubbles alters the fluid velocity, which leads to an increase in the Strouhal number.

2. Bubbles alter the effective width of the obstacle via changes to the wake streamlines.

3. Bubbles alter the density of the shed vortices, and the subsequent change in buoyancy alters the shedding frequency.

   While all these explanations are reasonable, they do not yet provide a complete theory for the mechanism by which the shedding frequency changes with bubble size and void fraction. One would expect that such a theory would incorporate the time and spatially-dependent nature of bubble motion within the wake. A brief review of selected papers in the area of generic bubble/vortex interaction has shown that there is an equilibrium distance from the vortex core at which bubbles tend to accumulate which is dependent on bubble size; this equilibrium distance has an influence on the degree of vortex distortion imparted by the presence of bubbles. Furthermore, very few bubbles are required for vortex distortion. It is reasonable to expect that significant modification to the vortex street is possible at low void fractions; secondly, it surprising that there would be a monotonic change in the shedding frequency with increasing void fraction when bubble/vortex interactions are so strongly dependent on bubble size. This bubble size dependence is the focus of the present work, as I believe that studying individual bubble motions (and tracking potential vortex distortion) can provide insight into a unifying theory for the frequency changes of vortex shedding in a bubbly flow. By taking a measured and careful approach to studying this complex flow I can provide insight into the nature of the changes that are observed. This chapter provides a background into the methods that were developed to study the flow field, which include both numerical and experimental analysis.

4.3   Numerical Approach

Numerical simulations were conducted within a time-varying flow field to determine regions in which bubbles will accumulate. The simulations were one-way coupled, so the focus is on determining the position of bubbles within the flow rather than predicting the changes to the carrier flow field. The implemented numerical scheme is an Eulerean-Lagrangian approach in

which the flow field is determined using in an Eulerean frame of reference with conventional CFD tools. Bubble trajectories are then computed by solving a simplified version of the force balance equation given in Eq. 1.4. The particular coefficients used for each of the terms directly follow the work of Oweis et al [13] who applied a point-particle tracking model for the study of bubbles near a Lamb-Oseen vortex. This approach is valid under the assumption of one-way coupling (the bubbles are small relative to the length scale of the vortices), unchanging bubble radius (expected to be valid provided that we don't model the bubble motion within the vortex core), spherical bubbles (valid at low Weber number) and dilute bubble concentrations (so there are no bubble-bubble interactions). The fundamental equation of motion is a simplified version of the force balance given in Eq. 1.4:

$$m_p \frac{dV_i}{dt} = -(m_p - m_f)g + F_{\text{undisturbed fluid}} + F_{\text{added mass}} + F_{\text{drag}} + F_{\text{Saffman lift}} \qquad (4.4)$$

Note that the Basset history force has been neglected under the assumption that fluid accelerations are small, and Magnus lift has also been neglected. The terms for buoyancy, added mass, drag, and the force due to the undisturbed flow directly follow from Eq. 1.4 (provided that the carrier fluid is incompressible). The added mass coefficient is taken to be 0.5, while the drag coefficient is given by:

$$C_D = \frac{24}{Re_B}(1 + 0.197Re_B^{0.63} + (2.6 \text{ x } 10^4)Re_B^{1.38}) \qquad (4.5)$$

The bubble Reynolds number, Re_B, is defined as $Re_B = \frac{(u-v)D}{\nu}$ where u is the velocity of the undisturbed fluid at the centre of the bubble and v is the velocity of the bubble. The Saffman lift force has the slightly altered form of:

$$F_L = \frac{1}{8}C_L\rho\pi D^2|u - v|(u - v) \qquad (4.6)$$

Where the lift coefficient follows from Auton [152]:

$$C_L = \frac{2}{3}\frac{|\omega|D}{|u - v|} \qquad (4.7)$$

Where ω is the vorticity of the undisturbed fluid evaluated at the centre of the bubble. Given this governing equation, it is possible to propagate the motion of the bubble using the numerically computed Euler flow field. The fourth order Runge-Kutta method was used to compute the trajectory in time.

The purpose of the numerical study of bubble transport is to assess how bubbles of different sizes move within the flow field. While the change in shedding frequency with bubble injection is inherently a two-way coupled problem, it is difficult to know *a priori* the regions in which bubbles of different sizes will accumulate. While the equilibrium position of bubbles within isolated vortices and free shear flows has been studied (see section 4.1)

previously, the motion of bubbles in the vicinity of a cylinder is a strong function of the time history of bubble motion, beginning upstream of the cylinder. It is not sufficient to know how bubbles interact with the vortices in isolation; the location of bubbles relative to the shed vortices is a function of complex upstream interactions. Therefore, it is important to gain insight regarding the size-dependent bubble motion specifically in the flow around a shedding cylinder. Results of the numerical simulations are given in section 5.1. Before detailing these results, the experimental procedure is described.

4.4 Experimental Facility

The experimental facility consists of a vertical flow loop, for which a schematic is given in Fig. 4.1. The primary components are the vertically orientated flow conditioner and test section, after which flow passes through a settling tank before returning to the pump. The flow loop is described in detail in section 4.4. The center of the cylinder is located 4.5D downstream of the flow contraction, while the bubble injector needle is located 3.5D upstream of the center of the cylinder. The cylinder design is described in detail in section 4.5. The bubble injection is described in section 4.5.

The flow loop is heavily instrumented, to monitor the motion of both the dispersed and carrier phases. The sensors are described in detail in subsequent sections, but are briefly given here. The synchronization of all measurement sensors is described in detail in section 4.5.

- **Stereo 2D-3C Particle Image Velocimetry (PIV)**. Two cameras are used to determine the three components of the flow velocity in a 2D plane, which is illuminated by a dual pulse Nd-YAG 532 nm laser. The PIV measurements are described in detail in section 4.5.

- **Tomographic 3D Bubble Tracking in Near Wake**. Three additional cameras beyond the PIV pair are used to triangulate and track the bubble position in three dimensions. The bubble tracking procedure is described in detail in section 4.5.

- **Upstream Optical Measurements of Bubble Size**. Located between the bubble injector and the cylinder, a designated camera is used to size the bubbles before they interact with the cylinder. This procedure is described in section 4.5.

- **Pressure Measurements on Cylinder Surface**. The cylinder is 25.4 cm in diameter, and contains four taps for the measurement of the surface pressure. A detailed description of the cylinder and pressure measurements is given in section 4.5.

- **Flow Rate**. The flow rate is measured using a Endress Hauser Promass 83F Coriolis mass flow meter with a reference accuracy of $\pm$ 0.1% of the reading.
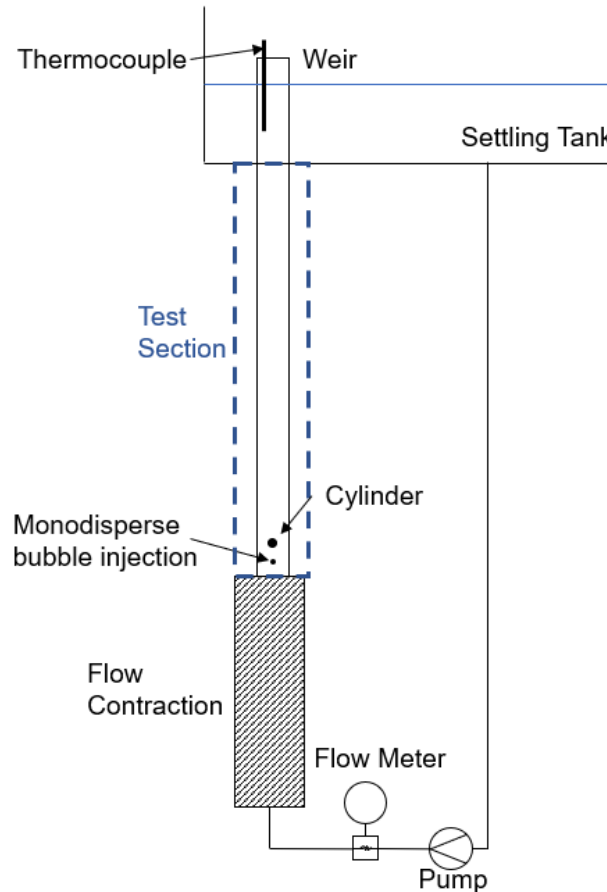
Figure 4.1: Vertical Flow Loop

- **Temperature Measurements**. The temperature of the water is measured at the top of the test section (Omega ON-970-44005 water thermistor). The air temperature is measured outside of the test section, with model number Omega OL-706 air thermistor.

Prior to describing the measurements in detail, the flow loop is described in detail.

Flow Loop

The pump used in the experiments is a Goulds 3656S series centrifugal pump with a nominal maximum flow rate of 160 GPM, resulting in a maximum superficial velocity of 1 m/s. The flow rate is controlled using a varible frequency drive (VFD). From the pump, the flow turns 90° vertically and enters a flow conditioner, which is described in detail in section 4.4. The purpose of the flow conditioner is to straighten the flow (direct streamlines vertically upward), ensure symmetry within the flow field, and ensure that "large scale" flow structures are eliminated. For the purpose of our experiments, the definition of large scale flow structures are those that are of comparable size to the vortices being shed by the cylinder, or

approximately one cylinder diameter in size. As described in section 4.4 we expect that the largest flow structures remaining in the flow are much smaller than the scale of the vortices being shed.

Following the exit of the flow conditioner, the flow enters the test section. The test section is 4 ft (1.22 m) long, and is 101.8 mm ± 0.2 mm x 101.9 mm ± 0.1 mm. The center of the cylinder is located 4.5D downstream of the flow conditioner. The cylinder passes through the wall of the test section, and the gap is sealed with a O-ring seated in the groove carved into the cylinder.

The location of the cylinder was chosen so as to ensure that the flow exiting the flow conditioner retained the desired top hat exit profile. To approximate the boundary layer thickness on the channel walls, we can use the Blasius solution for laminar flow over a flat plate:

$$\delta(x) = 5\sqrt{\frac{\nu x}{U_\infty}} \tag{4.8}$$

Where $\delta(x)$ is 99% of the boundary layer thickness at distance x from the start of the plate. At a distance of 4.5D (11.43 cm) and a freestream velocity of 0.33 m/s, the boundary layer is expected to be 2.9 mm, or 5.7% of the channel width. Note that this is a highly conservative estimate, as the experiments are often conducted at higher velocities. Consequently, the boundary layer development on the width of the channel is considered to be negligible. The remainder of the test section was in place for wake visualization, and to ensure that the effect of the flow passing into the settling tank was contained to the region far past the cylinder. Bubbles were injected 3.5D upstream of the center of the cylinder.

At the top of the test section, the flow passes through an expansion joint. The function of the expansion joint is to ensure that the test section remains vertical despite being connecting to the settling tank. Within the expansion joint, there is an insert that is the same width as the test section; the purpose of this insert is to prevent a sudden expansion in the flow.

Following the expansion joint the flow enters a settling tank, which is 0.61 m x 1.22 m x 0.46 m. The flow passes over top of a weir, which ensures that the pressure within the test section is constant. The settling tank is in place to allow bubbles to exit the flow loop, prior to the water returning back to the pump. During the experiments, visual inspection of the downward flow revealed that bubbles on the same order as the ones being injected were exiting the flow as intended. Visual inspection indicated that micro-bubbles may still be present in the flow at the highest flow rate, but this was a compromise that was necessary to constrain the size of the settling tank. From the settling tank the flow passed through the pump and back to the test section and flow conditioner.

Design of Flow Conditioner

The purpose of the flow conditioner is to ensure that the streamlines entering the test section are straight, and that the flow is devoid of structures on the same order as the vortices being shed.

(a) 6 x 7.3 cm holes.　　　(b) 163 x 1.02 cm holes.　　　(c) 431 x 0.51 cm holes.
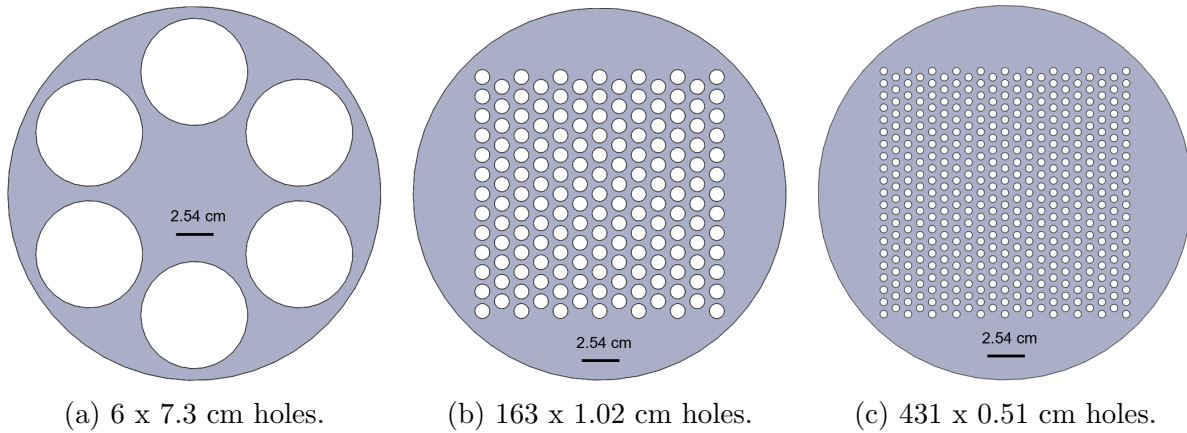
Figure 4.2: Pressure drop plates present in flow conditioner.

The flow conditioner is placed in between the flow meter and the test section, as seen in Fig. 4.1.

The main components of the flow conditioner are:

1. Six pressure drop plates, which are used to breakup the inlet jet and disperse flow through the full width of the flow conditioner.

2. 2 x 5.08 cm sections of 0.64 cm (0.25 in.) diameter honeycomb, which is used to straighten the flow streamlines and prevent flow structures larger than 0.64 cm from passing into the test section.

3. 1:1.7 flow contraction with a 101.6 cm (4 in.) square outlet, which directly precedes the test section. The flow contraction profile follows the 5th order polynomial given in [153].

The initial jet of water enters the flow conditioner via a 5.08 cm (2 in.) diameter inlet, and impacts two offset plates of the form given in Fig. 4.2a. Following these two plates, the cross section of the flow conditioner changes from a 25.4 cm (10 in.) diameter circle to a 17.1 cm (6.75 in.) square. The flow then passes through two sets of 163 x 1.02 cm (0.4 in.) hole plates and two sets of 0.51 cm (0.2 in.) hole plates. These plates are shown in Fig. 4.2b and Fig. 4.2c respectively. The function of the pressure drop plates is to disperse the flow evenly through the flow conditioner and break up any remaining lateral bulk motion prior to the honeycomb flow straightener. The gap between holes in the pressure drop plates was set by a 1/8 in. minimum requirement of the manufacturing process.

To determine the honeycomb size and location, Xiong et al [154] found that the breakdown of jets following a tube bundle or orifice plate at a Reynolds number of 100000 was roughly 4 pipe diameters downstream; at this distance, distinct flow structures created by the flow conditioner are no longer apparent. Based on the cell size in the honeycomb and orifice plate, this recovery distance is approximately 30 diameters downstream. Loehrke and Nagib

[155] recommend a honeycomb cell size to length ratio greater than 10, and show that the freestream turbulence intensity, $\frac{u_{rms}}{U_{\text{inf}}}$, decays to less than 5% within approximately 35 cell diameters downstream. However, they note that turbulence decay can be accelerated with a screen placed downstream of the honeycomb. In the current contraction design, a screen of 5.5 mm cell diameter as placed upstream and downstream of the honeycomb; the function of this screen was primarily to hold the honeycomb in place, rather than alter the turbulence dissipation downstream.

While size limitations in the flow contraction prevented the flow contraction from being placed 30-40 cell sizes downstream of the honeycomb, the beginning of the flow contraction was placed 16 cell sizes downstream. Notably, the flow contraction ended 64 cell sizes downstream, implying that the influence of the honeycomb cell size is negligible on the flow entering test section. The honeycomb was constructed of 2 x 5.08 cm segments. Each honeycomb cell was 0.64 cm (0.25 in.) in diameter, and the combined set of two honeycomb segments had a diameter to length ratio of 1:16. The flow contraction has a 1:1.7 contraction ratio, and reduces from a 17.15 cm (6.75 in.) square cross section to a 10.16 cm (4 in.) square at the entrance to the test section. The flow contraction profile follows the 5th order polynomial given in [153], with smoothing is applied in the corner of the contraction.

Using this flow conditioner, we observed a top hat velocity profile upstream of the cylinder, for which the profile at a location of x = -2D is given in Fig. 4.3. The boundary layer thickness on the walls is seen to be 3.5 mm $\pm$ 1.2 mm, where the uncertainty is the sum of the uncertainties for the location of the wall and the location of the boundary layer edge (each of which is given by one half of the interrogation window width). This measurement is only slightly larger than the 2.2 mm boundary layer prediction given by the Blasius solution at the same location. The upstream upstream turbulence intensity, defined with the freestream vertical velocity ($I = \frac{u_{rms}}{U_{\infty}}$), is 0.023.

4.5   Measurement Techniques

Using the experimental facility described above, the measurement techniques and devices used to analyze the flow are described.

Synchronizing Measurements

There are numerous measurements that must be made simultaneously, for which it is critical that the measurements are synchronized. The measurements can be broadly separated into three classes:

1. PIV measurements, which are controlled using an internal circuit timing board.

2. Tomographic bubble tracking images, for which the images and strobe are controlled using a BNC Model 575 delay generator.
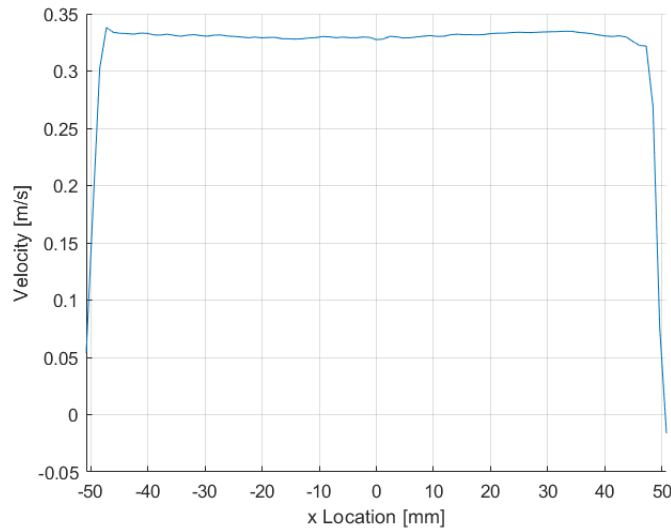
Figure 4.3: Upstream velocity profile at a mean velocity of 0.32 m/s at a location of x/D = -2 upstream. The centerline dip is due to the upstream influence of the cylinder.

3. Pressure and temperature measurements, which are controlled via a LabView program.

To ensure that the measuements are aligned, the DAQ measures the pressure and temperature data along with TTL trigger signals for both the PIV images and tomographic bubble images. The PIV TTL pulses are provided by an internal circuit board; the PIV trigger pulse also provides the trigger to the delay generator. Once triggered, the delay generator produces TTL pulses at a set frequency (with 250 ps resolution). For a velocity of 0.32 m/s, a 504 Hz frequency was sufficient to perform tomographic bubble tracking; this frequency was selected as an integer multiple of the PIV repetition frequency while allowing for sufficiently small motion between frames.

Particle Image Velocimetry Measurements

The velocity field of the carrier fluid is measured using particle image velocimetry (PIV). The PIV measurements are made with two cameras positioned in stereoscopic configuration, to provide 2D-3C velocity measurements. The positioning of the cameras relative to the test section is shown in Fig. 4.4.

The setup uses two 12-bit CCD cameras with an 1600 x 1200 array of 7.4 μm pixels (LaVision Imager PRO-X). The laser sheet is generated by a dual pulse Nd-YAG 532 nm laser (Lumibird Big Sky ICE450), with a maximum repetition rate of 15 Hz, which we ran at 14 Hz. Camera 1 is equipped with a Micro-Nikkor 50 mm lens, while camera 2 is equipped with a AF Nikkor 50 mm lens.

While the exposure time of the first image in the pair is dictated by the delay between laser pulses, the exposure time of the second pulse is fixed by the manufacturer at 33 ms.
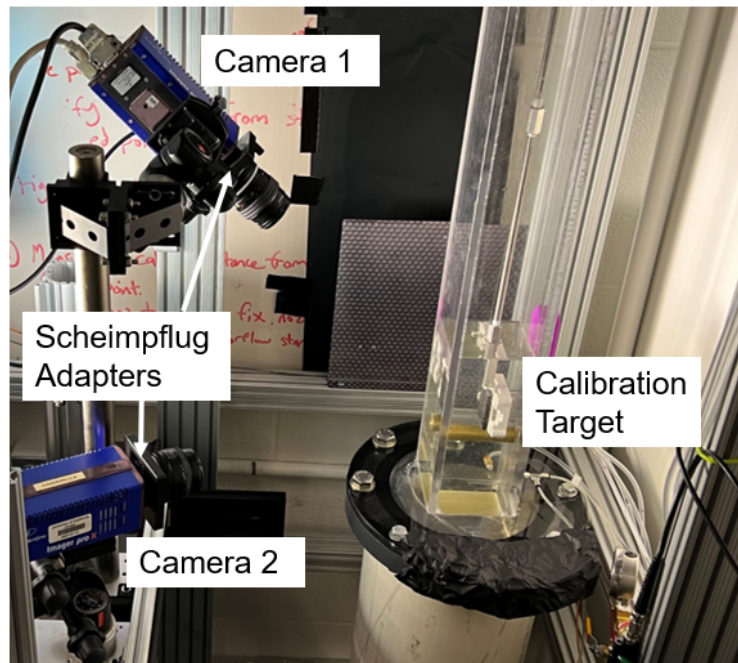
Figure 4.4: Position of PIV cameras relative to test section.

Since the strobe is pulsed to illuminate bubble trajectories during this exposure period (for more information see section 4.5, both cameras were equipped with filters to eliminate the blue strobe light. Camera 1 was at an oblique angle relative to the strobe, and consequently a yellow longpass (500 nm to 1100 nm) MidOpt filter was sufficient to prevent the strobe from altering the image quality. Camera 2 was equipped with a LaVision 3 nm bandpass filter (VZ20-0184), centred on 532 nm.

The calibration of the stereoscopic setup was performed with a LaVision Type #7 3D calibration card. The calibration card contains a 12x12 grid of 1.2 mm dots spaced 5 mm apart on the top surface, offset with an 11x11 grid that was recessed 1 mm into the plate. The shared calibrated area of both PIV cameras is 55 mm x 55 mm, located at the centerline of the test section.

To position the calibration card at the centerline of the test section, the card was placed within a 3D printed mount with four offset screws (seen in Fig. 4.5). When all four offset screws were placed against the back of the channel wall, the front of the calibration card was positioned within the centre of the channel. The mount was connected to a 3 degree of freedom (DOF) rotational mount and two linear stages at the top of the test section using 0.95 cm (3/8 in.) threaded rod, which allowed for precise positional control.

Once the calibration card was in place, calibration was conducted using Davis 7.2 from LaVision GmbH, which uses a 3rd order polynomial mapping function between identified points. Particularly due to optical distortion through the 1.27 cm thick (0.5 in.) test section wall no measurements were extrapolated outside of the calibrated area.

(a) Front view.   (b) Side view.
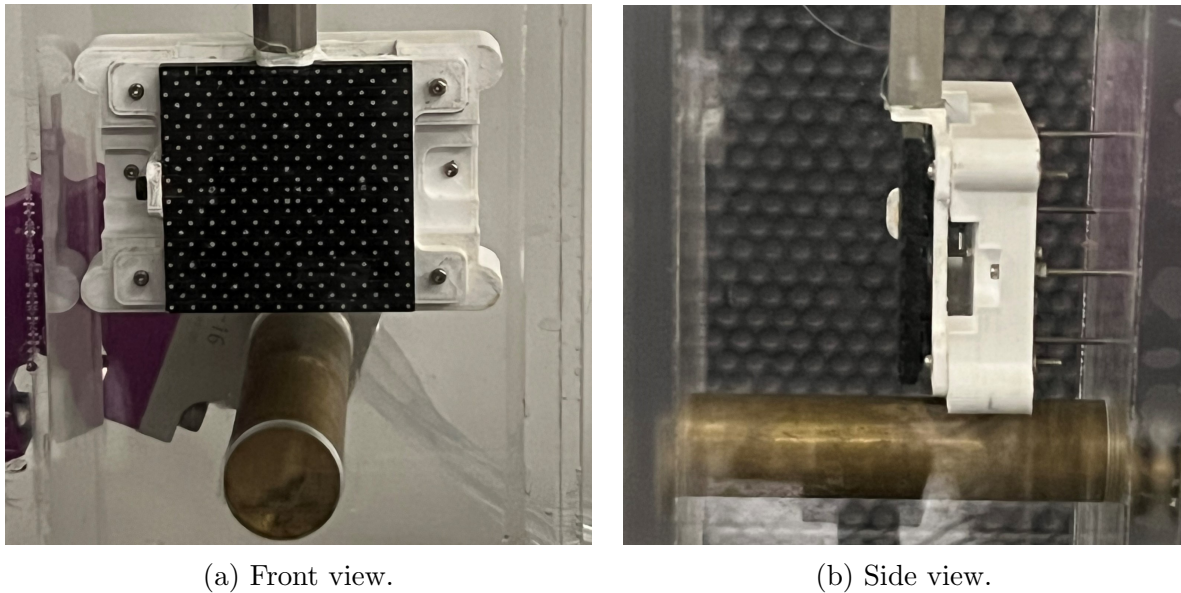
Figure 4.5: Positioning of 10 cm dual plane calibration card within test section.

The flow loop was seeded with Potters 110P8 sphericel hollow glass spheres. The particles have a density of 1.10 g/cm³, and a bulk density of 0.49 g/cm³. The mean particle size is 11.7 μm, and 50% of particles are smaller than 8.0 μm.

Since the bubble tracking and PIV data are obtained simultaneously, reflection off the bubble surface produces gaps in the PIV flow field. While these reflections could be minimized with fluorescent tracer particles, this could not be implemented within the current work. Consequently, median filtering is applied in PIV post-processing to fill in gaps in the generated vector flow field. This approach is assumed to be valid provided that the gaps are small relative to the length scale of the shed vortices in the wake (the dominant flow feature which we are aiming to resolve). Given that the injected bubbles are less than 1/30 of the diameter of the cylinder, this criteria is considered to be satisfied. However, it is understood that to determine finer flow features beyond the wake vortex structure, more careful treatment must be considered.

Cylinder Design and Pressure Measurements

The cylinder used in the experiments is 2.54 cm (1 in.) in diameter, and is made of brass. A simplified cylinder drawing is given in Fig. 4.6. The cylinder includes four pressure taps. Three pressure taps are positioned on the centerline of the channel, while the fourth is positioned 1/4 of the span across the channel (2.54 cm from the channel wall).

The cylinder is designed to pass through the test section wall and rest in a 0.64 cm (0.25 in.) slot in the back wall. The cylinder has an inset O-ring groove to prevent leakage from the test section. The O-ring also allows the cylinder to be rotated, such that the pressure

Figure 4.6: Critical dimensions and features of cylinder.

measurements can be made at any angle relative to the incoming flow.

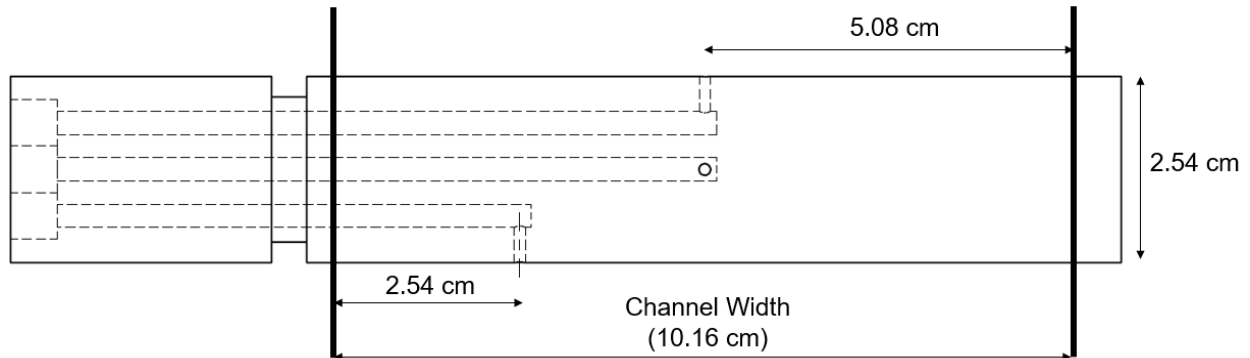The pressure taps pass to 0.32 cm (1/8 in.) inner diameter flexible tubing, which are connected to four differential pressure transducers. The differential pressure transducers have a range of -6.89 kPa to 6.89 kPa (-1 to 1 Psi), reference error of $\pm 0.08\%$, and a response time of less than 1 ms. The pressure transducers output a 4-20 mA signal which is simultaneously sampled at the rate specified by the delay generator. For more information on the synchronization of the measurements, see section 4.5.

By rotating the cylinder through the full 360°, the pressure distribution on the cylinder surface is determined. The off-centre pressure tap is used to determine the spanwise pressure variation. The pressure distribution on the cylinder surface at $Re_D = 18000$ is given in Fig. 4.7. The pressure coefficient off the centerline compares favourably with the centerline measurements, which indicates that the time-averaged pressure does not vary substantially across the span of the cylinder. Notably, the pressure coefficient is a strong function of the blockage ratio present in the channel. It has been reported at significant blockage ratios that the pressure coefficient is lower than in the infinite domain case (e.g. [156]), therefore, it is not surprising that the pressure coefficients seen in Fig 4.7 are lower than what is typically seen for comparable Reynolds numbers in a reduced blockage ratio channel.

Calibration of Tomographic Bubble Tracking

Bubbles are tracked in three dimensions using synchronized images from three cameras, for which the details are given in Table 4.2. The exact camera positions were determined through calibration, using the LaVision Type #7 3D calibration card pictured in Fig. 4.5. The calibration card was placed in the same x-y plane that was used for the stereo PIV calibration, ensuring that the z-planes are identical in both the bubble positioning and velocity measurements. The function of the calibration is to estimate the following parameters for each of the three cameras: camera rotation, position, focal length, pixel to mm conversion, camera centre offset, a radial distortion parameter (k_1), and two tangential distortion parameters ($p_{1,2}$). With knowledge of these parameters for each of the three cameras, the position of a
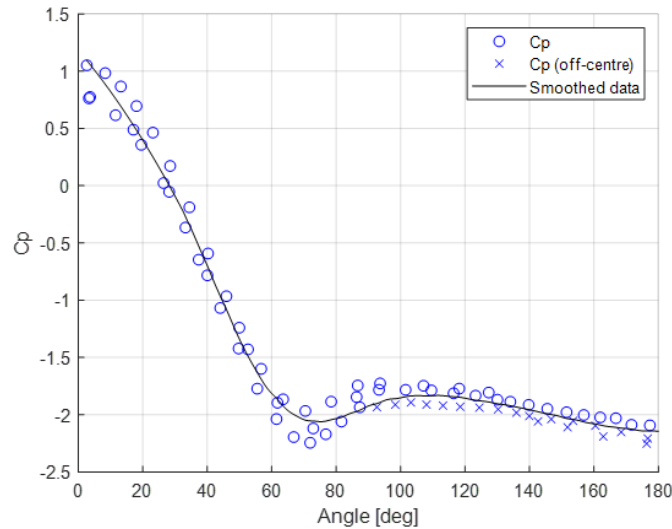
Figure 4.7: Experimentally measured C_p curve at $Re_D = 18000$. Angles are relative to front stagnation point.

point within the image can be converted to world coordinates. The calibration procedure is shown in Fig. 4.8.
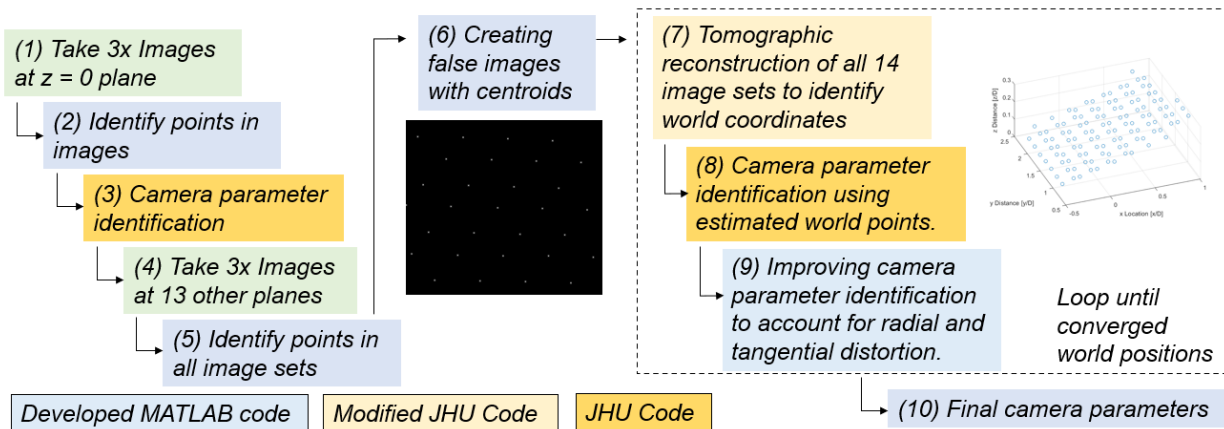
Figure 4.8: Process of estimating camera parameters for tomographic bubble tracking.

The calibration process begins with taking three simultaneous images of the calibration card in the same x-y plane as the stereo PIV calibration (z= 0). A set of example images of the calibration card are given in Fig. 4.9.

(a) Camera 1.   (b) Camera 2.   (c) Camera 3.
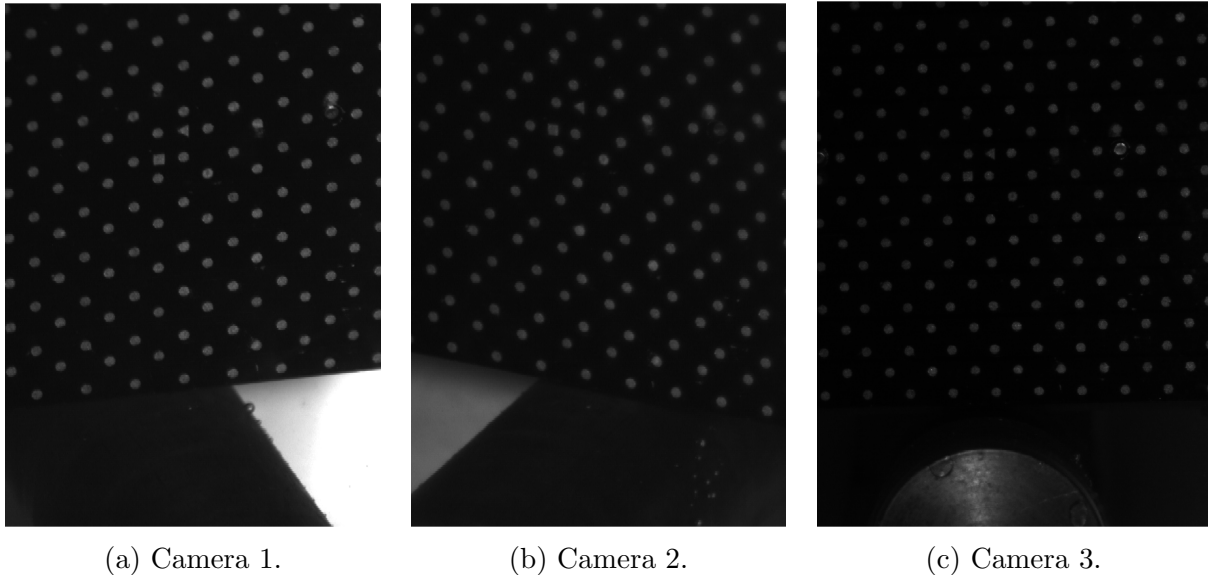
Figure 4.9: Sample calibration image set, with three simultaneous images of calibration card. Orientation in images is positive y upwards.

After identifying the dots on the calibration card, the camera parameters are estimated using this single set of images (step 3). The calibration card is then moved to 13 other positions (incorporating both tilt and translation in three dimensions), and the position of these calibration points are identified in the three sets of images (step 5). Since the triangulation code is not designed to handle the computation of centroids, the calibration card images are pre-processed and images containing only the dot centroids are created (3 images per camera position). The true position of these 13 additional positions in world coordinates *is not known*. These positions are instead used in a 'self-calibration' process, which is commonly used in conventional stereo or tomographic PIV. Rather than estimating camera parameters using true world coordinates, the procedure involves *estimating* the world position in the series of images, then optimizing the camera parameters to minimize error in the reconstructed position. For example, the world position of the points shown in Fig. 4.9 is given in Fig. 4.10.

The process is then repeated until the world positions converge. The process makes use of the facts that: (1) particles must be present in all three images; (2) shifts in camera position will cause correlated distortion between all particle positions; (3) the particles are in a known configuration so their relative position can be used to determine if the reconstruction is accurate.

The calibration procedure makes use of three primary codes:

1. MATLAB pre-processing code which identifies bubble centroids, then creates false images which include only particle centroids.
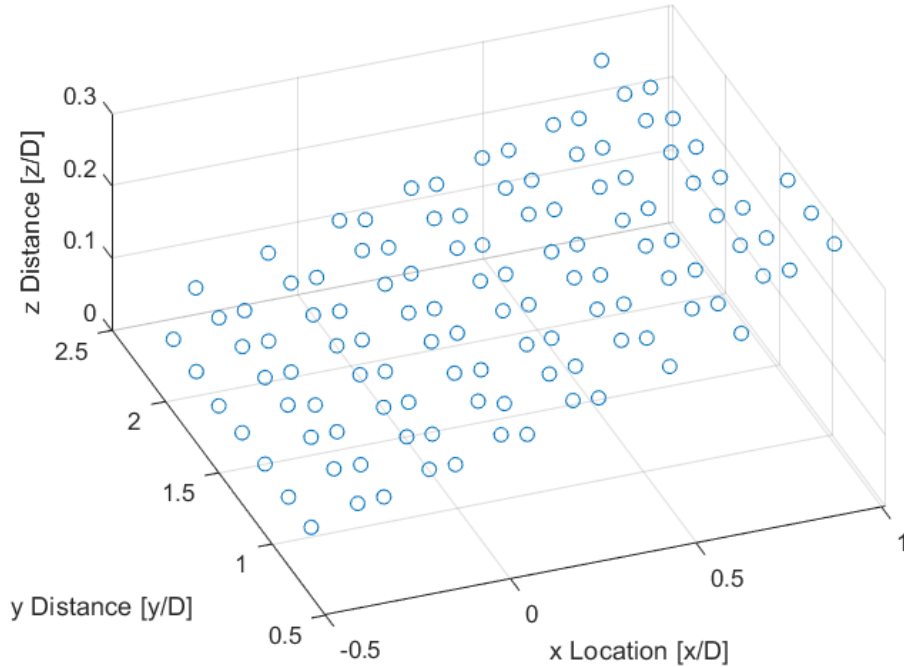
Figure 4.10: Estimated position of world points for calibration images shown in Fig. 4.9

2. MATLAB camera parameter identification code from Johns Hopkins university: *initial_calib.m*, while implements Tsai's method [157].

3. Modified C++ code from Johns Hopkins University for triangulation of bubble positions.

The original version of both codes from Johns Hopkins University can be found at `https://github.com/JHU-NI-LAB/OpenLPT_Shake-The-Box`, and is described in detail in Tan et al [158][159]. In addition to minor edits throughout the code, my main modification to the Johns Hopkins triangulation code is to include tangential distortion. The incorporation of camera distortion into the image analysis is described in the following section.

Accounting for Camera Distortion   Radial distortion is accounted for using the division model of Fitzgibbon [160], which has been suggested to have advantages over conventional radial distortion models [161]. The equations for radial distortion are given as follows:

$$x_{corr} = \frac{x_d}{1 + k_1(x_d^2 + y_d^2)} \tag{4.9}$$

$$y_{corr} = \frac{y_d}{1 + k_1(x_d^2 + y_d^2)} \tag{4.10}$$
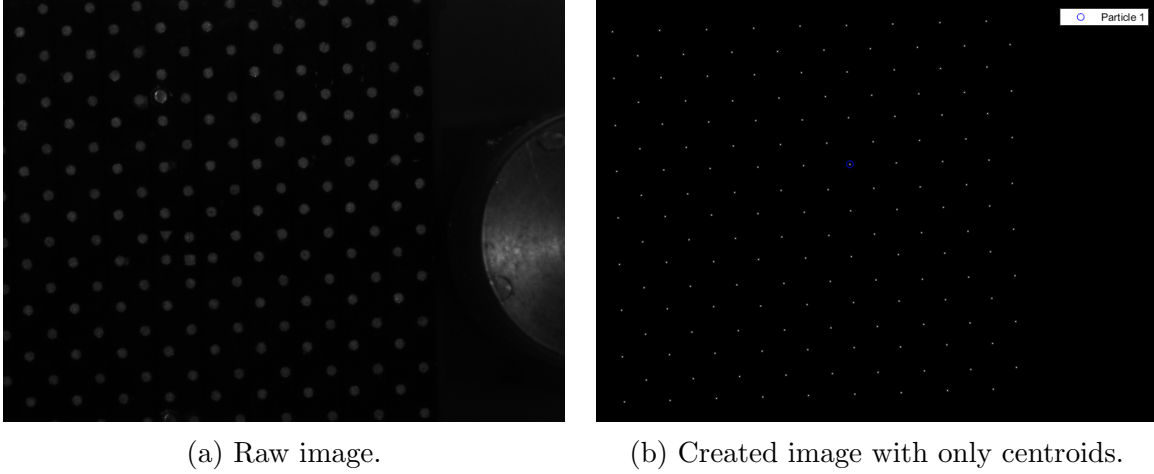
(a) Raw image.   (b) Created image with only centroids.

Figure 4.11: Comparison of raw image and identified centroids for view from camera 3, including particle that is to be triangulated ('particle 1').

Where $[x_d, y_d]$ is the distorted 2D position within the image, $[x_{corr}, y_{corr}]$ is the 2D position within the image following radial distortion corrections, and k_1 is the radial distortion coefficient that must be determined in the calibration process.

Tangential distortion is accounted for using equations given by Weng et al [162], such that the true undistorted position when accounting for radial and tangential distortion is given by the following

$$x = x_{corr} + p_1(3x_d^2 + y_d^2) + 2p_2 x_d y_d + O(x_d \cdot y_d)^4) \tag{4.11}$$
$$y = y_{corr} + 2p_1 x_d y_d + p_2(x_d^2 + 3y_d^2) + O(x_d \cdot y_d)^4) \tag{4.12}$$

Where $[x, y]$ is the fully undistorted 2D position within the image and $p_{1,2}$ are the tangential distortion coefficients that must be determined during calibration. Tangential distortion is particularly relevant in the present experiments, given the oblique angle of the cameras relative to the square test section. Both tangential distortion parameters, p_1, p_2 and the radial distortion parameter, k_1, is estimated with the calibration code. These parameters are also accounted for when projecting from 2D image coordinates to 3D world coordinates. With the above distortion model in mind, the working principle behind the code is described in the following section.

Triangulation Procedure. While the code is described in Tan et al [158] [159], a brief description of the working principle behind the code is given here. The triangulation code receives a camera parameter file, for which the process to generate the file is given in Fig. 4.8. At first, the code identifies particle positions (made trivially easy by pre-processing the images to only include particle centroids), and projects these images into world coordinates. The original calibration image and the image containing only centroids is given in Fig. 4.11.
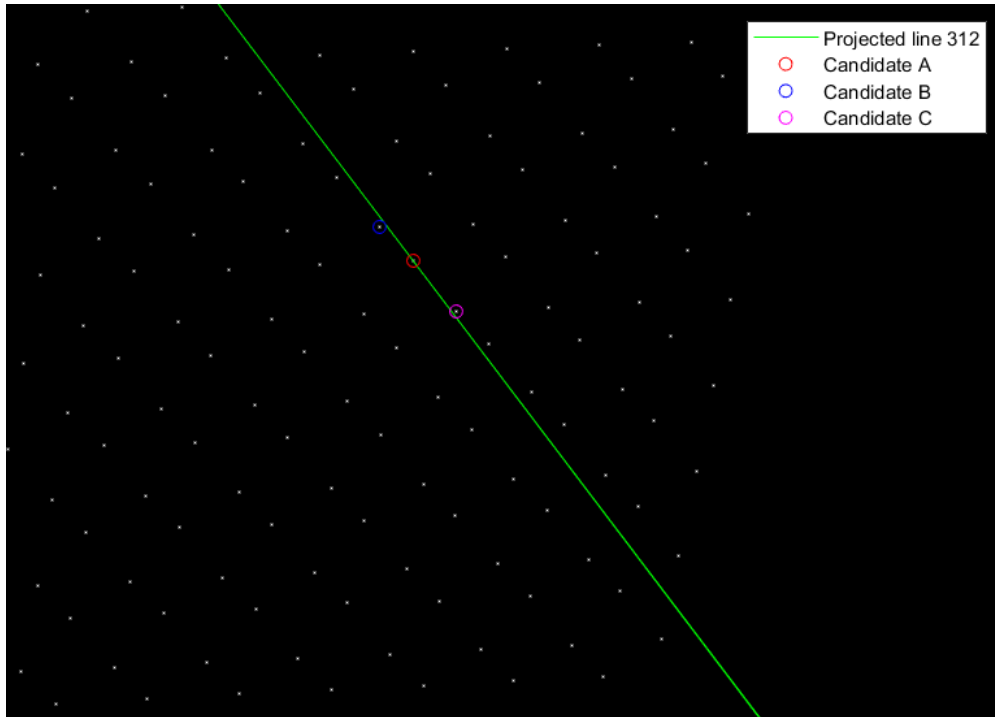
Figure 4.12: Line between particle 1 and the camera 3 projected onto view from camera 2. The three closest particles to the line are identified as potential matches.

For each identified point, a line between the camera centre and the 3D (world) position of the point is drawn. Along this line the camera cannot discern differences in position, so the other camera views must be used to determine the correct position in world coordinates. This line in 3D space is projected onto one of the other two camera planes, for which the projection is shown in Fig. 4.12. For clarity, I will refer to this line as '312', ie. the line drawn between camera 3 and particle 1 in world coordinates that is projected onto the image from camera 2.

According to a user-defined tolerance, particles within a certain distance of this line are identified as potential matches. In the sample image in Fig. 4.12, three potential matches have been identified. For each potential match, a line is drawn between camera 2 and the particle (in world coordinates), then is projected onto the image plane of camera 1. These lines are referred to as 2a1 (line between camera 2 and particle 'a' projected onto camera 1 plane), 2b1, and 2c1 respectively. We can also see the projected line 311 as well, which is from the original particle. Three intersection points have been identified, which correspond to potential matches between the particle from image 1 and the three candidate matches from image 2. The true particle position is the dot that minimizes the distance between an identified particle on image 1 and one of the three intersection points. If no dot is identified within the user defined tolerance, then a match is not created.

As can be seen from Fig. 4.13, the matched particle lies nearly exactly where it is expected

(a) Projection onto camera 1.   (b) Zoomed in view.
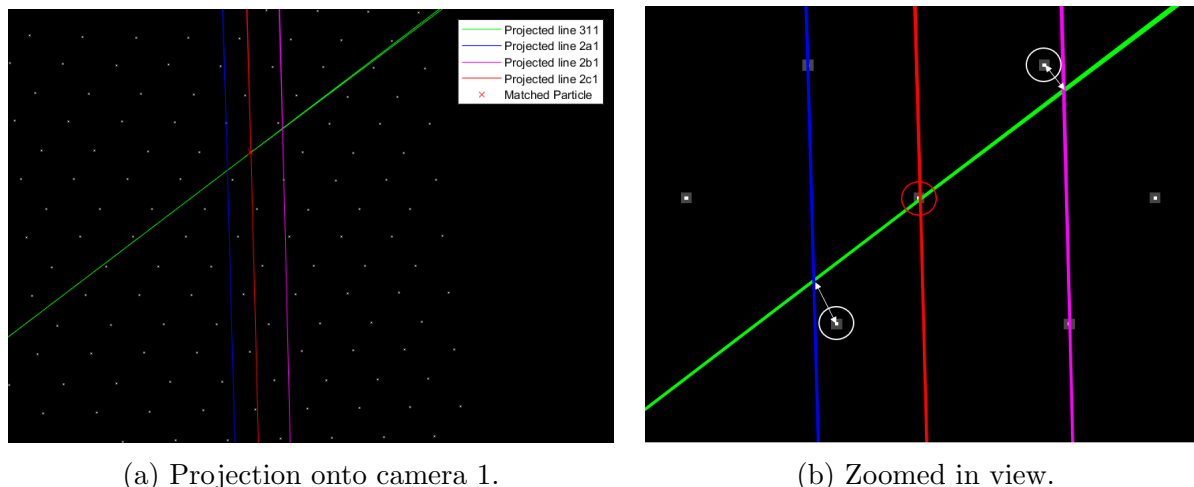
Figure 4.13: Projection of the three lines between potential matches and camera 2 onto the view from camera 1. The line between particle 1 and camera 3 is projected as well, and creates three intersection points with the potential matches. The three intersection points are compared to identified particles on image 1, with the true match being the identified particle which minimizes the distance to the intersection point.

on the camera 1 image. As a result, a particle has been matched between all three camera images. For each image, the particle is projected into world coordinates and a line is drawn between the respective camera and particle (ie. the line between camera 3 and particle 1, line between camera 2 and particle 2b, line between camera 1 and matched particle). The outputted world position from the triangulation code is the world position that minimizes the distance (in a least squares sense) between the three lines.

Notably, the Shake the Box and tracking modules of the code are not used, as the shake the box relies on particle tracking [158] [159]. The tracking of bubbles is notoriously hard as bubbles are not faithful flow tracers. Instead, the bubble trajectory depends on strongly on bubble size. Therefore, predictions of where the bubble should be in the next frame are not accurate enough to shift the triangulation based on the predicted position. Instead, false positives are removed based on heavy pre-processing, and relying on the relatively low bubble density per frame. Using this triangulation process, all fourteen calibration images were reconstructed in 3D.

Summary of Calibration.   The total volume calibrated using the fourteen planes is shown in Fig. 4.14. The position of these points overlaid on the $z = 0$ plane calibration images is given in Fig. 4.15. Note that the calibration card (particularly for camera 3) has some dots which do not show up as triangulated points. These dots are outside the shared image plane between all three cameras, and therefore do not show up in either camera 1 or 2. As such, these dots could not be triangulated.
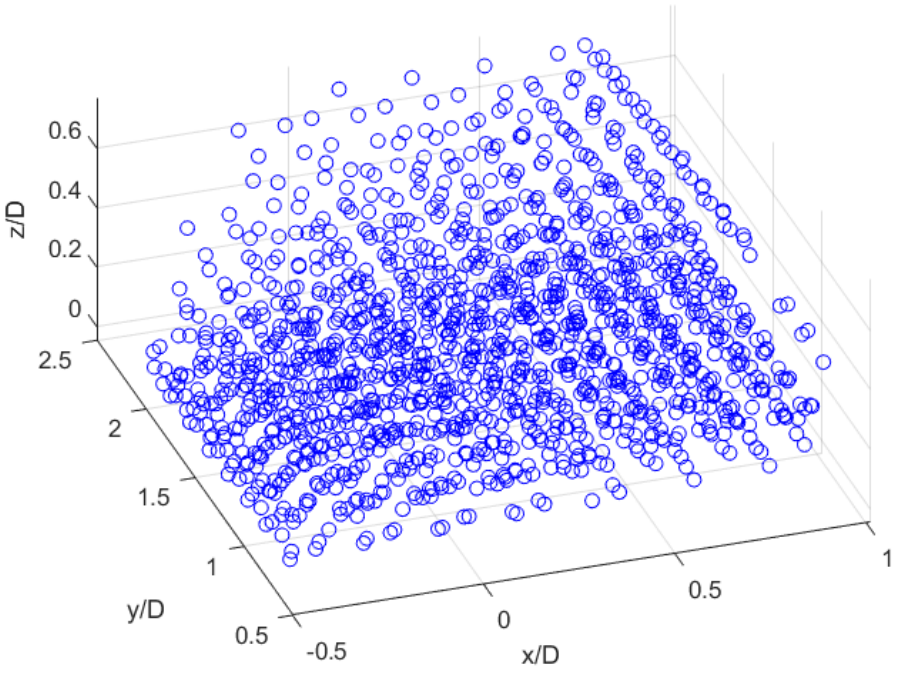
Figure 4.14: Position of all points from 14 calibration planes.

(a) Camera 1.   (b) Camera 2.   (c) Camera 3.
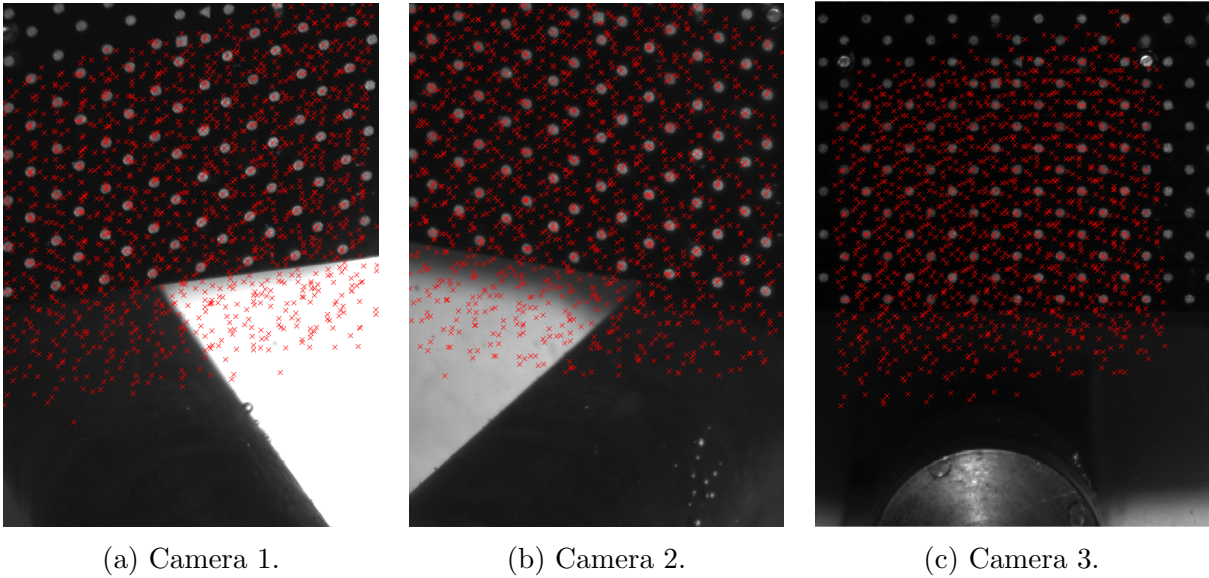
Figure 4.15: Position of all points from 14 calibration planes overlaid on z = 0 plane set of images.

Within the calibrated volume, there are 1414 points, which span the range x∈[-12.1, 21.7]
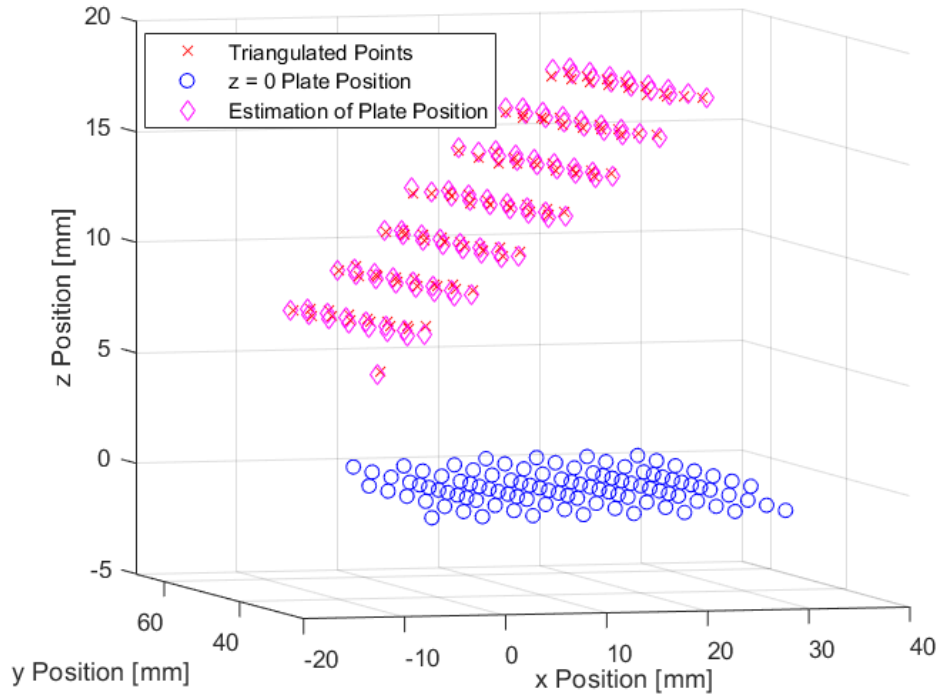
Figure 4.16: Rotation and translation of calibration plate points, to estimate error in world position reconstruction.

mm, y∈[17.8, 62.0] mm, z∈[-1.2, 19.6] mm. Since the exact position of the calibration plate within each image is not known in 13 of the 14 images, the true position of the plate must be estimated to compute the error. To do so, a rotation and translation is applied to the calibration plate coordinates, which minimizes the mean squared distance between the plate coordinates and triangulated point cluster. The optimized rotation and translation of the calibration plate does not change the relative position of the points. The triangulated point cluster and estimated plate position for one of the images is shown in Fig. 4.16.

Across all points in the volume, the median distance between the triangulated position and estimated position on the plate is 0.16 mm. Only 1 point had an error larger than 1 mm, and the 95.5% of points had an error below 0.5 mm. Since the error computation relies on a best fit approach to determine the plate position, this error calculation is sensitive to the relative positional error of points within a given image rather than the *true* position error. However, given the robust performance across many different calibration plate positions within the volume it is assumed that the true positions have also been computed accurately. At the end of the calibration process I produced the set of camera parameters given in Table 4.2, which are the camera rotation, position, focal length, pixel to mm conversion, a radial distortion parameter (k_1), and two tangential distortion parameters ($p_{1,2}$). Note that the pixel to mm conversion is determined separately for the x and y direction within the image.

Cam. #	Model	Lens	Image Size [pix]
1	JAI SP-5000M	Computar 12-36mm	768 x 550
2	JAI SP-5000M	AF Micro-Nikkor 60mm	768 x 550
3	Basler acA800-510um	AF Nikkor 28mm	800 x 600

Cam. #	Rotation Matrix	Focal Length [mm]	[x,y,z] Position [mm]
1	$\begin{bmatrix} -0.1266 & 0.9327 & 0.3376 \\ 0.9746 & -0.0251 & 0.2224 \\ 0.2159 & 0.3572 & -0.9059 \end{bmatrix}$	405	[-75 167 346]
2	$\begin{bmatrix} 0.1659 & 0.9524 & 0.2556 \\ 0.9426 & 0.0023 & -0.3339 \\ -0.3186 & 0.2963 & -0.8974 \end{bmatrix}$	543	[175 187 476]
3	$\begin{bmatrix} -0.0006 & 0.9999 & 0.0120 \\ 0.9999 & 0.0001 & -0.0163 \\ -0.0163 & 0.0120 & -0.9998 \end{bmatrix}$	335	[14 38 335]

Cam. #	Centre Offset [mm] [x y]	mm per Pix, x	mm per Pix, y
1	[-0.02 -0.02]	0.0742	0.0758
2	[0.01 -0.04]	0.0696	0.0695
3	[0.01 -0.04]	0.0760	0.0758

Cam. #	p_1	p_2	k_1
1	-2.8 x 10^{-5}	-1.1 x 10^{-5}	1.2 x 10^{-7}
2	3.6 x 10^{-5}	-5.7 x 10^{-6}	2.3 x 10^{-7}
3	3.8 x 10^{-7}	1.2 x 10^{-5}	-1.0 x 10^{-6}

Table 4.2: Specifications of tomographic bubble tracking cameras.

Using this set of camera parameters, tomographic bubble tracking could be undertaken.

Tomographic Bubble Tracking

Bubbles are tracked in three dimensions using synchronized images from three cameras, for which example images are given in Fig. 4.17.

(a) Camera 1.

(b) Camera 2.

(c) Camera 3.
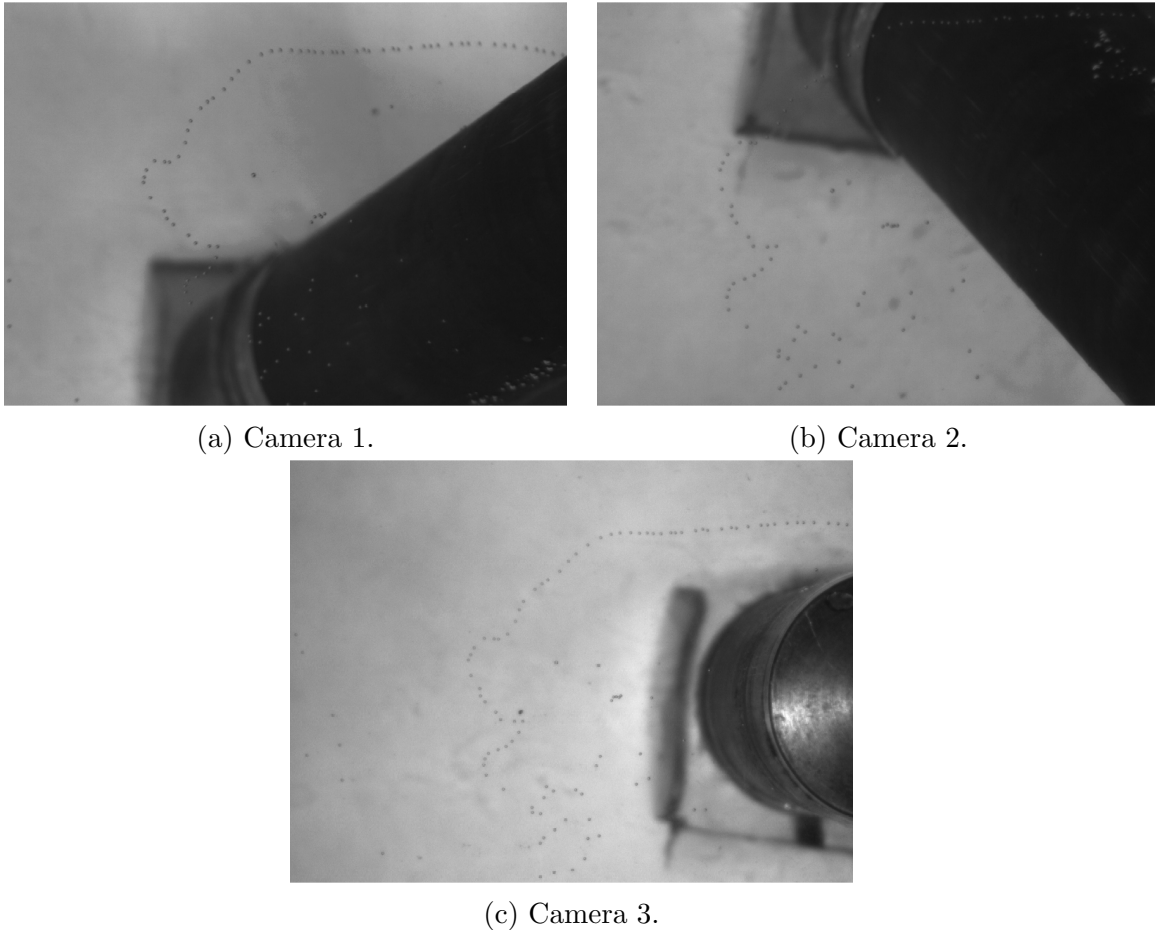
Figure 4.17: Raw images of bubble injection, used for tomographic bubble tracking.

From these raw images, MATLAB code which performed background subtraction, edge detection, and outlier rejection was used to identify the bubble centroids. The located centroids for the raw images given in Fig. 4.17 are given in Fig. 4.18.

(a) Camera 1.

(b) Camera 2.

(c) Camera 3.
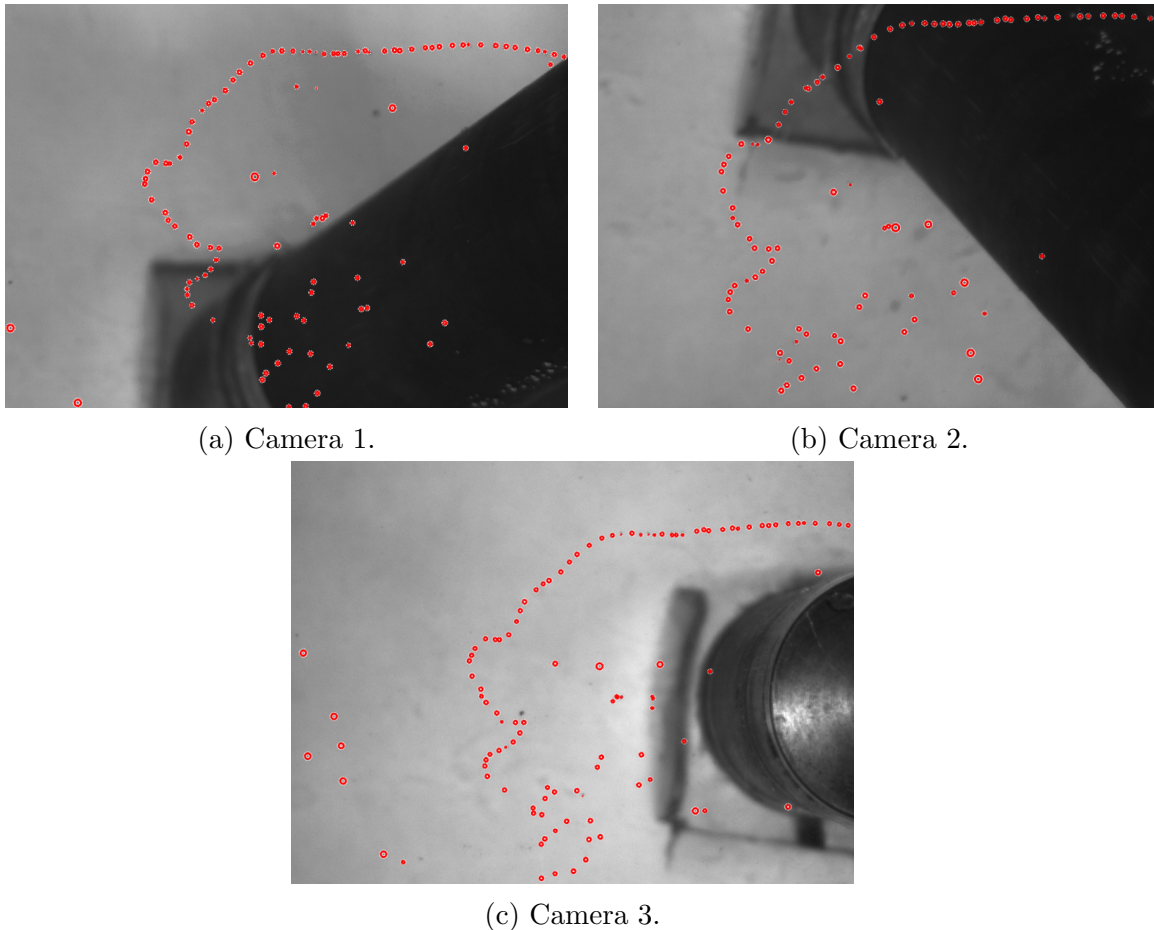
Figure 4.18: Identifying bubble centroids in images used for tomographic bubble tracking.

From the bubble centroids, false images of the form given in Fig. 4.11b were used as an input to the tomographic bubble tracking code. Note that despite the potential for false positives in the centroid images, the triangulation code performs additional checks to reject false matches. As described in section 4.5, the tomographic code is highly accurate at producing correct matches, even when the points are placed in close proximity. While a fourth (redundant) camera can provide direct validation and improve the accuracy of the tracking process, the triangulation process was deemed to be sufficiently accurate to proceed.

Bubble Injection

Monodisperse bubbles were produced using a single LAMYLEC L250 bubble injector, which was positioned 3.5D upstream of the cylinder. The injector is a commercial product from YLEC consultants. The injector operates in a coflowing arrangement, for which the pressure and flow rate of the water and air streams can be modified independently. The monodisperse bubble sizes produced with the injector are a function of the ratio of the two pressures and
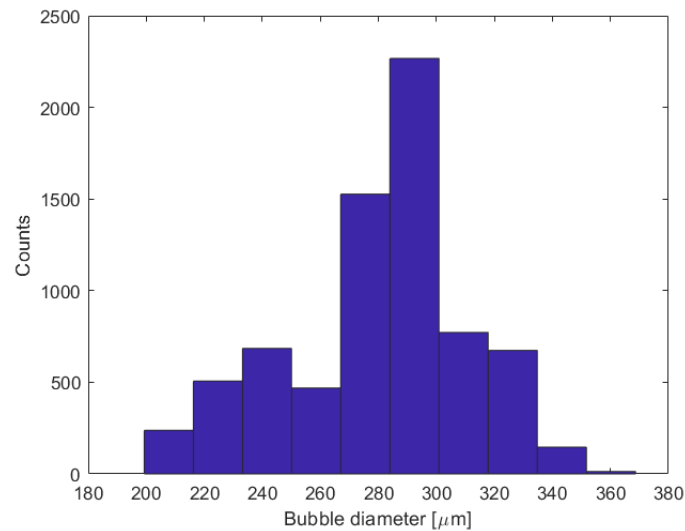
Figure 4.19: Sample histogram of bubble sizes with a mean diameter of 281 μm and a standard deviation of 31 μm.

flow rates. The sizing of bubbles produced using this injector is described in the subsequent section.

Upstream Bubble Sizing   Bubbles were sized using a camera which measured the bubble position upstream of the cylinder. The measurement of the diameter is approximated as $\pm$ 2 pixels, which corresponds to an uncertainty of $\pm$ 10 μm. An example histogram using this method is shown in Fig. 4.19. The variation in the bubble size is due to: (1) variation from the physical bubble size as well (2) artificial variation from uncertainty in the image detection method, which uses edge detection to automatically size bubbles from the images. Despite both of these factors, the variation in the bubble size is larger than the uncertainty of the camera, indicating that the true uncertainty in the bubble size is not limited by the camera resolution. The bubble sizes are highly monodisperse, which allows for the isolated study of the bubble size effect. Bubble sizes were measured for each test using a set of 1000 uncorrelated frames, to ensure that the distribution is accurate.

Chapter 5

Results for Bubble Transport around a Cylinder

To provide insight into the mechanism by which the shedding frequency changes in a bubbly flow, I looked to characterize dispersed bubble transport in the vicinity of a cylinder. Both simulations and experiments were conducted, which provide complementary sets of data. From the study of size dependent, nominally one-coupled, bubble motion, regions of locally high void fraction are determined. These regions are then related to observed changes in the structure of the shed vortices.

5.1   Numerical Study

Numerical simulations were conducted using the methods described in section 4.3. The Eulerian flow field was computed using large eddy simulation (LES). The LES code was an in house software developed by Per-Olof Persson, and has been applied to problems such as vertical axis wind turbines [163] and separated flows [164]. While flow past a cylinder inherently has spanwise variation, simulations were first conducted in 2D under the assumption of an infinitely long cylinder; this allowed results to be obtained at a much lower computational expense.

The code makes use of 3rd order mesh elements, for which the mesh is given in Fig. 5.1. The mesh contains 3957 cubic elements, with 16 node points per element. The time discretization was a 3rd order L-stable DIRK scheme with a 0.005 s time step. No slip conditions were applied on the cylinder surface, and periodic boundary conditions were applied on the domain boundaries. The simulated Reynolds number based on the cylinder diameter is $Re_D = 20000$.

The pressure distribution on the cylinder surface is given in Fig. 5.2, where the angle is in reference to the front stagnation point. The coefficient of pressure is given by $C_P = \frac{P - P_\infty}{\frac{1}{2}\rho U_\infty^2}$, where U_∞ and P_∞ are the far field velocity and pressure, respectively. When comparing Fig. 5.2 to literature (e.g. Moussaed et al [165]), it is seen that the 2D LES simulations
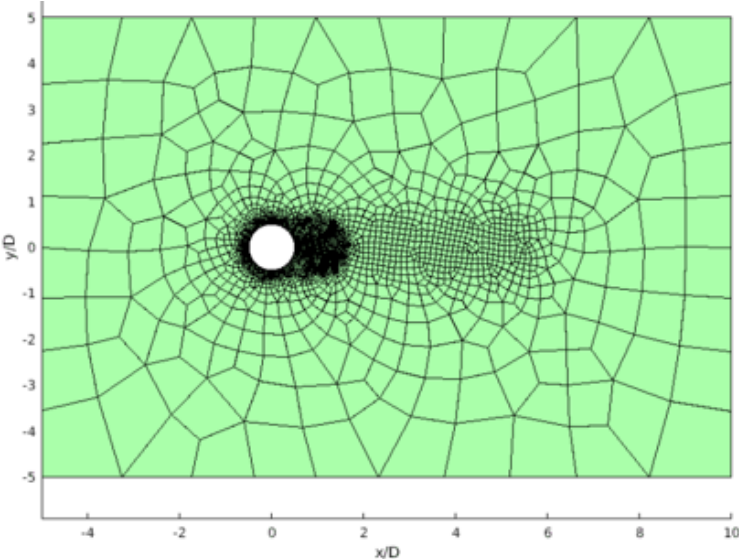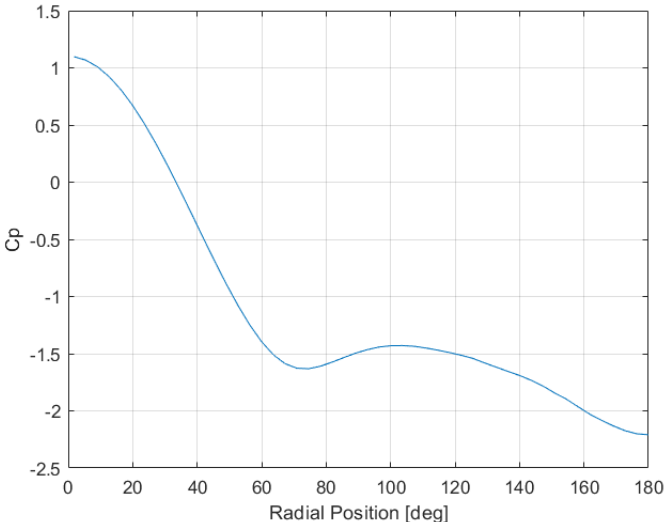
Figure 5.1: Mesh for 2D LES Simulations.

Figure 5.2: Pressure distribution on cylinder surface computed with 2D LES simulations at $Re_D = 20000$.

under-predict the pressure in the wake of the cylinder. Under-predicting the base pressure is a well known problem with 2D simulations (e.g. see Lei et al [166]). Despite this inaccuracy in the pressure coefficient, *qualitative* results are presented using the 2D simulation results. It is important to note that current work is being undertaken to study bubble motion with 3D LES simulations in a confined channel, as discussed further in section 6.1.

Numerical Simulation Results

With the Eulerian flow field computed as described in the preceding section, Lagrangian bubble trajectories are computed using Eq. 4.3. Given that the pressure in the wake of the cylinder is under-predicted with 2D LES, it is not possible to draw quantitative conclusions from the computed bubble trajectories. However, there are several important qualitative findings which are of note. The motion of two sets of bubble trajectories, corresponding to a bubble size of d = 200 μm and d = 1000 μm (with a cylinder diameter of 2 cm), is given in Fig. 5.3. The bubble trajectories are computed from a release point of x/D = -1 upstream, and varying y/D position from -1 to 1. This release point was selected as a balance between reducing computational expense (avoiding computing bubble trajectories far upstream of the cylinder) while allowing bubbles to reach an equilibrium position from cylinder interaction. It is important to note that bubbles preferentially sample particular regions of the flow in the vicinity of the cylinder, so evenly spaced bubble positions are only equally probable far upstream of the cylinder. The bubble trajectories were computed with the fourth order Runge-Kutta method with a fixed time step of 1 μs. Bubble trajectories were computed in a time varying flow field, for which linear temporal interpolation between solved flow fields (5 ms interval) was used at intermediate time steps.

There are several features of note in Fig. 5.3. The first is that there is a region upstream of the cylinder which is devoid of bubbles; this region increases in size with increasing bubble size. This region is caused by high pressure upstream of the cylinder. In the case of d = 1000 μm bubbles, bubbles are forced along a common streamline which could lead to a path of locally high bubble density. Notably, since the simulations are one-way coupled this does not lead to increased coalescence or bubble interaction but this effect may become important when accounting for two way coupling. Downstream of the cylinder, it can be seen that strong preferential accumulation of bubbles occurs. Bubbles are pulled towards the shed vortices, and form looping patterns as they are advected with the vortices downstream. Notably, these loops are of finite size (which is bubble size dependent) - indicating that bubbles do not simply cluster in the centre of the vortices. As described in section 4.1, this finite offset from the vortex centre could lead to increased vortex distortion.

To determine the spatially dependent interaction of bubbles with the shed vortices, statistics were computed across a series of simulations. The vortex centre was computed using the Q-criterion, which identifies regions in which the vorticity magnitude is greater than the strain rate. Bubbles were considered to be captured if they were within 0.2D (400 μm) of the vortex centre. It was necessary to choose a distance that was sufficiently large that the equilibrium distance from the vortex centre (of the studied bubble sizes) was contained

(a) d = 200 μm, 0.04 s

(b) d = 200 μm, 0.09 s.

(c) d = 1000 μm, 0.04 s.

(d) d = 1000 μm, 0.09 s.
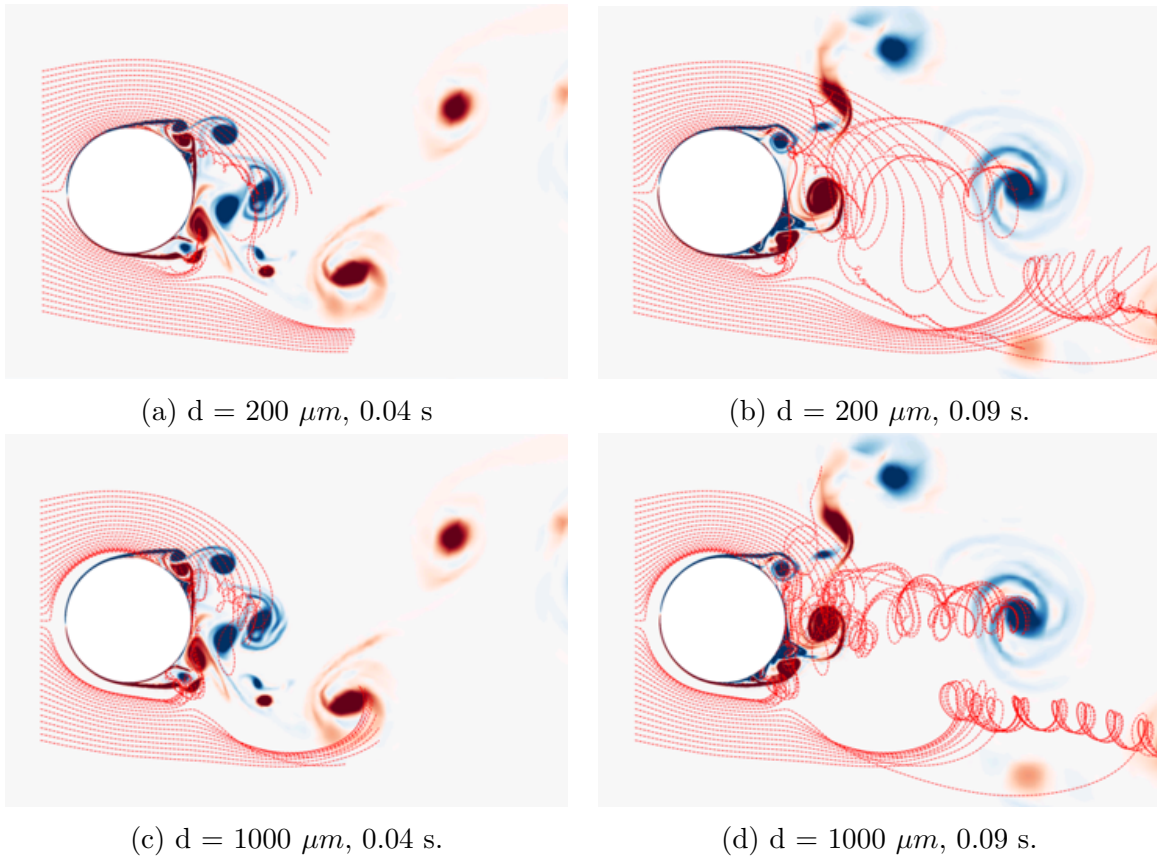
Figure 5.3: Effect of bubble size and time since upstream release on position within the flow field. Trajectories are overlaid on a snapshot of vorticity, but the trajectories were computed using a time-varying flow field. Flow is from left to right.

within this limit; however, the region had to be sufficiently small so that bubbles which entered this region tended to remain trapped. This criteria could be improved in future work, however, it is sufficient for the qualitative nature of the results currently being presented. Bubble trajectories were simulated across two shedding cycles, with bubbles released at 1/8 intervals across the shedding period. For each starting point, 200 bubbles were simulated along the line of x/D = -1, y/D = $[-1, 1]$. This is not sufficient data for converged statistics, but it is sufficient to draw some high level conclusions.

The probability of capture as a function of distance downstream is shown in Fig. 5.4; smoothing was applied to the curves to increase the clarity of the data. The convergence of these statistics could be improved by releasing bubbles at a greater number of points within each shedding cycle, or by averaging over more than two shedding cycles. However, a compromise is necessary given the computational cost of computing individual Lagrangian trajectories.

From Fig. 5.4, it is clear that the probability of vortex capture is a strong function of
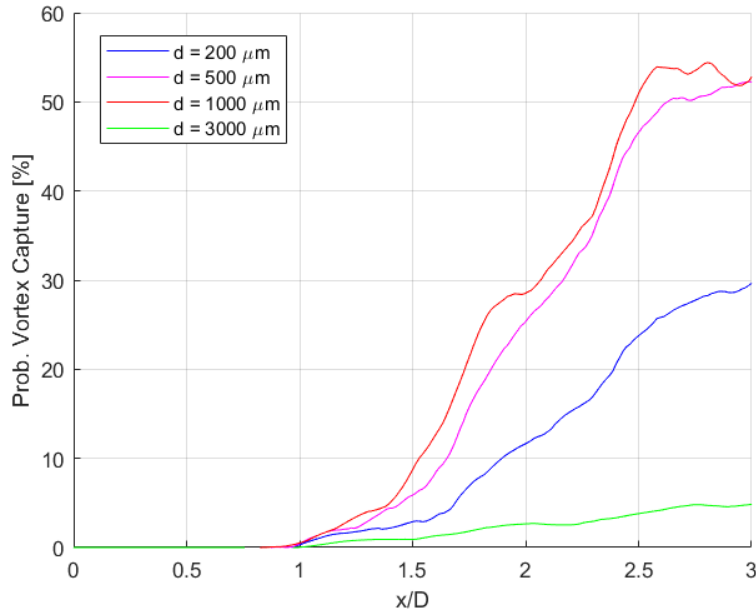
Figure 5.4: Probability of vortex capture as a function of distance downstream of cylinder.

bubble size and distance downstream. The capture probability increases for all bubble sizes with distance downstream. While this is not surprising, it is interesting to note that the highest probability of capture occurs at an intermediate bubble size. It would be challenging to predict these capture probabilities *a priori*, as the capture probability is a function of both the preferential accumulation of bubbles upstream of the cylinder (driven by pressure gradients from the leading edge of the cylinder) as well as time and spatially dependent position of bubbles relative to the shed vortices. Bubbles do not simply interact with the vortices in isolation - they preferentially sample certain regions within the flow, which then determines the location and probability of capture.

To understand how bubbles move when approaching a vortex, sample trajectories of four different bubbles approaching the exact same vortex are shown in Fig. 5.5. The trajectories are plotted in a moving reference frame with the vortex. All four bubbles were released at the same position upstream. The motion of the bubbles differs substantially both upstream of the vortex as well as near the vortex core. Both features are important to consider; as mentioned previously, the motion of bubbles upstream of the vortex is an important factor in determining the likelihood that bubbles are captured (as it determines the distance and inertia of the bubble as it approaches the vortex). When bubbles approach the vortex core it is clear to see that bubbles of sufficient inertia (such as d = 3000 μm) do not simply approach the vortex and remain trapped; instead, the bubble passes near the vortex then gets flung away. By comparison, the other bubble sizes were all trapped in the vortex upon approach, but the equilibrium distance relative to the vortex centre varied with bubble size.

While the results presented here are solely for $Re_D = 20000$, it is reasonable to think that
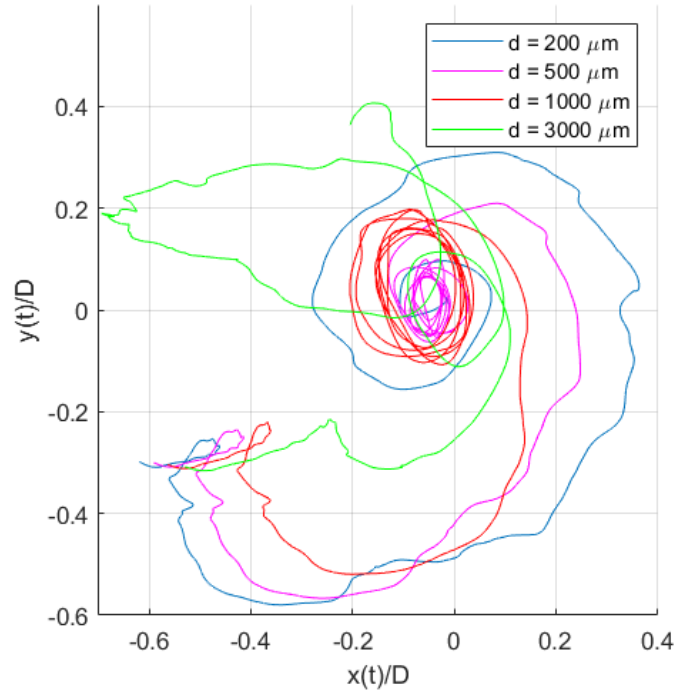
Figure 5.5: Size dependent bubble trajectories plotted in moving reference frame relative to vortex.

the optimally captured bubble size is Reynolds number dependent. Changing the Reynolds number changes the strength and position of the shed vortices. As a result, bubbles would preferentially sample different regions of the flow.

In summary, there are several important effects which were determined using numerical simulations:

1. There is a region which is largely devoid of bubbles upstream of the cylinder. This region leads to the formation of streamlines with higher bubble density.

2. The likelihood that bubbles are captured in the shed vortices is a strong function of bubble size. The highest probability of capture for $Re_D = 20000$ is an intermediate size within the d $= [200, 3000]$ μm studied range.

3. The orbital motion taken by bubbles as they approach the vortex is a strong function of bubble size. Once bubbles reach an equilibrium position within the vortex it is clear that there is a finite offset from the vortex centre. This effect mirrors that shown in previous works (reviewed in section 4.1).

Despite the qualitative nature of these results, it is clear that vortex interaction in the wake is bubble size dependent. As discussed in section 4.1, once bubbles interact with vortices

then we would expect vortex distortion to occur, as well as bubble coalescence (which could drive further distortion). In short, determining the probability of capture is a necessary step to understanding how the vortex structure changes when bubbles are injected into the flow; however, the nonlinear nature of bubble capture necessitates high fidelity numerical simulations and experiments to be computed. These initial findings will hopefully provide the groundwork for motivating why such careful study of bubble motion is required, even when attempting to understand changes to the bulk flow field. To further illustrate this point, results are now presented from the experimental study.

5.2 Experimental Study

To study the motion of individual bubbles experimentally, we use the experimental setup described in section 4.4. Results are presented for the case of $Re_D = 8100$, which corresponds to a velocity of 0.32 m/s. The upstream velocity profile at this Reynolds number is reported in Fig. 4.3. Four different bubble sizes were injected at this velocity: (1) 210 μm ± 46 μm, (2) 281 μm ± 31 μm, (3) 487 μm ± 78 μm, and (4) 673 μm ± 59 μm. For the mean bubble size of 487 μm, the size distribution was determined using wake data near the cylinder; unfortunately, upstream images did not exist for this case. An example size histogram for the size of 281 μm ± 31 μm is given in Fig. 4.19.

For all injected bubble sizes, the upstream void fraction is less than 0.0005%. Consequently, there was no change in the measured shedding frequency on the cylinder. The shedding frequency for the case of 487 μm bubble injection is shown in Fig. 5.6.

Notably, the frequency peak of 3.08 Hz corresponds to a Strouhal number of 0.24. This is higher than the Strouhal number of 0.2 that would be expected in an infinite domain, yet is reasonable given the 25% blockage ratio. As reported by Nguyen and Lei [156], for a Reynolds number of 8100 they predict that the Strouhal number should be ≈ 0.24. This compares well with the value we measure directly.

Several methods are used to analyze the bubble motion. The first is through qualitative assessment of images of the bubble motion, for which images are synched with velocity measurements to determine the position within the shedding cycle. In the subsequent set of images, warm colours are used to indicate counter-clockwise (CCW) rotating vortices, while cool colours are used to indicate clockwise (CW) vortices.

In Fig. 5.7, we can see the motion of 673 μm ± 59 μm bubbles within the cylinder wake. The line of bubbles on the right hand side of the cylinder is significantly distorted as bubbles are pulled into the wake via the CCW rotating vortex. Within this region, bubbles coalesce and are gradually carried downstream with the shed vortex. Of the four studied bubble sizes, this is the only case in which significant coalesence occurs. The increased likelihood of coalesence for this bubble size is notable as larger bubbles are more likely to distort and break up vortices. The effect of these bubbles on the vorticity is explored further below.

In Fig. 5.8, we can see the motion of 487 μm ± 78 μm bubbles within the cylinder wake. The line of bubbles on the right hand side of the cylinder experiences significant distortion as
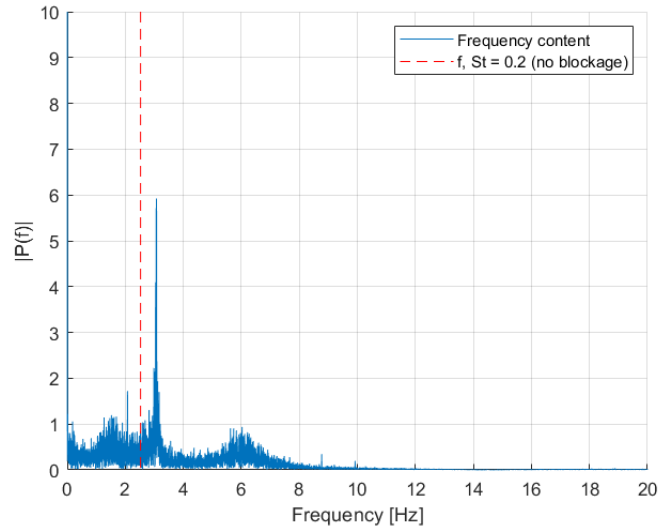
Figure 5.6: Frequency spectrum of pressure signal, measured at 270° degrees clockwise from front stagnation point. The frequency corresponding to a Strouhal number of 0.2 is shown for reference.

bubbles are pulled into the wake via the CCW rotating vortex. Within this region, bubbles are not grouped tightly enough to coalesce. Instead, bubbles become scattered throughout the wake region. Notably, significant distortion of the line of bubbles only occurs at the phase = 0 point in the cycle; in all other images the line of bubbles is still present (although it is shifted either further or closer to the cylinder if the CCW vortex is weaker or stronger, respectively).

In Fig. 5.9, we can see the motion of 281 $\mu m \pm 31 \mu m$ bubbles within the cylinder wake. The line of bubbles on the right hand side of the cylinder experiences distortion as bubbles are pulled into the wake via the CCW rotating vortex, but the line is still observable at all points in the shedding cycle. Bubbles are pulled out of the line and into the wake when they encounter the CW vortex on the left hand side of the cylinder; however, the line of bubbles only stretches this far at the phase = 0 point in the shedding cycle.

In Fig. 5.10, we can see the motion of 210 $\mu m \pm 46 \mu m$ bubbles within the cylinder wake. The line of bubbles on the right hand side of the cylinder is present at all points in the shedding cycle, and comparatively few bubbles are pulled into the wake region.

From these qualitative images showing the motion of bubbles in the cylinder wake, we can identify several key phenomena:

1. The degree of clustering in the wake increases with bubble size (at the studied Reynolds number of 8100). At the largest bubble size, there was sufficient clustering for coalescence to be readily observed.

2. The motion of bubbles in the wake is strongly dependent on both the time-dependent

(a) Phase = 0   (b) Phase = $\pi/2$

(c) Phase = π (d) Phase = $3\pi/2$

Figure 5.7: Snapshots of 673 μm ± 59 μm bubble motion during shedding cycle (indicated by range $[0, 2\pi]$) with overlaid centerline vorticity contours. Flow is from left to right.

position of vortices in the wake and the bubble size. The fluctuating position of the undistorted line of bubbles illustrates the time-scale of bubble re-positioning with changing vortex strength and position. For sufficiently small bubbles, the time-scale of distortion of this line is too large for bubbles to end up in the near wake.

These phenomena illustrate how bubbles of different sizes take different paths through the wake. If bubbles are sufficiently small, they don't cluster within vortices (in the studied range of 0 - 2D downstream). If bubbles are sufficiently large, then the bubbles cluster close enough in the shed vortices for coalescence to occur. The effect of these phenomena on vortex distortion will be discussed further, however, it is important to first improve upon the qualitative nature of this analysis.

In particular, these images show the position of bubbles near the centerline vortices, yet notably do not distinguish between bubbles that are near the centerline (and hence responding to the measured flow field) versus bubbles that are far from the centerline (and hence

(a) Phase $= 0$ (b) Phase $= \pi/2$

(c) Phase $= \pi$ (d) Phase $= 3\pi/2$

Figure 5.8: Snapshots of 487 μm $\pm$ 78 μm bubble motion during shedding cycle (indicated by range $[0, 2\pi]$) with overlaid centerline vorticity contours. Flow is from left to right.

responding to an unknown flow field). Therefore, tomographic bubble tracking is required to identify bubbles which are near the centerline. To illustrate the tracking capability of the system described in section 4.5, three bubble tracks are given in Fig. 5.11. Notably, the bubbles are positioned in sequence at the start of the track, yet deviate significantly in the spanwise (z) direction as they move throughout the wake. As a result of this spanwise motion, the bubbles experience different flow fields and are carried to significantly different [x,y] positions. These tracks are demonstrative of the capability of tomographic bubble tracking for eliminating bubbles that are sufficiently far from the measured velocity profile, as well as producing validation trajectories for bubble motion models (e.g. such as those described in section 4.3).

From Fig. 5.11, it is clear that the motion of individual bubbles varies significantly, even when bubbles are of the same size and are initially in close proximity. To quantitatively study bubble motion within the flow field, many phase averaged bubble positions must be

(a) Phase = 0   (b) Phase = $\pi/2$
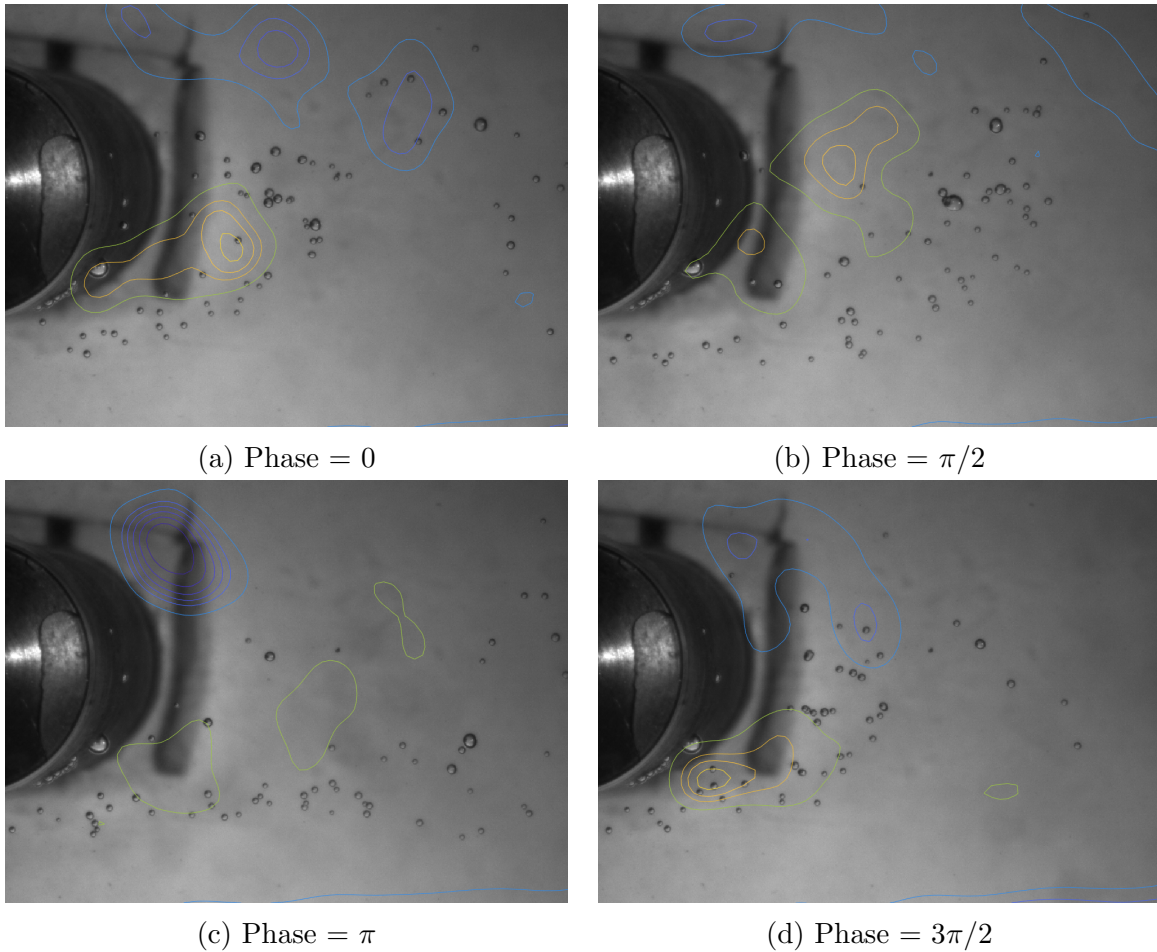
(c) Phase = π (d) Phase = $3\pi/2$
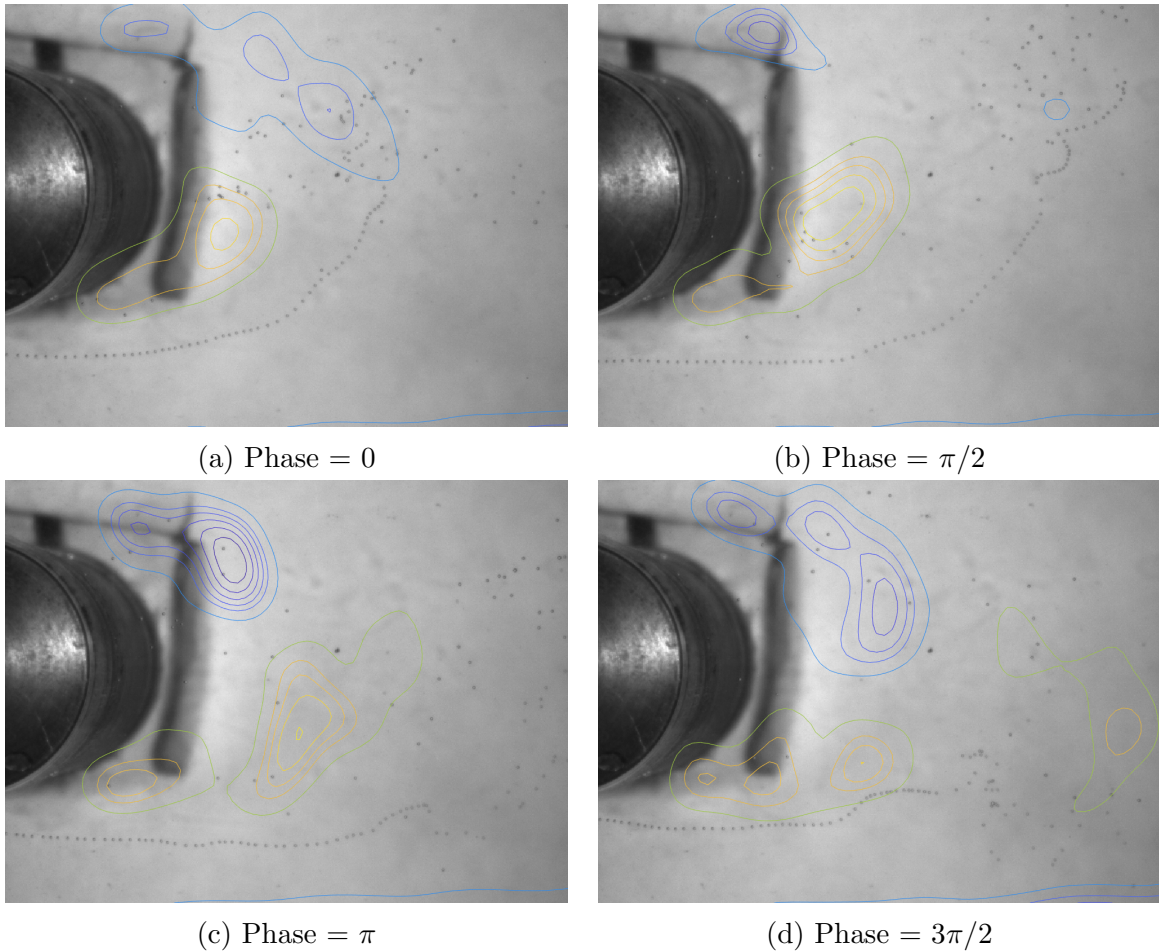
Figure 5.9: Snapshots of 281 $\mu m \pm 31$ μm bubble motion during shedding cycle (indicated by range $[0, 2\pi]$) with overlaid centerline vorticity contours. Flow is from left to right.

aggregated. To perform phase averaging, one could use either pressure measurements or velocity measurements. A sample time series of pressure and velocity measurements is given in Fig. 5.12.

Both the pressure and x velocity measurements exhibit clear and regular peaks, and can be used to produce phase averaged measurements. There is a slight phase lag between the peaks in both sets of measurements. The x velocity was chosen as the method for generating phase averaged data moving forward, as the peaks corresponded directly to vortex positions within the wake. With this in mind, phase averaged measurements of velocity data and bubble position were created for four different bubble sizes. To illustrate how bubbles cluster within the flow field, phase averaged measurements of the bubble position are overlayed on the centerline vorticity contours (Fig. 5.13). Bubbles that are greater than 1 cm from the centerline are rejected from the analysis.

As given in Fig. 5.13, we can see that bubbles have a tendency to get pulled counter-

(a) Phase $= 0$ (b) Phase $= \pi/2$
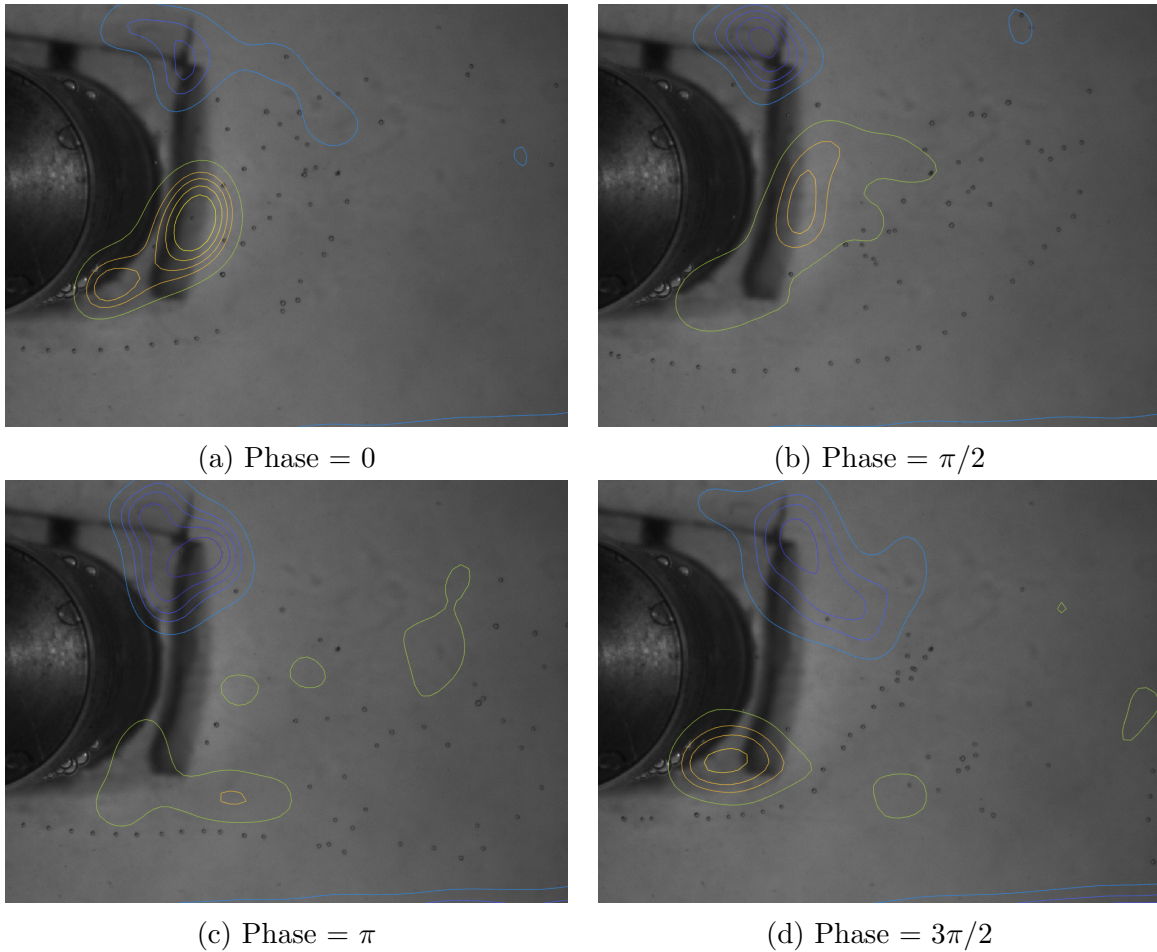
(c) Phase $= \pi$ (d) Phase $= 3\pi/2$
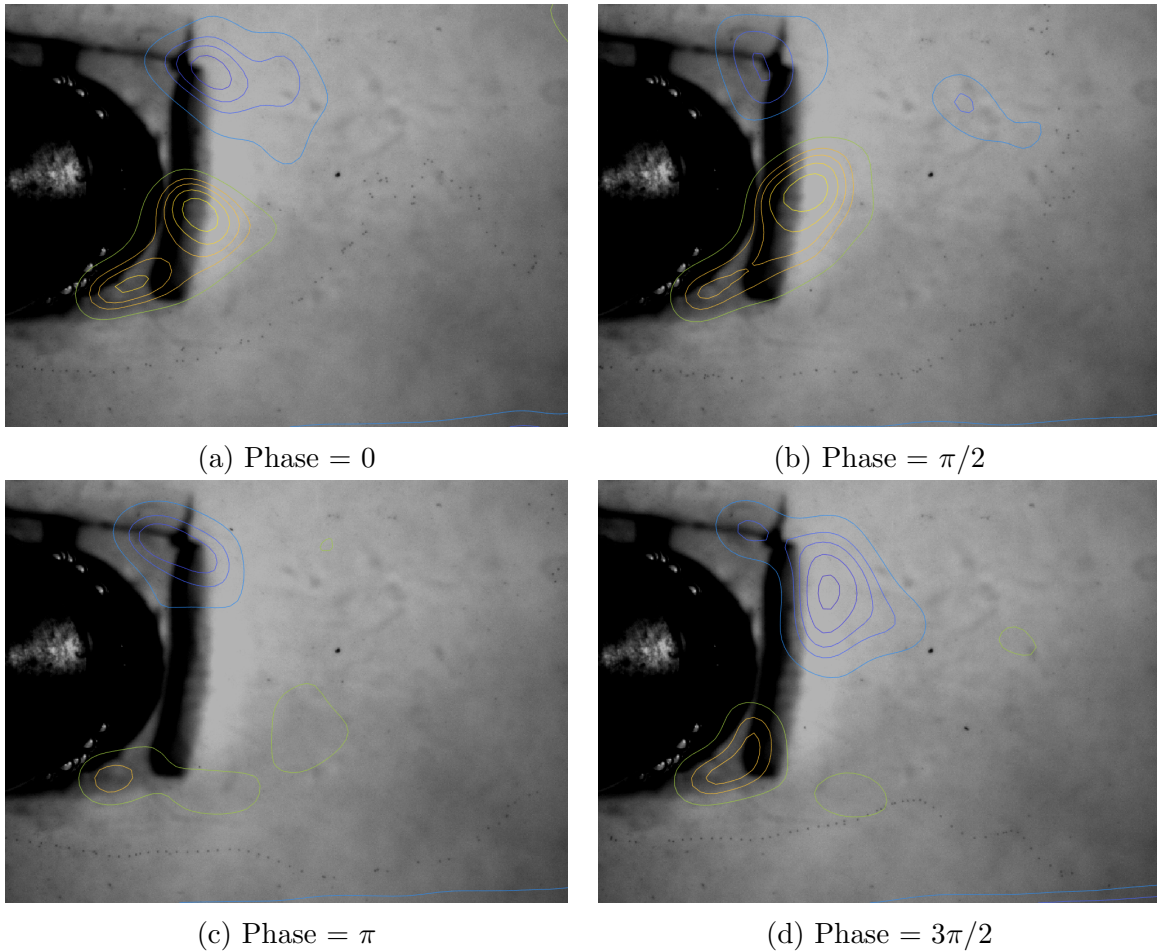
Figure 5.10: Snapshots of 210 μm $\pm$ 46 μm bubble motion during shedding cycle (indicated by range $[0, 2\pi]$) with overlaid centerline vorticity contours. Flow is from left to right.

clockwise into the CW vortex on the left hand side. However, the path the bubbles take, as well as the degree of clustering within the CCW vortex, depends strongly on bubble size. Larger bubbles tend to get pulled into the top of the CCW vortex, as well as the region between the CCW and CW vortex. Conversely, smaller bubbles have a tendency to get pulled over the top of the CCW vortex directly into the CW vortex on the left hand side. For the smaller two bubble sizes, very few bubbles are pulled within the CCW vortex, or into the gap region between the two vortices. Not only does this clustering substantially alter the likelihood of coalescence (for which this effect is qualitatively seen in Fig. 5.7), the positioning of bubbles within the shed vortices also alters the shape of the vortices. The largest bubbles stretch the core of the CCW vortex vertically, instead of the angled orientation seen in the other cases. Furthermore, the left hand side of the CCW vortex has heavily distorted contours.

While the distortion experienced with smaller bubble sizes is reduced, path dependent

(a) 2D position.
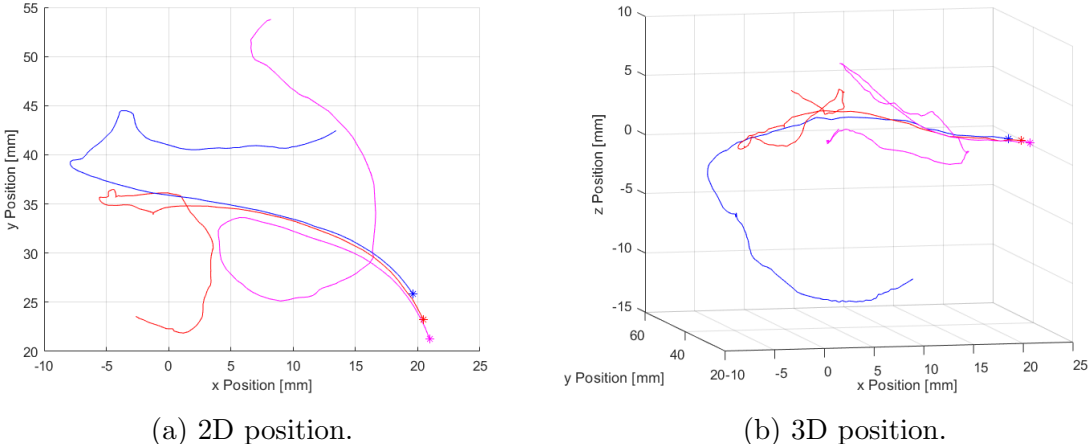
(b) 3D position.

Figure 5.11: Time-dependent bubble position of three bubbles which are initially in close proximity. The start of the trajectory is indicated by *.

(a) Pressure measurement.
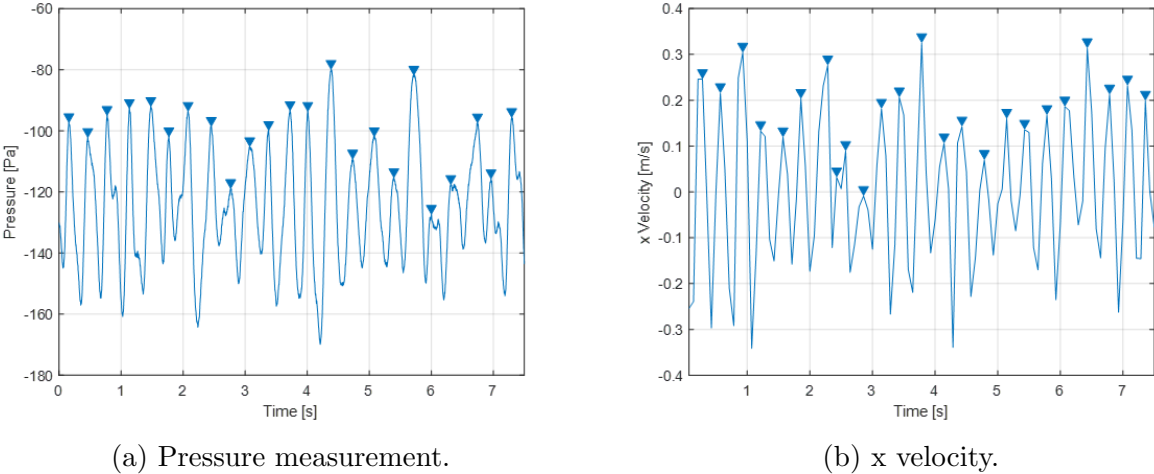
(b) x velocity.

Figure 5.12: Time series of pointwise pressure and velocity data, for which peaks are indications of a new shedding cycle. The pressure data was obtained 90° clockwise from front stagnation point, while the velocity data was measured at [x, y] = [0.002D, 0.74D]. X velocity measurements are used in subsequent datasets as method for generating phase averaged data.

(a) 210 μm ± 46 μm

(b) 281 μm ± 31 μm

(c) 487 μm ± 78 μm

(d) 673 μm ± 59 μm
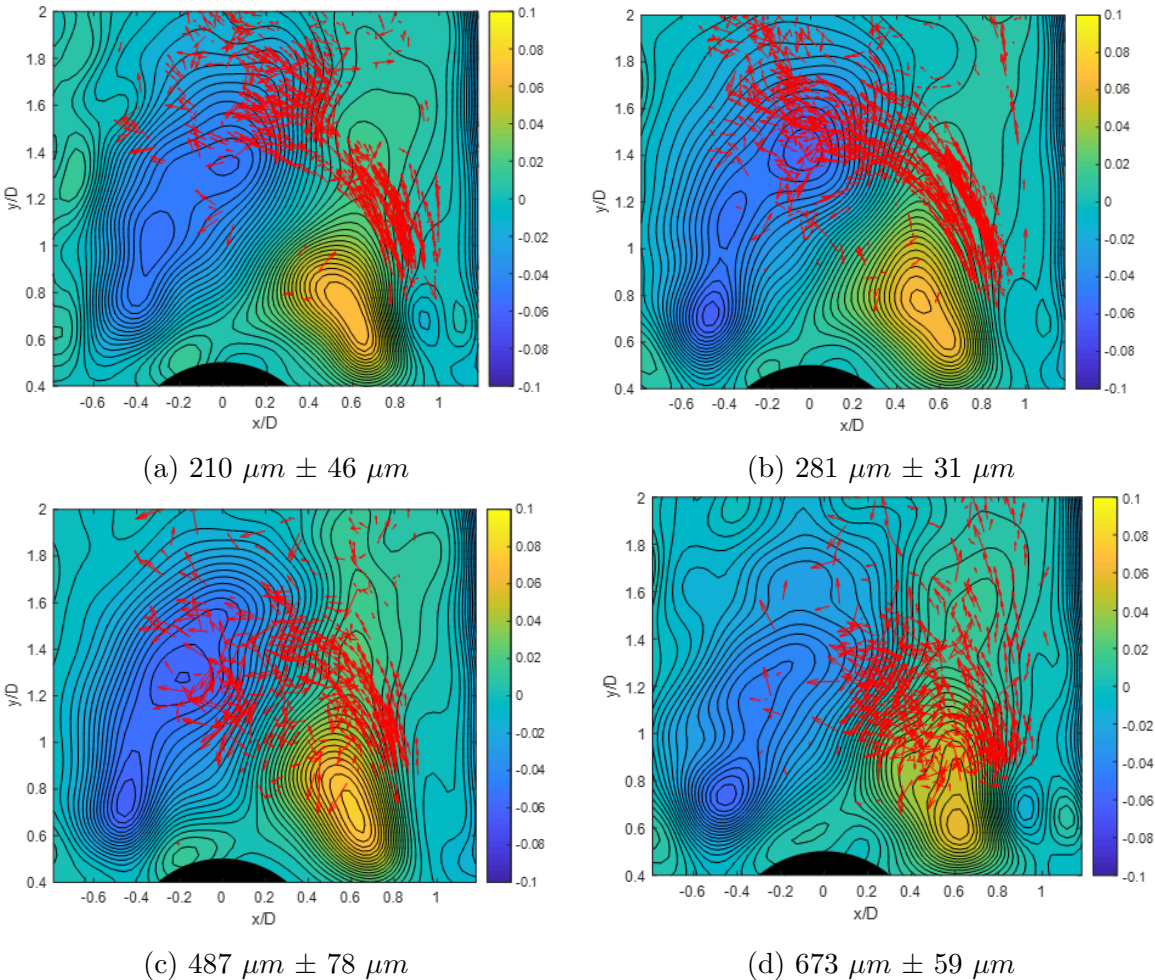
Figure 5.13: Phase averaged bubble positions and instantaneous velocity vectors overlayed on centerline vorticity contours. Only bubbles within 1 cm of centerline are pictured. Positive vorticity indicates counter-clockwise (CCW) rotation, while negative vorticity corresponds to clockwise (CW) rotation.

(a) 210 $\mu m \pm 46 \mu m$

(b) 281 $\mu m \pm 31 \mu m$

(c) 487 $\mu m \pm 78 \mu m$

(d) 673 $\mu m \pm 59 \mu m$
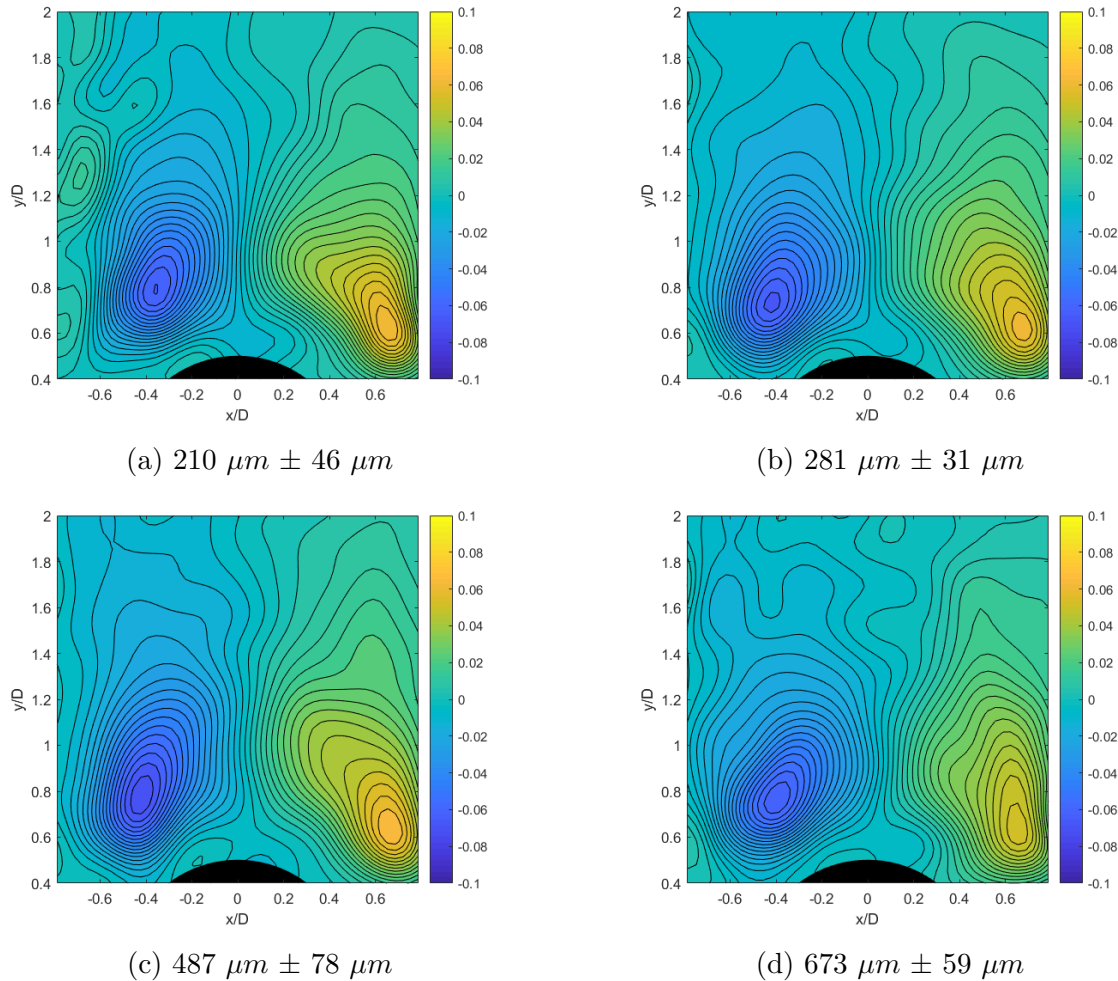
Figure 5.14: Time averaged centerline vorticity contours as a function of bubble size.

distortion is still apparent. In particular, the CCW vortex is stretched vertically towards the path that 281 $\mu m \pm 31 \mu m$ bubbles take above the vortex. Conversely, this vortex stretching behaviour is not observed for the 210 $\mu m \pm 46 \mu m$ bubbles (likely due to the fact that less momentum is imparted onto the flow for these bubble sizes).

To further illustrate the effect of bubble size on the vortex structure, the time-averaged vorticity contours across all shedding cycles are shown in Fig. 5.14. For the largest bubble size, the CCW vortex core is stretched vertically. Furthermore, the vortex strength is reduced. This reduction in strength, combined with the path dependent vortex distortion noted above, could be important in understanding why the shedding frequency changes with bubbles present in the flow. Note that the PIV laser is directed at the cylinder from the right hand side; therefore, CW vorticity measurements couldn't be made in the shadow region directly to the left of the cylinder.

In summary, there are several experimental effects which have been identified. These

effects are specific to a Reynolds number of $Re_D = 8100$ and a bubble diameter size range of 210 - 670 μm; however, they are illustrative of the type of effects which can be expected in other parameter ranges.

1. The degree of bubble clustering in the wake increases with bubble size, and for sufficiently small bubbles (210 μm) there is very little clustering within 2D downstream.

2. Very little bubble coalescence occurs at bubble size ranges below 500 μm, however, coalescence becomes significant at a size of 670 μm.

3. The mean trajectory taken in the wake is bubble size dependent. The vortex core is stretched towards the mean bubble trajectory. In the case that bubbles are consistently trapped within the vortex (e.g. 673 μm bubbles), the core region is stretched both vertically and laterally.

4. For the 673 μm bubble size, the CCW vortex strength was reduced significantly when compared to other bubble sizes. This is likely due to the trapping and motion of bubbles within the vortex.

5. Very few bubbles were required to alter the vortex structure. These effects were observed at void fractions below 0.0005%.

While these results are specific to the studied Reynolds number and bubble size range, the bubble size dependent capture and distortion of vortices in the cylinder wake has not yet been described. As opposed to previous literature which has studied vortex distortion in unobstructed flows, the size dependent bubble capture is a function of the path taken by bubbles around the obstacle. Consequently, for sufficiently small bubble sizes there is very little vortex trapping in the near wake. Increased research into the bubble size dependent capture and distortion of the shed vortices may shed light bubble size dependent change in shedding frequency, and warrants future study.

Chapter 6

Conclusions

The study of multiphase flow transport presents a formidable challenge, as well as a wealth of active research areas. A distinct feature of these types of flows is the clustering of the dispersed phase by vortical flow structures, which results in many interesting one- and two-way coupled effects. In an effort to study the effect of coupling on dispersed flow transport, results have been presented for two projects:

1. Studying the transport and deposition of water density matched particles expelled into air.

2. Studying the capture and transport of dispersed air bubbles within cross flow over a cylinder.

While both projects study the transport of air/water mixtures, the density ratio of the dispersed and carrier phases is flipped between the two cases. Dense particles are flung from vortices while lighter bubbles preferentially accumulate in vortices. This redistribution of the dispersed phase results in many interesting effects, which are summarized briefly below.

Particle and Droplet Transport in Air The transport of dense particles/droplets in air was motivated by the study of disease transport, for which the motion of expelled droplets is highly dependent on the environment in which they are ejected. To control for environmental effects, a quiescent, isothermal, and isopotential chamber was built and methods were developed to track particle and droplet motion within the room.

The developed methods were subsequently applied to the transport and deposition of 22-212 μm particles suspended within a steady state jet. The transport of nominal "aerosol" particles (22-27 μm) was shown to be highly dependent on the production of secondary flows within the room, for which CFD models struggled to replicate the deposition pattern [1]. The growing application and development of advanced CFD tools necessitates the development of suitable experimental studies for model validation, but as discussed in Section 2.1 such studies do not yet exist for practical geometries. Model validation experiments should carefully characterize or eliminate thermal gradients, ambient flows and charge effects. Methods

for studying particle deposition must be accurate across a wide range of particle sizes, which is challenging with optical methods. The steps needed (e.g. room and sampling strip charge neutralization, and significant thermal insulation) suggests that in many studies that did not explicitly consider such effects and go to great lengths to mitigate them, results should be viewed cautiously with appreciation of the effects that may have influenced the data yet have not been described. I hope that future research can build on the methods presented here to improve the quality of available validation studies. In the meantime, I hope that experimental studies in simplified geometries (such as the data presented in here) see increased use in numerical model validation, as predicting mid–size particle transport is shown to be highly non–trivial.

In the second part of this project, the effect of a realistic oral cavity on particle dispersal was studied across the same particle size range. The data suggests a clear effect on particle deposition from the cough release geometry, which is in agreement with what is expected given the modified Stokes number of the released particles. Particles deposit in an eddying pattern, which is a frozen signature of the initial particle clustering near to the mouth. The pattern fading further downstream implies that there will still be a 'far field' distance at which the effects of the oral cavity geometry can be neglected. In this region, a more general approximation of the flow field is likely sufficient, provided that the initial preferential clustering of particles has been accounted for. However, studies that are attempting to predict particle transport on the order of typical social distancing (recommended social distancing guideline is 1.8 m (6 ft) as given in [102]) between individuals should consider the oral cavity as something more complex than a plain round or elliptical orifice.

Through the results presented in both projects, it is clear that particle transport is strongly affected by (1) secondary flows caused by thermal gradients or end wall effects, as well as (2) inlet boundary conditions. Preferential accumulation, coupled with long residence times of low Stokes number particles, increases the importance of these effects. Consequently, the general rules of thumb for single phase flow, such as the understanding that inlet geometry ceases to affect the flow by $O(10)$ diameters downstream [167], do not necessarily apply to the multiphase case. High quality validation experiments are needed to develop similar guidelines for dispersed multiphase flow transport.

Bubble Flow Around a Cylinder The study of bubbly flows past a cylinder was motivated by the changing shedding frequency from the single phase case, for which a comprehensive explanation has yet to be provided in literature. Numerical and experimental techniques were applied to study the motion of dilute (nominally one-way coupled) bubble concentrations in the vicinity of the cylinder. While the numerical results were primarily qualitative, several important effects were identified:

1. There is a region which is largely devoid of bubbles upstream of the cylinder. This region leads to the formation of streamlines with higher bubble density.

2. The likelihood that bubbles are captured in the shed vortices is a strong function of

bubble size. The highest probability of capture for $Re_D = 20000$ is an intermediate size within the d = $[200, 3000]$ μm studied range.

3. The orbital motion taken by bubbles as they approach the vortex is a strong function of bubble size. Once bubbles reach an equilibrium position within the vortex it is clear that there is a finite offset from the vortex centre. This effect mirrors that shown in previous works (reviewed in section 4.1).

The identification of an intermediate bubble size with the highest probability of capture illustrates the nonlinear nature of bubble motion in the wake; namely, the capture probability depends on both the redistribution of bubbles around the obstacle as well as the time-dependent looping approach of a bubble towards a vortex. The determination of these capture probabilities requires the use of experiments or high fidelity numerical simulations, which illustrates the challenge of studying bubbly flow over a cylinder. The probability of capture is expected to relate to the likelihood of coalescence as well as vortex stretching and deformation; both effects are likely important in determining how the shedding frequency changes. However, the numerical results were one-way coupled so by definition no changes in the carrier fluid could be observed.

To study two-way coupled effects, experiments were conducted. The experiments studied a monodisperse stream of bubbles (with a diameter of 210 - 670 μm) at an upstream global void fraction of less than 0.0005%. The Reynolds number was $Re_D = 8100$. Several interesting phenomena were observed:

1. The degree of bubble clustering in the wake increases with bubble size, and for sufficiently small bubbles (210 μm) there is very little clustering within 2D downstream.

2. Very little bubble coalescence occurs at bubble size ranges below 500 μm, however, coalescence becomes significant at a size of 670 μm.

3. The mean trajectory taken in the wake is bubble size dependent. The vortex core is stretched towards the mean bubble trajectory. In the case that bubbles are consistently trapped within the vortex (e.g. 673 μm bubbles), the core region is stretched both vertically and laterally.

4. For the 673 μm bubble size, the CCW vortex strength was reduced significantly when compared to other bubble sizes. This is likely due to the trapping and motion of bubbles within the vortex.

5. Very few bubbles were required to alter the vortex structure. These effects were observed at void fractions below 0.0005%.

Consequently, the capture probability appears to relate to the degree of both (1) coalescence and (2) vortex stretching and distortion. While the experimentally studied Reynolds number and bubble size range was such that these effects increased monotonically with

bubble size, the numerical results suggest that for a given Reynolds number these effects would be maximized at a particular bubble size range. While no changes in the shedding frequency were observed, the study of vortex distortion is a first step to understanding why the shedding frequency has a bubble size dependence.

6.1 Future Research Directions

The methods developed for studying bubbly flow past a cylinder are valuable for predicting vortex capture (numerically) and observing the resulting bubble coalescence and vortex distortion (experimentally). The numerical simulations and experimental results cannot yet be compared as the numerical simulations are only for a 2D flow. Work is currently being undertaken to extend the same numerical approach to a 3D confined channel (with 25% blockage), which will allow for direct comparison to experiments.

Experimentally, work is being undertaken to increase the Reynolds number range. As predicted with the numerical simulations, there should be an intermediate bubble size which maximizes vortex distortion and coalescence for a given Reynolds number. Sweeping a larger parameter space of Reynolds number and bubble size will allow for an increased understanding of this effect.

Lastly, work is being undertaken to study the flow at higher void fractions, in which the shedding frequency is altered. This set of experiments allows for the coupling of information on vortex distortion with observable changes in the shedding frequency. The combined set of experiments will allow for development of a complete theory on the change in shedding frequency with changing void fraction and bubble size.

Bibliography

[1]   E. Thacher, T. Carlson, J. Castellini, M. D. Sohn, E. Variano, and S. A. Mäkiharju, "Droplet and particle methods to investigate turbulent particle laden jets," *Aerosol Science and Technology*, vol. 55, no. 12, pp. 1359–1377, 2021.

[2]   K. Zaman, "Axis switching and spreading of an asymmetric jet: the role of coherent structure dynamics," *Journal of Fluid Mechanics*, vol. 316, pp. 1–27, 1996.

[3]   E. Thacher and S. A. Mäkiharju, "Effect of coherent structures on particle transport and deposition from a cough," *Aerosol Science and Technology*, vol. 56, no. 5, pp. 425–433, 2022.

[4]   S. Balachandar and J. K. Eaton, "Turbulent dispersed multiphase flow," *Annual review of fluid mechanics*, vol. 42, pp. 111–133, 2010.

[5]   M. R. Maxey and J. J. Riley, "Equation of motion for a small rigid sphere in a nonuniform flow," *The Physics of Fluids*, vol. 26, no. 4, pp. 883–889, 1983.

[6]   E. E. Michaelides, "The transient equation of motion for particles, bubbles, and droplets," 1997.

[7]   R. Clift and W. Gauvin, "The motion of particles in turbulent gas-streams," *Proc. Chemeca'70*, vol. 1, p. 14, 1970.

[8]   C. Crowe, M. Sommerfeld, and Y. Tsuji, *Multiphase Flows with Droplets and Particles*. Ž, 1998.

[9]   N. Moradian, D. S.-K. Ting, and S. Cheng, "The effects of freestream turbulence on the drag coefficient of a sphere," *Experimental thermal and fluid science*, vol. 33, no. 3, pp. 460–471, 2009.

[10] E. Guazzelli and J. F. Morris, *A physical introduction to suspension dynamics*. Cambridge University Press, 2011, vol. 45.

[11] A. A. Kulkarni and J. B. Joshi, "Bubble formation and bubble rise velocity in gas-liquid systems: a review," *Industrial & engineering chemistry research*, vol. 44, no. 16, pp. 5873–5931, 2005.

[12]   G. Ryskin and L. Leal, "Numerical solution of free-boundary problems in fluid mechanics. part 2. buoyancy-driven motion of a gas bubble through a quiescent liquid," *Journal of Fluid Mechanics*, vol. 148, pp. 19–35, 1984.

[13]   G. F. Oweis, I. Van der Hout, C. Iyer, G. Tryggvason, and S. L. Ceccio, "Capture and inception of bubbles near line vortices," *Physics of Fluids*, vol. 17, no. 2, p. 022105, 2005.

[14]   R. Jones and M. Nicas, "Experimental determination of supermicrometer particle fate subsequent to a point release within a room under natural and forced mixing," *Aerosol Science and Technology*, vol. 43, pp. 921–938, 2009.

[15]   C. Stan, D. Milathianaki, H. Laksmono, R. Sierra, T. McQueen, M. Messerschmidt, G. Williams, J. Koglin, T. Lane, M. Hayes, S. Guillet, M. Liang, A. Aquila, P. Willmott, J. Robinson, K. Gumerlock, S. Botha, K. Nass, I. Schlichting, R. Shoeman, H. Stone, and S. Boutet, "Liquid explosions induced by x-ray laser pulses," *Nature Physics*, vol. 12, pp. 966–972, 2016.

[16]   M. R. Maxey, "The gravitational settling of aerosol particles in homogeneous turbulence and random flow fields," *Journal of fluid mechanics*, vol. 174, pp. 441–465, 1987.

[17]   J. Davila and J. C. Hunt, "Settling of small particles near vortices and in turbulence," *Journal of Fluid Mechanics*, vol. 440, pp. 117–145, 2001.

[18]   S. I. Green, *Introduction to Vorticity*.   Dordrecht: Springer Netherlands, 1995, pp. 1–34. [Online]. Available: https://doi.org/10.1007/978-94-011-0249-0_1

[19]   S. Elghobashi, "On predicting particle-laden turbulent flows," *Applied scientific research*, vol. 52, no. 4, pp. 309–329, 1994.

[20]   S. Elgobashi, "An updated classification map of particle-laden turbulent flows," in *IUTAM Symposium on Computational Approaches to Multiphase Flow*.   Springer, 2006, pp. 3–10.

[21]   V. Mathai, D. Lohse, and C. Sun, "Bubbly and buoyant particle–laden turbulent flows," *Annual Review of Condensed Matter Physics*, vol. 11, pp. 529–559, 2020.

[22]   N. K. Jha and R. Govardhan, "Interaction of a vortex ring with a single bubble: bubble and vorticity dynamics," *Journal of Fluid Mechanics*, vol. 773, pp. 460–497, 2015.

[23]   W. F. Wells, "On air-borne infection: study ii. droplets and droplet nuclei." *American journal of Epidemiology*, vol. 20, no. 3, pp. 611–618, 1934.

[24]   A. D. Bordoloi, C. C. K. Lai, L. Clark, G. V. Carrillo, and E. Variano, "Turbulence statistics in a negatively buoyant multiphase plume," *Journal of Fluid Mechanics*, vol. 896, p. A19, 2020.

[25] P. Bahl, C. Doolan, C. De Silva, A. A. Chughtai, L. Bourouiba, and C. R. MacIntyre, "Airborne or droplet precautions for health workers treating covid-19?" *The Journal of infectious diseases*, 2020.

[26] M. Jayaweera, H. Perera, B. Gunawardana, and J. Manatunge, "Transmission of covid-19 virus by droplets and aerosols: A critical review on the unresolved dichotomy," *Environmental research*, p. 109819, 2020.

[27] M. A. Kohanski, L. J. Lo, and M. S. Waring, "Review of indoor aerosol generation, transport, and control in the context of covid-19," in *International forum of allergy & rhinology*, vol. 10, no. 10.   Wiley Online Library, 2020, pp. 1173–1179.

[28] D. K. Chu, E. A. Akl, S. Duda, K. Solo, S. Yaacoub, H. J. Schünemann, A. El-harakeh, A. Bognanni, T. Lotfi, M. Loeb *et al.*, "Physical distancing, face masks, and eye protection to prevent person-to-person transmission of sars-cov-2 and covid-19: a systematic review and meta-analysis," *The Lancet*, vol. 395, no. 10242, pp. 1973–1987, 2020.

[29] G. Sze To, M. Wan, C. Chao, F. Wei, S. Yu, and J. Kwan, "A methodology for estimating airborne virus exposures in indoor environments using the spatial distribution of expiratory aerosols and virus viability characteristics." *Indoor air*, vol. 18, no. 5, pp. 425–438, 2008.

[30] M. Wan, C. Y. H. Chao, Y. Ng, G. N. Sze To, and W. Yu, "Dispersion of expiratory droplets in a general hospital ward with ceiling mixing type mechanical ventilation system," *Aerosol Science and Technology*, vol. 41, no. 3, pp. 244–258, 2007.

[31] H. Qian and Y. Li, "Removal of exhaled particles by ventilation and deposition in a multibed airborne infection isolation room," *Indoor air*, vol. 20, no. 4, pp. 284–297, 2010.

[32] W. G. Lindsley, W. P. King, R. E. Thewlis, J. S. Reynolds, K. Panday, G. Cao, and J. V. Szalajda, "Dispersion and exposure to a cough-generated aerosol in a simulated medical examination room," *Journal of occupational and environmental hygiene*, vol. 9, no. 12, pp. 681–690, 2012.

[33] K. Nissen, J. Krambrich, D. Akaberi, T. Hoffman, J. Ling, Å. Lundkvist, L. Svensson, and E. Salaneck, "Long-distance airborne dispersal of sars-cov-2 in covid-19 wards," *Scientific reports*, vol. 10, no. 1, pp. 1–9, 2020.

[34] Z. Zhang, X. Chen, S. Mazumdar, T. Zhang, and Q. Chen, "Experimental and numerical investigation of airflow and contaminant transport in an airliner cabin mockup," *Building and Environment*, vol. 44, no. 1, pp. 85–94, 2009.

[35] Z. Liu, W. Zhuang, L. Hu, R. Rong, J. Li, W. Ding, and N. Li, "Experimental and numerical study of potential infection risks from exposure to bioaerosols in one bsl-3 laboratory," *Building and environment*, vol. 179, p. 106991, 2020.

[36] J. Richmond-Bryant, A. Eisner, L. Brixey, and R. Wiener, "Transport of airborne particles within a room." *Indoor Air*, vol. 16, no. 1, pp. 48–55, 2006.

[37] S. Miller and W. Nazaroff, "Environmental tobacco smoke particles in multizone indoor environments," *Atmospheric Environment*, vol. 35, no. 12, pp. 2053–2067, 2001.

[38] Z. Zhang and Q. Chen, "Experimental measurements and numerical simulations of particle transport and distribution in ventilated rooms," *Atmospheric environment*, vol. 40, no. 18, pp. 3396–3408, 2006.

[39] S. Murakami, "Diffusion characteristics of airborne particles with gravitational setting in an convection-dominant indoor flow field," *Ashrae Transactions*, vol. 98, no. 1, pp. 82–97, 1992.

[40] S. Liu and A. Novoselac, "Transport of airborne particles from an unobstructed cough jet," *Aerosol Science and Technology*, vol. 48, no. 11, pp. 1183–1194, 2014.

[41] A. C. Lai and S.-L. Wong, "Experimental investigation of exhaled aerosol transport under two ventilation systems," *Aerosol Science and Technology*, vol. 44, no. 6, pp. 444–452, 2010.

[42] C. Chao and M. Wan, "A study of the dispersion of expiratory aerosols in unidirectional downward and ceiling-return type airflows using a multiphase approach." *Indoor air*, vol. 16, no. 4, pp. 296–312, 2006.

[43] A. Jurelionis, L. Gagytė, T. Prasauskas, D. Čiužas, E. Krugly, L. Šeduikytė, and D. Martuzevičius, "The impact of the air distribution method in ventilated rooms on the aerosol particle dispersion and removal: The experimental approach," *Energy and Buildings*, vol. 86, pp. 305–313, 2015.

[44] H. Jin, Q. Li, L. Chen, J. Fan, and L. Lu, "Experimental analysis of particle concentration heterogeneity in a ventilated scale chamber," *Atmospheric Environment*, vol. 43, no. 28, pp. 4311–4318, 2009.

[45] D. Bolster and P. Linden, "Particle transport in low-energy ventilation systems. part 2: Transients and experiments," *Indoor air*, vol. 19, no. 2, pp. 130–44, 2009.

[46] S. Seepana and A. C. Lai, "Experimental and numerical investigation of interpersonal exposure of sneezing in a full-scale chamber," *Aerosol Science and Technology*, vol. 46, no. 5, pp. 485–493, 2012.

[47] J. Wei and Y. Li, "Human cough as a two-stage jet and its role in particle transport," *PloS one*, vol. 12, no. 1, p. e0169235, 2017.

[48] S. Zhu, S. Kato, and J.-H. Yang, "Study on transport characteristics of saliva droplets produced by coughing in a calm indoor environment," *Building and environment*, vol. 41, no. 12, pp. 1691–1702, 2006.

[49] L. Bourouiba, E. Dehandschoewercker, and J. W. Bush, "Violent expiratory events: on coughing and sneezing," *Journal of Fluid Mechanics*, vol. 745, pp. 537–563, 2014.

[50] L. Bourouiba, "A sneeze," *New England Journal of Medicine*, vol. 375, no. 8, p. e15, 2016.

[51] J. Lee, D. Yoo, S. Ryu, S. Ham, K. Lee, M. Yeo, K. Min, C. Yoon *et al.*, "Quantity, size distribution, and characteristics of cough-generated aerosol produced by patients with an upper respiratory tract infection," *Aerosol and Air Quality Research*, vol. 19, no. 4, pp. 840–853, 2019.

[52] N. Zhang, Z. Zheng, S. Eckels, V. B. Nadella, and X. Sun, "Transient response of particle distribution in a chamber to transient particle injection," *Particle & Particle Systems Characterization*, vol. 26, no. 4, pp. 199–209, 2009.

[53] E. Sajo, H. Zhu, and J. Courtney, "Spatial distribution of indoor aerosol deposition under accidental release conditions," *Health physics*, vol. 83, no. 6, pp. 871–883, 2002.

[54] J. W. Tang, W. P. Bahnfleth, P. M. Bluyssen, G. Buonanno, J. L. Jimenez, J. Kurnitski, Y. Li, S. Miller, C. Sekhar, L. Morawska *et al.*, "Dismantling myths on the airborne transmission of severe acute respiratory syndrome coronavirus (sars-cov-2)," *Journal of Hospital Infection*, 2021.

[55] R. M. Jones and M. Nicas, "Experimental evaluation of a markov multizone model of particulate contaminant transport," *Annals of occupational hygiene*, vol. 58, no. 8, pp. 1032–1045, 2014.

[56] W. C. Hinds, *Aerosol technology: properties, behavior, and measurement of airborne particles*.   John Wiley & Sons, 1999.

[57] B. Wang, H. Wu, and X.-F. Wan, "Transport and fate of human expiratory droplets—a modeling approach," *Physics of Fluids*, vol. 32, no. 8, p. 083307, 2020.

[58] J. Wei and Y. Li, "Enhanced spread of expiratory droplets by turbulence in a cough jet," *Building and Environment*, vol. 93, pp. 86–96, 2015.

[59] J. W. Tang, T. J. Liebner, B. A. Craven, and G. S. Settles, "A schlieren optical study of the human cough with and without wearing masks for aerosol infection control," *Journal of the Royal Society Interface*, vol. 6, no. suppl_6, pp. S727–S736, 2009.

[60] S. Yang, G. W. Lee, C.-M. Chen, C.-C. Wu, and K.-P. Yu, "The size and concentration of droplets generated by coughing in human subjects," *Journal of Aerosol Medicine*, vol. 20, no. 4, pp. 484–494, 2007.

[61] K. W. Hegland, M. S. Troche, and P. W. Davenport, "Cough expired volume and airflow rates during sequential induced cough," *Frontiers in physiology*, vol. 4, p. 167, 2013.

[62] J. K. Gupta, C.-H. Lin, and Q. Chen, "Flow dynamics and characterization of a cough," *Indoor air*, vol. 19, no. 6, pp. 517–525, 2009.

[63] C. Y. H. Chao, M. P. Wan, L. Morawska, G. R. Johnson, Z. Ristovski, M. Hargreaves, K. Mengersen, S. Corbett, Y. Li, X. Xie *et al.*, "Characterization of expiration air jets and droplet size distributions immediately at the mouth opening," *Journal of Aerosol Science*, vol. 40, no. 2, pp. 122–133, 2009.

[64] J. Duguid, "The size and the duration of air-carriage of respiratory droplets and droplet-nuclei," *Epidemiology & Infection*, vol. 44, no. 6, pp. 471–479, 1946.

[65] P. Prasanna Simha and P. S. Mohan Rao, "Universal trends in human cough airflows at large distances," *Physics of Fluids*, vol. 32, no. 8, p. 081905, 2020.

[66] N. Dudalski, A. Mohamed, S. Mubareka, R. Bi, C. Zhang, and E. Savory, "Experimental investigation of far-field human cough airflows from healthy and influenza-infected subjects," *Indoor air*, vol. 30, no. 5, pp. 966–977, 2020.

[67] E. Savory, W. E. Lin, K. Blackman, M. C. Roberto, L. R. Cuthbertson, J. A. Scott, and S. Mubareka, "Western cold and flu (wecof) aerosol study–preliminary results," *BMC research notes*, vol. 7, no. 1, pp. 1–11, 2014.

[68] M. VanSciver, S. Miller, and J. Hertzberg, "Particle image velocimetry of human cough," *Aerosol Science and Technology*, vol. 45, no. 3, pp. 415–422, 2011.

[69] S.-B. Kwon, J. Park, J. Jang, Y. Cho, D.-S. Park, C. Kim, G.-N. Bae, and A. Jang, "Study on the initial velocity distribution of exhaled air from coughing and speaking," *Chemosphere*, vol. 87, no. 11, pp. 1260–1264, 2012.

[70] J. W. Tang, A. Nicolle, J. Pantelic, G. C. Koh, L. D. Wang, M. Amin, C. A. Klettner, D. K. Cheong, C. Sekhar, and K. W. Tham, "Airflow dynamics of coughing in healthy human volunteers by shadowgraph imaging: an aid to aerosol infection control," *PLoS One*, vol. 7, no. 4, p. e34818, 2012.

[71] W. Sun and J. Ji, "Transport of droplets expelled by coughing in ventilated rooms," *Indoor and Built Environment*, vol. 16, no. 6, pp. 493–504, 2007.

[72] J. Redrow, S. Mao, I. Celik, J. A. Posada, and Z.-g. Feng, "Modeling the evaporation and dispersion of airborne sputum droplets expelled from a human cough," *Building and Environment*, vol. 46, no. 10, pp. 2042–2051, 2011.

[73] F. Berlanga, I. Olmedo, and M. Ruiz de Adana, "Experimental analysis of the air velocity and contaminant dispersion of human exhalation flows," *Indoor Air*, vol. 27, no. 4, pp. 803–815, 2017.

[74] L. Feng, S. Yao, H. Sun, N. Jiang, and J. Liu, "Tr-piv measurement of exhaled flow using a breathing thermal manikin," *Building and environment*, vol. 94, pp. 683–693, 2015.

[75] H. Qian, Y. Li, P. V. Nielsen, C.-E. Hyldgaard, T. W. Wong, and A. Chwang, "Dispersion of exhaled droplet nuclei in a two-bed hospital ward with three different ventilation systems." *Indoor air*, vol. 16, no. 2, pp. 111–128, 2006.

[76] L. Yang, X. Li, Y. Yan, and J. Tu, "Effects of cough-jet on airflow and contaminant transport in an airliner cabin section," *The Journal of Computational Multiphase Flows*, vol. 10, no. 2, pp. 72–82, 2018.

[77] J. Villafruela, I. Olmedo, and J. San José, "Influence of human breathing modes on airborne cross infection risk," *Building and Environment*, vol. 106, pp. 340–351, 2016.

[78] C. Xu, P. Nielsen, G. Gong, R. Jensen, and L. Liu, "Influence of air stability and metabolic rate on exhaled flow," *Indoor air*, vol. 25, no. 2, pp. 198–209, 2015.

[79] F. Berlanga, L. Liu, P. V. Nielsen, R. L. Jensen, A. Costa, I. Olmedo, and M. R. de Adana, "Influence of the geometry of the airways on the characterization of exhalation flows. comparison between two different airway complexity levels performing two different breathing functions," *Sustainable Cities and Society*, vol. 53, p. 101874, 2020.

[80] M. Duan, L. Liu, G. Da, E. Géhin, P. V. Nielsen, U. M. Weinreich, B. Lin, Y. Wang, T. Zhang, and W. Sun, "Measuring the administered dose of particles on the facial mucosa of a realistic human model," *Indoor air*, vol. 30, no. 1, pp. 108–116, 2020.

[81] M. Han, R. Ooka, H. Kikumoto, W. Oh, Y. Bu, and S. Hu, "Measurements of exhaled airflow velocity through human coughs using particle image velocimetry," *Building and Environment*, p. 108020, 2021.

[82] J. K. Eaton and J. Fessler, "Preferential concentration of particles by turbulence," *International Journal of Multiphase Flow*, vol. 20, pp. 169–209, 1994.

[83] W. K. George, "The self-preservation of turbulent flows and its relation to initial conditions and coherent structures," *Advances in turbulence*, vol. 3973, 1989.

[84] B. J. Boersma, G. Brethouwer, and F. T. Nieuwstadt, "A numerical investigation on the effect of the inflow conditions on the self-similar region of a round jet," *Physics of fluids*, vol. 10, no. 4, pp. 899–909, 1998.

[85] J. Hunt, R. Delfos, I. Eames, and R. J. Perkins, "Vortices, complex flows and inertial particles," *Flow, turbulence and combustion*, vol. 79, no. 3, pp. 207–234, 2007.

[86] X. Yang, N. Thomas, and L. Guo, "Particle dispersion in organized vortex structures within turbulent free shear flows," *Chemical engineering science*, vol. 55, no. 7, pp. 1305–1324, 2000.

[87] I. Eames and M. Gilbertson, "The settling and dispersion of small dense particles by spherical vortices," *Journal of Fluid Mechanics*, vol. 498, pp. 183–203, 2004.

[88] F. Wen, N. Kamalu, J. Chung, C. Crowe, and T. Troutt, "Particle dispersion by vortex structures in plane mixing layers," *Journal of Fluids Engineering*, vol. 114, pp. 657–666, 1992.

[89] R. Perkins, S. Ghosh, and J. Phillips, "The interaction between particles and coherent structures in a plane turbulent jet," in *Advances in Turbulence 3*. Springer, 1991, pp. 93–100.

[90] L. Tang, F. Wen, Y. Yang, C. Crowe, J. Chung, and T. Troutt, "Self-organizing particle dispersion mechanism in a plane wake," *Physics of Fluids A: Fluid Dynamics*, vol. 4, no. 10, pp. 2244–2251, 1992.

[91] B. Lazaro and J. Lasheras, "Particle dispersion in a turbulent, plane, free shear layer," *Physics of Fluids A: Fluid Dynamics*, vol. 1, no. 6, pp. 1035–1044, 1989.

[92] C. Casciola, P. Gualtieri, F. Picano, G. Sardina, and G. Troiani, "Dynamics of inertial particles in free jets," *Physica Scripta*, vol. 2010, no. T142, p. 014001, 2010.

[93] F. Picano, G. Sardina, P. Gualtieri, and C. Casciola, "Anomalous memory effects on transport of inertial particles in turbulent jets," *Physics of Fluids*, vol. 22, no. 5, p. 051705, 2010.

[94] W. Yang and L. C. Marr, "Dynamics of airborne influenza a viruses indoors and dependence on humidity," *PloS one*, vol. 6, no. 6, 2011.

[95] M. Taghavivand, P. Mehrani, A. Sowinski, and K. Choi, "Electrostatic charging behaviour of polypropylene particles during pulse pneumatic conveying with spiral gas flow pattern," *Chemical Engineering Science*, vol. 229, p. 116081, 2021.

[96] T. Matsuyama, "A discussion on maximum charge held by a single particle due to gas discharge limitation," in *AIP Conference Proceedings*, vol. 1927, no. 1. AIP Publishing LLC, 2018, p. 020001.

[97]   F. Picano, G. Sardina, and C. Casciola, "Spatial development of particle-laden turbulent pipe flow," *Physics of Fluids*, vol. 21, no. 9, p. 093305, 2009.

[98]   H. Ge, L. Chen, C. Xu, and X. Cui, "Large-eddy simulation of droplet-laden cough jets with a realistic manikin model," *Indoor and Built Environment*, p. 1420326X211032247, 2021.

[99]   J. Jimenez, "A spanwise structure in the plane shear layer," *Journal of Fluid Mechanics*, vol. 132, pp. 319–336, 1983.

[100] M. A. Hernan and J. Jimenez, "Computer analysis of a high-speed film of the plane turbulent mixing layer," *Journal of Fluid Mechanics*, vol. 119, pp. 323–345, 1982.

[101] L.-S. Huang and C.-M. Ho, "Small-scale transition in a plane mixing layer," *Journal of Fluid Mechanics*, vol. 210, pp. 475–500, 1990.

[102] S. Balachandar, S. Zaleski, A. Soldati, G. Ahmadi, and L. Bourouiba, "Host-to-host airborne transmission as a multiphase flow problem for science-based social distance guidelines," 2020.

[103] S. Kaneko, T. Nakamura, F. Inada, M. Kato, K. Ishihara, T. Nishihara, and M.A.Langthjem, Eds., *Flow-Induced Vibrations: Classifications and Lessons from Practical Experiences*, 2nd ed.   Elsevier, 2014.

[104] Z. Sun and H. Zhang, "Measurement of the flow rate and volume void fraction of gas-liquid bubble flow using a vortex flow meter," *Chemical Engineering Communications*, vol. 197, no. 2, pp. 145–157, 2009.

[105] A.W.Patwardhan and J.B.Joshi, "Design of stirred vessels with gas entrained from free liquid surface," *Canadian Journal of Chemical Engineering*, vol. 76, pp. 339–364, 1998.

[106] J.B.Yianatos, "Fluid flow and kinetic modelling in flotation related processes: Columns and mechanically agitated cells - a review," *Chemical Engineering Research and Design*, vol. 85, pp. 1591–1603, 2007.

[107] J. Lienhard, "Synopsis of lift, drag, and vortex frequency data for rigid circular cylinders," Washington State University, College of Engineering, Tech. Rep. Bulletin No. 300, 1966.

[108] H. Achenbach and E. Heinecke, "On vortex shedding from smooth and rough cylinders in the range of reynolds numbers 6 x 10^3 to 5 x 10^6," *Journal of Fluid Mechanics*, vol. 109, pp. 239–251, 1981.

[109] A. Roshko, "On the wake and drag of bluff bodies," *Journal of the aeronautical sciences*, vol. 22, no. 2, pp. 124–132, 1955.

[110] P. Bearman, "Vortex shedding from oscillating bluff bodies," *Annual Review of Fluid Mechanics*, vol. 16, pp. 195–222, 1984.

[111] R. Gabbai and H. Benaroya, "An overview of modeling and experiments of vortex-induced vibration of circular cylinders," *Journal of Sound and Vibration*, vol. 282, pp. 575–616, 2005.

[112] P. Bearman, "Circular cylinder wakes and vortex-induced vibrations," *Journal of Fluids and Structures*, vol. 27, pp. 648–658, 2011.

[113] C. Williamson, "Vortex dynamics in the cylinder wake," *Annual Reviews of Fluid Mechanics*, vol. 28, pp. 477–539, 1996.

[114] M. Pettigrew, L. Carlucci, C. Taylor, and N. Fisher, "Flow-induced vibration and related technologies in nuclear components," *Nuclear Engineering and Design*, vol. 131, pp. 81–100, 1991.

[115] J.-P. Hulin, C. Fierfort, and R. Coudol, "Experimental study of vortex emission behind bluff obstacles in a gas liquid vertical two-phase flow," *International Journal of Multiphase Flow*, vol. 8, no. 5, pp. 475–490, 1982.

[116] F. Hara, "Air-bubble effects on vortex-induced vibrations of a circular cylinder," in *Excitation and Vibration of Bluff Bodies in Cross Flow*, ser. ASME Winter Annual Meeting, M. Paidoussis, O. Griffin, and M. Sevik, Eds., vol. 1. ASME, December 1984, pp. 103–113.

[117] N. P. Cheremisinoff, Ed., *Encyclopedia of Fluid Mechanics*. Houston, Texas: Gulf Publishing Company, 1986, vol. 3, Chap. 27, pp. 771–810.

[118] T. Uchiyama and Y. Ishiguro, "Experimental study of flow around a circular cylinder inside a bubble plume," *Advances in Chemical Engineering and Science*, vol. 6, pp. 269–280, 2016.

[119] J. Lee and H. Park, "Bubble dynamics and bubble-induced agitation in the homogeneous bubble-swarm past a circular cylinder at small to moderate void fractions," *Physical Review Fluids*, vol. 5, no. 5, p. 054304, 2020.

[120] F. Hara, "Vibrations of circular cylindrical structures subjected to two-phase cross flows," *JSME International Journal*, vol. 30, no. 263, pp. 711–722, 1987.

[121] M. Yokosawa, Y. Kozawa, A. Inoue, and S. Aoki, "Studies on two-phase cross flow. part ii: Transition reynolds number and drag coefficient," *International Journal of Multiphase Flow*, vol. 12, no. 2, pp. 169–184, 1986.

[122] A. Inoue, Y. Kozawa, M. Yokosawa, and S. Aoki, "Studies on two-phase cross flow. part i: Flow characteristics around a cylinder," *International Journal of Multiphase Flow*, vol. 12, no. 2, pp. 149–167, 1986.

[123] Y. Joo and V.K.Dhir, "An experimental study of drag on a single tube and on a tube in an array under two-phase cross flow," *International Journal of Multiphase Flow*, vol. 20, no. 6, pp. 1009–1019, 1994.

[124] T. Shakouchi, D. Tian, and T. Ida, "Behavior of vertical upward gas-liquid two-phase flow past obstacle in rectangular channel (effect of blockage ratio)," *JSME International Journal*, vol. 45, no. 3, pp. 686–693, 2002.

[125] Y. Murai, T. Sasaki, M. Ishikawa, and F. Yamamoto, "Bubble-driven convection around cylinders confined in a channel," *Journal of Fluids Engineering*, vol. 127, pp. 117–123, 2005.

[126] L. Habeeb and R. Al-Turaihi, "Experimental study and cfd simulation of two-phase flow around multi-shape obstacles in enlarging channel," *American Journal of Mechanical Engineering*, vol. 1, no. 8, pp. 470–486, 2013.

[127] A. Voutsinas, T. Shakouchi, K. Tsujimoto, and T. Ando, "Flow visualization and characteristics of vertical gas-liquid bubbly flow around a rectangular cylinder (bubble size effect)," *Journal of Physics: Conference Series*, vol. 147, 2009.

[128] T. Shakouchi, T. Matsumoto, M. Nishio, K. Tsujimoto, and T. Ando, "Flow and aeration characteristics of micro bubble jet flow," *Progress in Multiphase Flow Research*, vol. 2, pp. 33–38, 2007.

[129] , "Modeling and experimental validation of the bubble-induced reynolds stress in the homogeneous bubble-swarm past a circular cylinder," Ph.D. dissertation, , 2021.

[130] D. Kim and M. J. Rau, "Two-phase wakes in adiabatic liquid-gas flow around a cylinder," in *Fluids Engineering Division Summer Meeting*, vol. 83723. American Society of Mechanical Engineers, 2020, p. V002T04A034.

[131] T. Suzuki, Y. Oishi, Y. Murai, Y. Tasaka, and Y. Takeda, "Wake structure of circular cylinder in microbubble mixture," in *Journal of Physics: Conference Series*, vol. 147, no. 1. IOP Publishing, 2009, p. 012012.

[132] H. Meng, "On dispersed two phase flows past obstacles," 1993.

[133] S. Pascal-Ribot and Y. Blanchet, "Buffeting lift forces and local air–water flow aspects around a rigid cylinder," *International journal of multiphase flow*, vol. 33, no. 11, pp. 1237–1254, 2007.

[134] ——, "An improved scaling model of buffeting lift forces in air-water flows," *Journal of Pressure Vessel Technology*, vol. 133, no. 2, 2011.

[135] T. Ijima, F. Hara, and K. Nishikubo, "Unsteady fluid force acting on two tandem circular cylinders subjected to two-phase cross flow," *JSME International Journal, Series C*, vol. 38, no. 2, pp. 219–226, 1995.

[136] F. Hara and T. Iijima, "Vibrations of two circular cylinders in tandem subjected to two-phase bubble cross flows," *Journal of Fluids and Structures*, vol. 3, pp. 389–404, 1989.

[137] V. Ranade, "Numerical simulation of dispersed gas-liquid flows," *Sadhana*, vol. 17, no. 2, pp. 237–273, 1992.

[138] H. A. Jakobsen, B. H. Sannæs, S. Grevskott, and H. F. Svendsen, "Modeling of vertical bubble-driven flows," *Industrial & Engineering Chemistry Research*, vol. 36, no. 10, pp. 4052–4074, 1997.

[139] W. Benguigui, E. Deri, J. Lavieville, S. Mimouni, and E. Longatte, "Numerical investigation and analysis of a dispersed two-phase flow across a single rigid cylinder."

[140] P. Hanafizadeh, S. K. M., B. S. E., and S. Ghanbarzadeh, "Drag coefficient and strouhal number analysis of cylindrical tube in two phase flow," *Energy Equipment and Systems*, vol. 1, pp. 35–58, 2013.

[141] H. Xu, Z. Li, H. Dong, Y. Di, and Y. Tang, "Numerical investigation of the gas-liquid two-phase flow around the square-section cylinder using a multi-scale turbulence model," *Applied Mechanics and Materials*, vol. 444-445, pp. 437–445, 2014.

[142] T. Uchiyama and T. Degawa, "Numerical simulation for gas-liquid two-phase free turbulent flow based on vortex in cell method," *JSME International Journal Series B Fluids and Thermal Engineering*, vol. 49, no. 4, pp. 1008–1015, 2006.

[143] V. L. Nguyen, T. Degawa, T. Uchiyama, and K. Takamure, "Numerical simulation of bubbly flow around a cylinder by semi-lagrangian–lagrangian method," *International Journal of Numerical Methods for Heat & Fluid Flow*, 2019.

[144] T. L. Cook and F. H. Harlow, "Vortices in bubbly two-phase flow," *International journal of multiphase flow*, vol. 12, no. 1, pp. 35–61, 1986.

[145] K. Sugiyama, S. Takagi, and Y. Matsumoto, "Three-dimensional numerical analysis of bubbly flow around a circular cylinder," *JSME International Journal Series B Fluids and Thermal Engineering*, vol. 44, no. 3, pp. 319–327, 2001.

[146] T. Uchiyama, "Numerical simulation of gas-liquid two-phase flow around a rectangular cylinder by the incompressible two-fluid model," *Nuclear science and engineering*, vol. 133, no. 1, pp. 92–105, 1999.

[147] G. Sridhar and J. Katz, "Effect of entrained bubbles on the structure of vortex rings," *Journal of Fluid Mechanics*, vol. 397, pp. 171–202, 1999.

[148] G. Ruetsch and E. Meiburg, "Two-way coupling in shear layers with dilute bubble concentrations," *Physics of Fluids*, vol. 6, no. 8, pp. 2656–2670, 1994.

[149] O. Druzhinin and S. Elghobashi, "Direct numerical simulation of a three-dimensional spatially developing bubble-laden mixing layer with two-way coupling," *Journal of Fluid Mechanics*, vol. 429, pp. 23–61, 2001.

[150] R. Ž. Milenković, B. Sigg, and G. Yadigaroglu, "Bubble clustering and trapping in large vortices. part 1: Triggered bubbly jets investigated by phase-averaging," *International Journal of Multiphase Flow*, vol. 33, no. 10, pp. 1088–1110, 2007.

[151] ——, "Bubble clustering and trapping in large vortices. part 2: Time-dependent trapping conditions," *International journal of multiphase flow*, vol. 33, no. 10, pp. 1111–1125, 2007.

[152] T. Auton, "The lift force on a spherical body in a rotational flow," *Journal of fluid Mechanics*, vol. 183, pp. 199–218, 1987.

[153] I. Nedyalkov, "Design of contraction, test section, and diffuser for a high-speed water tunnel," Master's thesis, 2012.

[154] W. Xiong, K. Kalkühler, and W. Merzkirch, "Velocity and turbulence measurements downstream of flow conditioners," *Flow Measurement and Instrumentation*, vol. 14, no. 6, pp. 249–260, 2003.

[155] R. Loehrke and H. Nagib, "Control of free-stream turbulence by means of honeycombs: a balance between suppression and generation," 1976.

[156] Q. D. Nguyen and C. Lei, "Hydrodynamic characteristics of a confined circular cylinder in cross-flows," *Ocean Engineering*, vol. 221, p. 108567, 2021.

[157] R. Tsai, "A versatile camera calibration technique for high-accuracy 3d machine vision metrology using off-the-shelf tv cameras and lenses," *IEEE Journal on Robotics and Automation*, vol. 3, no. 4, pp. 323–344, 1987.

[158] S. Tan, A. Salibindla, A. U. M. Masuk, and R. Ni, "An open-source shake-the-box method and its performance evaluation," in *13th international symposium on particle image velocimetry*, 2019.

[159] ——, "Introducing openlpt: new method of removing ghost particles and high-concentration particle shadow tracking," *Experiments in Fluids*, vol. 61, no. 2, pp. 1–16, 2020.

[160] A. W. Fitzgibbon, "Simultaneous linear estimation of multiple view geometry and lens distortion," in *Proceedings of the 2001 IEEE Computer Society Conference on Computer Vision and Pattern Recognition. CVPR 2001*, vol. 1. IEEE, 2001, pp. I–I.

[161] F. Bukhari and M. N. Dailey, "Automatic radial distortion estimation from a single image," *Journal of mathematical imaging and vision*, vol. 45, no. 1, pp. 31–45, 2013.

[162] J. Weng, P. Cohen, M. Herniou *et al.*, "Camera calibration with distortion models and accuracy evaluation," *IEEE Transactions on pattern analysis and machine intelligence*, vol. 14, no. 10, pp. 965–980, 1992.

[163] S. Kanner, L. Wang, and P.-O. Persson, "Implicit large-eddy simulation of 2d counter-rotating vertical-axis wind turbines," in *34th Wind Energy Symposium*, 2016, p. 1731.

[164] A. Uranga, P.-O. Persson, M. Drela, and J. Peraire, "Implicit large eddy simulation of transition to turbulence at low reynolds numbers using a discontinuous galerkin method," *International Journal for Numerical Methods in Engineering*, vol. 87, no. 1-5, pp. 232–261, 2011.

[165] C. Moussaed, S. Wornom, M.-V. Salvetti, B. Koobus, and A. Dervieux, "Impact of dynamic subgrid-scale modeling in variational multiscale large-eddy simulation of bluff-body flows," *Acta Mechanica*, vol. 225, no. 12, pp. 3309–3323, 2014.

[166] C. Lei, L. Cheng, and K. Kavanagh, "Spanwise length effects on three-dimensional modelling of flow over a circular cylinder," *Computer methods in applied mechanics and engineering*, vol. 190, no. 22-23, pp. 2909–2923, 2001.

[167] E. Ferdman, M. Otugen, and S. Kim, "Effect of initial velocity profile on the development of round jets," *Journal of Propulsion and Power*, vol. 16, no. 4, pp. 676–686, 2000.